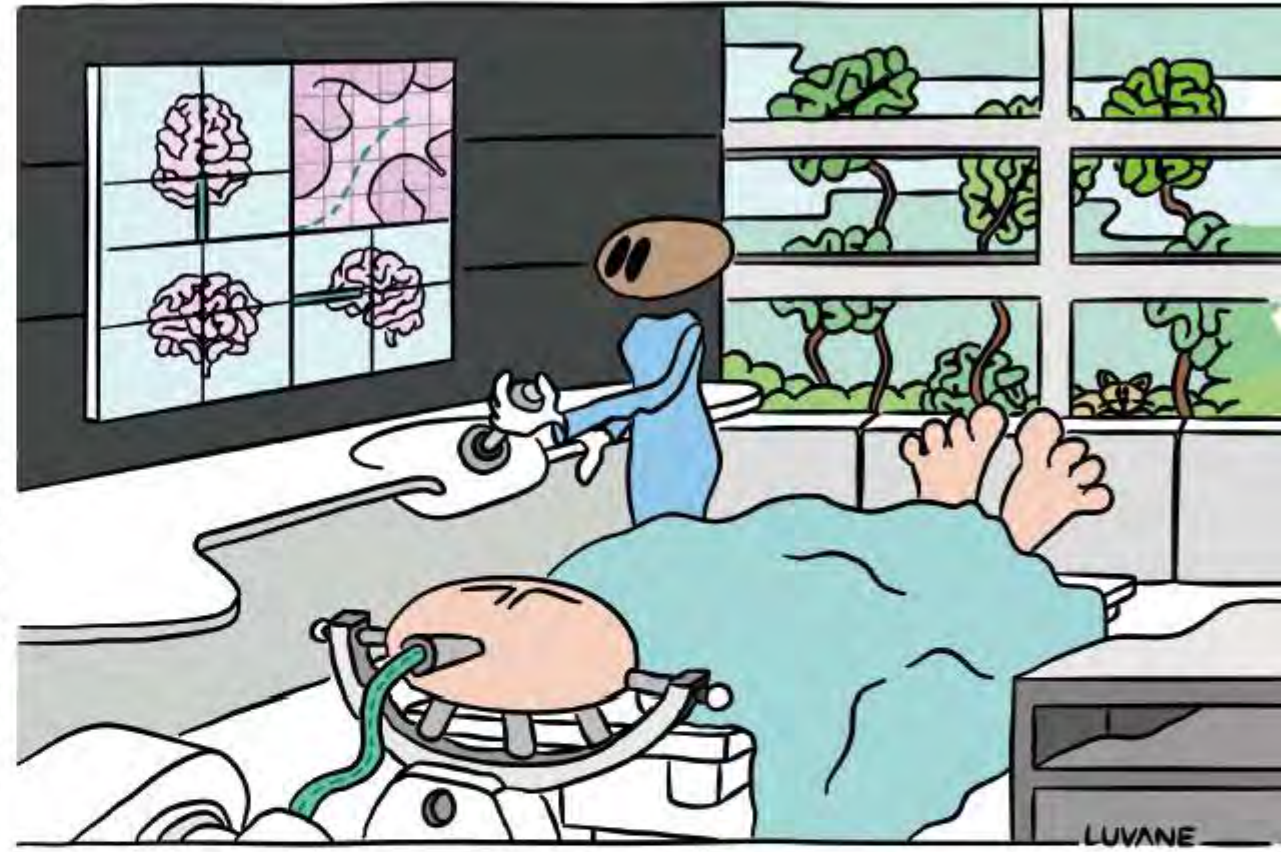


Minimally invasive procedures are favored over open surgeries as they cause less trauma to healthy tissue and this leads to shorter recovery time, and thus lower medical costs. These procedures often utilize flexible instruments because they improve access to the operating areas within the body. However, localization of flexible instruments relative to the anatomy is a challenge. In this thesis, this challenge is undertaken and a technique is developed to localize these instruments. More specifically, methods are presented that can acquire the shape, position and orientation of a flexible instrument. Fiber Bragg gratings are employed as strain gauges, and the sensor measurements are combined with a mathematical model of curves to determine the instrument's location. Various validation experiments are conducted where these methods are applied to a flexible instrument designed for minimally invasive neurosurgery. The results show that Fiber Bragg gratings are effective localization sensors for flexible medical instruments. Moreover, optical fiber sensors have a high potential to further enhance these instruments and research continues to utilize them to their full potential.

Fouzia Khan

Fiber Bragg Grating Sensors for Flexible Medical Instruments



Fiber Bragg Grating Sensors for Flexible Medical Instruments

Fouzia Khan



Fiber Bragg Grating Sensors for Flexible Medical Instruments

Fouzia Khan

Fouzia Khan
Fiber Bragg Grating Sensors for Flexible Medical Instruments
PhD thesis, University of Groningen

Copyright ©2021 Fouzia Khan
No part of this thesis may be reproduced, stored or transmitted in any
form or by any means, without permission from the author.

Cover design: LUVANE
Printed by: Ipskamp Printing, Enschede

The publication of this thesis was financially supported by University of
Groningen.



university of
 groningen

Fiber Bragg Grating Sensors for Flexible Medical Instruments

PhD thesis

to obtain the degree of PhD at the
University of Groningen
on the authority of the
Rector Magnificus Prof. C. Wijmenga
and in accordance with
the decision by the College of Deans.

This thesis will be defended in public on

Wednesday 12 May 2021 at 11.00 hours

by

Fouzia Khan

born on 17 June 1986
in Munshiganj, Bangladesh

Supervisors

Prof. S. Misra
Prof. P.C. Jutte

Assessment Committee

Prof. E.C.J. Consten
Prof. S. Manohar
Dr. J.J. van den Dobbelsteen



This thesis is part of the EDEN2020 project and has received funding from the European Union's Horizon 2020 research and innovation programme under grant agreement #688279. www.eden2020.eu

EDEN2020

Enhanced Delivery Ecosystem for Neurosurgery in 2020

To my dear parents.

Samenvatting

Het hoofddoel van dit proefschrift is de positie en oriëntatie van flexibele medische instrumenten -zoals katheters -te verkrijgen door middel van optische sensoren. Deze sensoren worden in het engels “fiber Bragg-gratings” genoemd, afgekort tot FBG-sensoren. Flexibele instrumenten worden veelvuldig gebruikt bij minimaal invasieve chirurgie, waarbij de chirurg opereert via kleine incisies in plaats van grote. Deze minimaal invasieve operaties zijn gunstig voor patiënten omdat er geen grote wond ontstaat en de patiënt daardoor minder pijn en minder complicaties ervaart, sneller herstelt, en daarmee bijdraagt aan lagere ziekenhuiskosten.

De kleine afmeting van de incisie heeft echter tot gevolg dat de instrumenten niet direct te zien zijn. Daardoor ontbreekt informatie over de positie en oriëntatie van deze instrumenten. Dit probleem wordt momenteel in de praktijk ondervangen door gebruik te maken van beeldvorming via röntgenstralen of door laparoscopie (camera met lichtbron). Deze oplossingen kennen elk hun beperkingen. Denk aan mogelijke schadelijke effecten van straling in geval van röntgenbestraling en beperkte toepasbaarheid bij minimaal invasieve chirurgie van laparoscopie. Scopische benadering is slechts toepasbaar in holten die kunnen worden verlicht, denk aan buikholte of hersenkamers. Daarentegen heeft het gebruik van een camera met een lichtbron binnen in bloedvaten of in solide weefsels niet zo veel zin. Deze beperkingen zijn de aanleiding om onderzoek te doen naar alternatieve methoden om bij minimaal invasieve chirurgie toepassingen noodzakelijke positie en oriëntatie van de flexibel medische instrument te krijgen.

Dit proefschrift beschrijft een van deze alternatieve methodes, namelijk de technieken om met behulp van FBG-sensoren de positie en oriëntatie van een flexibel instrument te verkrijgen. Daarnaast wordt een methode gepresenteerd om op basis van de sensormetingen de krachten op de punt van het instrument te schatten. In Hoofdstuk 2 wordt een techniek gepresenteerd, waarmee de positie van de katheter in 3D-ruimte wordt gereconstrueerd met behulp van de FBG-sensoren. Dit principe wordt verder ontwikkeld in Hoofdstuk 3, door naast de positie van de punt van de katheter ook informatie over de oriëntatie te verkrijgen. Hoofdstuk 4 presenteert een vergelijkende studie tussen twee verschillende soorten multi-core vezels met FBG-sensoren. Een van de vezels heeft rechte kernen terwijl de andere spiraalvormige kernen heeft. Ten slotte worden in Hoofdstuk 5 en 6 twee toepassingsstudies beschreven. In de eerste studie worden FBG-sensoren in combinatie met echografie gebruikt om een katheter te volgen en in de

tweede studie wordt de vorm die is verkregen van de FBG-sensoren gebruikt om de kracht op de punt van een flexibel instrument te schatten.

Het onderzoek in het proefschrift laat zien dat FBG-sensoren effectieve sensoren zijn om informatie te verkrijgen over de positie en oriëntatie van medische instrumenten. Zo kunnen FBG-sensoren worden toegepast op instrumenten die worden gebruikt bij minimaal invasieve chirurgie waarbij het instrument niet direct zichtbaar is. Als onderzoek op dit gebied wordt voortgezet kan zicht worden verkregen op het volledige toepassingspectrum van deze sensoren bij minimaal invasieve chirurgie.

Summary

The main objective of this thesis is to utilize optical sensors called fiber Bragg gratings (FBG) to acquire the position and orientation of flexible medical instruments such as catheters. These instruments are frequently used in minimally invasive surgeries where small incisions are made to perform the surgery. These minimally invasive surgeries are beneficial for patients because there is no large wound therefore the patient experiences less pain, fast recovery, and fewer complications; thus it contributes to lower hospital costs.

The small size of the incision means that during a minimally invasive surgery the instrument cannot be directly seen, thus the position and orientation of the instrument are concealed. This issue is mitigated currently in practice by utilizing imaging like X-rays or laparoscopes (camera with light source); but these solutions have certain drawbacks such as harmful radiation used in X-rays and inability to use laparoscopes for all minimally invasive surgeries. A laparoscope can only be used in cavities that can be illuminated, such as the abdominal cavity or the ventricles in the brain. However, it is not possible to use a light source in a blood vessel or in solid tissues. These limitations motivate research into alternative methods of acquiring position and orientation of a flexible instrument.

This thesis is an outcome of one such research endeavor and it presents techniques of acquiring the position and orientation of a flexible instrument based on measurements from FBG sensors. Moreover, a method to estimate the forces at the instrument's tip from the sensor measurements is also presented. Chapter 2 provides a technique to get the shape of the catheter based on FBG measurements and to get the position of the catheter in 3D space. The technique is further developed in Chapter 3 to acquire the orientation in addition to the position of the catheter tip. Chapter 4 presents a comparison study between two different types of multi-core fibers that have FBG sensors. One of the fiber has straight cores while the other has helical cores. Lastly, Chapter 5 and 6 present two application studies where the first study utilizes FBG sensors in conjunction with Ultrasound to track a catheter and the second study utilizes the shape of a flexible instrument to estimate the force on its tip.

The research in the thesis shows that FBG sensors are effective as position and orientation sensors for flexible medical instruments. Thus, FBG sensors can be applied to instruments utilized in minimally invasive surgery where the instrument is not directly visible. Continuing research in this field will provide insight into the full spectrum of applications of these sensors.

Contents

Samenvatting	ix
Summary	xi
I Introduction	1
1 Thesis Overview	3
1.1 Motivation	3
1.2 Literature Review	7
1.3 Main Contributions	9
References	12
II Shape and Pose Sensing	19
2 Shape Acquisition	21
2.1 Introduction	21
2.2 Theoretical Framework	23
2.3 Experiments	30
2.4 Conclusions	35
References	37
3 Pose Measurement	41
3.1 Introduction	41
3.2 Theory	43
3.3 Experiments	49
3.4 Discussion	56
3.5 Conclusions and Future Work	58
References	59

4	Straight and Helical Core Fibers	63
4.1	Introduction	64
4.2	Theoretical Background	65
4.3	Experiments and Results	69
4.4	Conclusions	75
4.5	Appendix	76
	References	78
III	Application Studies	81
5	Catheter Tracking	83
5.1	Introduction	83
5.2	Shape Sensing Using Fiber Bragg Gratings	86
5.3	Ultrasound Tracking Algorithm	88
5.4	Sensor Fusion Algorithm	93
5.5	Experiments	97
5.6	Conclusions	101
	References	103
6	Force Estimation	107
6.1	Introduction	107
6.2	Shape Reconstruction	110
6.3	Rigid Link Model	111
6.4	Cosserat Model	115
6.5	Experiments and Results	117
6.6	Conclusions	120
	References	121
IV	Outlook	125
7	Conclusions	127
7.1	Discussion and Future Work	127
7.2	Scientific Disseminations	131
	Acknowledgments	133
	Curriculum Vitae	135

Part I

Introduction

The research presented in this thesis is focused on utilizing fiber Bragg grating (FBG) sensors to acquire shape and pose measurements of flexible medical instruments such as catheters. These sensors are well suited for medical applications due to their size, flexibility and immunity to electromagnetic interference. This part of the thesis places the research within the relevant literature and clinical practice. Moreover, it presents the motivation and contributions of the research.

Chapter 1

Thesis Overview

1.1 Motivation

Flexible medical instruments such as catheters, endoscopes and needles are utilized in clinical practice for various minimally invasive procedures; some examples are coronary angioplasty, colonoscopy and brachytherapy, as illustrated in Figure 1.1 [1]. Coronary angioplasty is performed to treat blocked or narrowed coronary arteries due to plaque build up. During the procedure a catheter is inserted through an artery in either the groin or the arm and pushed to the heart with the aid of fluoroscopy [2,3]. Colonoscopy is conducted to diagnose colorectal diseases, an endoscope is inserted into the colon in order to visually inspect the entire colon [4]. Brachytherapy is a cancer treatment in which radioactive seeds are placed in or near the treatment site under the guidance of either ultrasound (US), magnetic resonance imaging (MRI) or computer tomography (CT) [5–7]. Minimally invasive procedures are preferred to open surgeries because they have similar efficacy as open surgery while inflicting minimum trauma which leads to shorter recovery time, lower post-operation complications, and lower costs [8,9]. The instruments utilized for minimally invasive procedures are frequently flexible because they increase the accessibility to the target site while maintaining the small incision [10–14]. As a result, flexible instruments are prevalent in clinical practice and also in research studies, some examples of these instruments are shown in Figure 1.2.

Flexible instruments improve accessibility, but localization of these instruments during a procedure becomes challenging due to the insertion size and flexibility of the instruments. For example, in coronary angioplasty once the catheter is inserted into an artery the catheter tip cannot be vi-

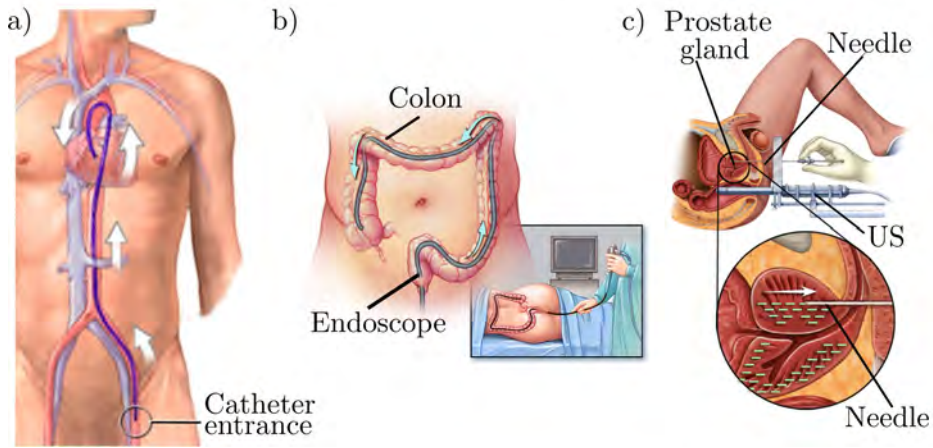


Figure 1.1: Examples of minimally invasive surgeries. a) Coronary angioplasty where a catheter is inserted through an artery near the groin and guided to the heart with x-ray fluoroscopy guidance (images courtesy of A.D.A.M., Georgia, USA ©). b) Colonoscopy which is conducted for diagnosis using an endoscope equipped with a camera (image courtesy of Mayo Foundation for Medical Education and Research, Rochester, USA ©). c) Brachytherapy for treatment of prostate cancer. A set of radioactive seeds are inserted into the prostate under ultrasound (US) guidance (image courtesy of Mayo Foundation for Medical Education and Research, Rochester, USA ©).

sually localized and imaging like fluoroscopy must be used to accurately navigate the catheter to the required location. Similarly for other minimally invasive treatments, the knowledge of the position and orientation of the flexible instrument is essential; however is difficult to acquire.

In clinical practice the instruments are localized using medical imaging equipment such as magnetic resonance imaging (MRI), ultrasound (US), x-ray fluoroscopy, computer tomography (CT) and endoscopy, see Figure 1.3. These modalities are effective and have certain advantages but there are also some drawbacks. MRI provides high resolution images however it is expensive to use due to its high maintenance costs. In addition, all equipment in the MR scanner must be non-ferromagnetic due to the magnetic field generated, thus limiting the equipment that can be used there. Lastly, the restricted space in the MRI bore can hinder or prohibit instruments' movements that are required for the procedures [15]. US has the benefit of a high update rate, however the images are low in spatial resolution and

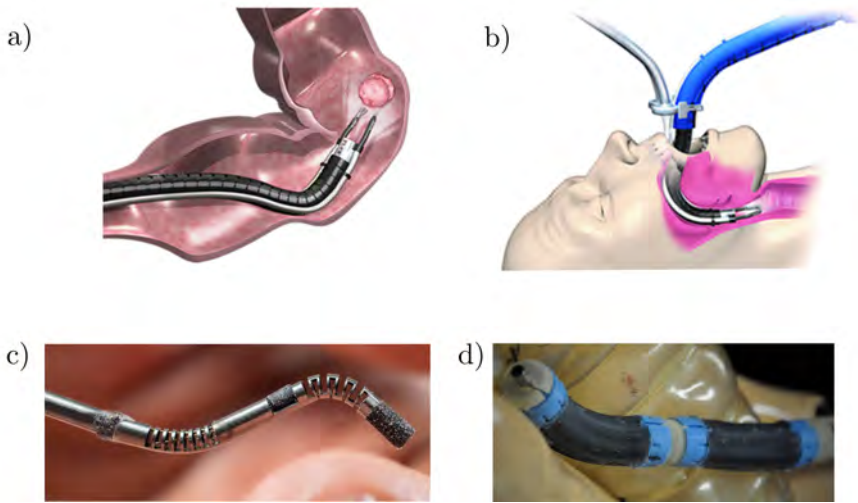


Figure 1.2: Examples of flexible instruments. a) Flex[®] Robotic System for colon procedures (image courtesy of Medrobotics, Massachusetts, USA ©). b) Flex[®] Robotic System for ear nose and throat (image courtesy of Medrobotics, Massachusetts, USA ©). c) Steerable instrument for pediatric neurosurgery (image courtesy of Georgia Institute of Technology, Georgia, USA ©). d) An pneumatically actuated flexible instrument called Stiff-Flop (image courtesy of King’s College London, London, UK ©)

often suffer from image artifacts like comet tail or shadowing [16]. X-ray fluoroscopy can provide close to real-time images and with the aid of contrast agent the anatomy of interest can be viewed with high accuracy. The major disadvantages of fluoroscopy and CT are the harmful dose of X-rays delivered to the patient and the risk of exposure to X-rays for the interventionalist. Endoscopy and laparoscopy have revolutionized minimally invasive surgery by providing visualization of the surgical site that is accessed percutaneously or via natural orifice. The main drawbacks of endoscopy is the lack of its location information in relation to the anatomy and loop formation in colonoscopy [4, 15].

There has been extensive research conducted on alternative methods of localization in order to enhance the current state-of-the-art. One approach is to combine multiple modalities so that the short comings of one is mitigated by the other. An example would be utilizing CT, US and electromagnetic (EM) tracking to acquire the position of the surgical instrument [17]. The drawback of this approach is that EM tracking works

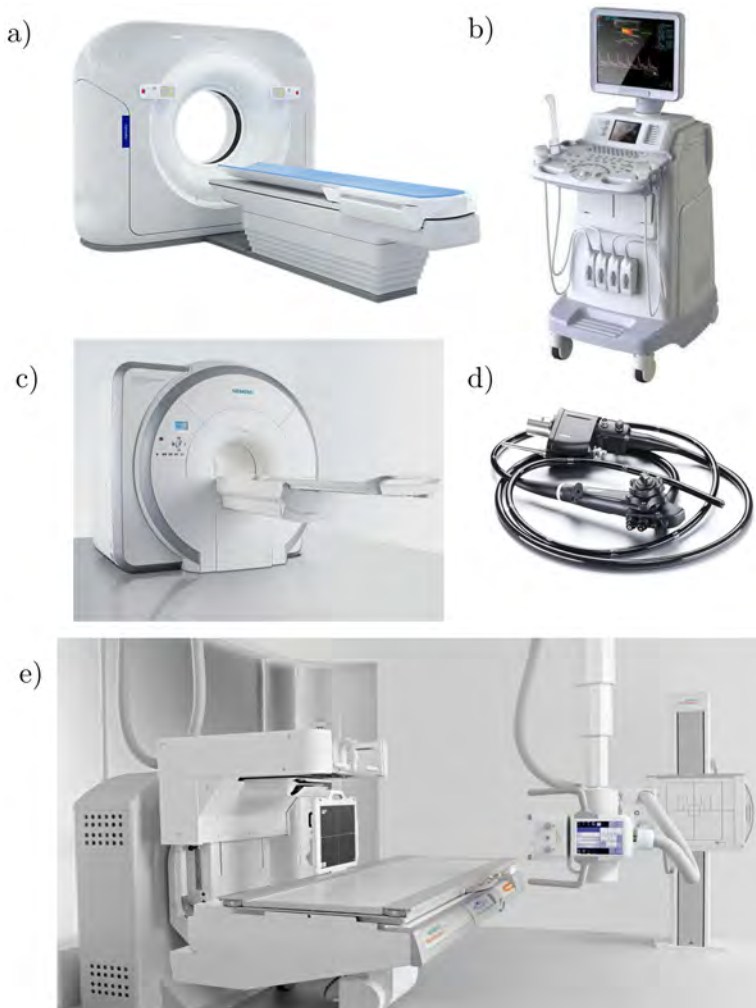


Figure 1.3: Medical imaging equipment utilized in practice for localization. a) Computer tomography (CT) scanner (Philips, Eindhoven, Netherlands). b) Ultrasound (US) scanner (GE Healthcare, Illinois, United States) c) Magnetic resonance imaging (MRI) scanner (Siemens-healthineers, Erlangen, Germany). d) Endoscope (Pentax Medical, New Jersey, United States). e) X-ray fluoroscopy (Siemens-healthineers, Erlangen, Germany).

within a limited space and the tracking accuracy degrades significantly in the presence of metallic objects such as surgical instruments [18]. Another approach is to use endoscopic images to localize the instrument tip within

the anatomy, but this approach suffers from drift and loss of tracking in case of occlusions, shadows and fast motion [19]. For flexible instruments that are been developed by research groups, various sensing methods are utilized for localization, such as pressure sensors for pneumatically actuated instruments like Stiff-Flop, sensors to measure cable lengths for cable driven instruments such as Flex[®] Robotic System. Moreover, a novel inductive sensor composed of elastomer and liquid metal in a helical structure has been developed for sensing bend and tensile deformation in soft cylindrical instruments [20]. The issue with these methods is compatibility within the operating environment, for instance sensors on the instrument are required to be sterilizable and the novel sensor utilizes liquid metals which are not bio-compatible thus are unsafe [20].

The sensors that are highly suitable for the clinical environment are the ones inscribed in optical fibers. This is because optical fibers are immune to electromagnetic interference, chemically inert, nontoxic, small in diameter, light weight, and flexible. They are used most commonly in endoscopes to transmit light to the operating area for the scope camera. Moreover, they are also used for pressure, temperature, oxygenation, blood flow, electrocardiogram and force measurements [21–23]. In addition, they can be utilized in various manner for sensing shape and position of flexible instruments [24]. The compatibility of optical fibers with the medical environment make them a natural choice as localization sensors in medical instruments. This thesis focuses on using fiber Bragg gratings (FBG) for sensing tip pose, that is position and orientation, of flexible instruments. The objective is to acquire robust localization which is essential for effective minimally invasive procedures. The next section presents the literature on shape and position sensing of flexible medical instruments using FBG sensors.

1.2 Literature Review

The origins of fiber Bragg gratings lie in experiments conducted in 1978 by Hill *et al.* at the Canadian Communications Research Center [25]. It was discovered that exposing germanium doped fiber to argon-ion laser radiation lead to the fiber reflecting back some intensity of the input light. Moreover, it was established that the refractive index of the fiber can be altered and creating a periodic perturbation of the refractive index lead to the fiber reflecting back a narrow-band of the light wavelength. This periodic perturbation is termed the Bragg gratings and the reflected wavelength is called the Bragg wavelength, as shown in Figure 1.4. Further

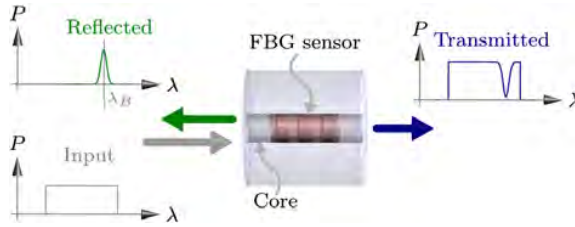


Figure 1.4: Fiber Bragg grating sensor reflects back a narrow-band of light. The central wavelength of the reflected spectrum is called the Bragg wavelength, λ_B . The spectra utilized consists of the optical power P for every wavelength λ .

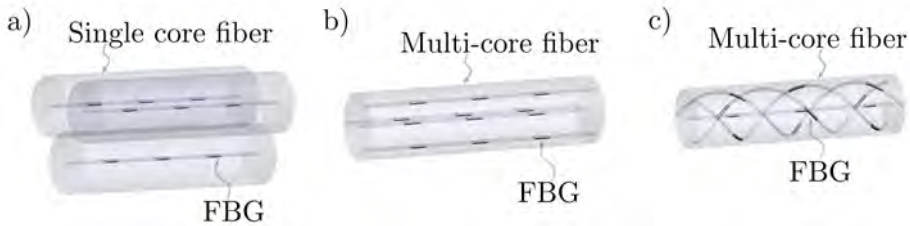


Figure 1.5: Examples of configurations using fiber Bragg grating (FBG) sensors a) A bundle of 3 single core fibers. b) A multi-core fiber with straight cores. c) A multi-core fiber with helical cores.

research also showed that the Bragg wavelength alters based on the strain and temperature experienced by the fiber once the grating is created. This phenomenon has led to the use of Bragg gratings as strain and temperature sensor [25]. Fiber Bragg gratings are used in many industries, however this section focuses on its application in medical instruments for shape and position sensing.

In the literature, various configurations of FBG sensors are proposed in order to sense shape and position of medical instruments. Three common configurations are illustrated in Figure 1.5. Sefati *et al.*, Ryu *et al.*, Wang *et al.* and Moon *et al.* use a bundle of single core optical fibers that are inscribed with FBG sensors; the bundle is such that the sensors are parallel to each other and the sensors are aligned such that they are co-located [26–29]. This configuration can also be realized in multi-core fibers with straight cores as proposed in Barrera *et al.*, Bronnikov *et al.* and Zhang *et al.* [30–32]. The advantages of multi-core fiber are that it has a smaller overall diameter than a fiber bundle of single core fibers, it is mechanically

stronger and the FBG alignment is more accurate [30,31,33]. An issue with parallel FBGs is that the twist sensing is weak as observed by Duncan *et al.* [34]. In order to sense the twist more accurately, FBG sensors have been placed in a helical shape either by inscribing the sensors in multi-core fiber with helical core or by winding single core fiber with FBGs in helical slots [35–37]. The wavelength shift in each FBG sensor can be related to the strain on the sensor by the configuration of the sensors [30,38–40]. The curvature and twist which create the shape of the fiber are determined based on the sensor configuration geometry and the calculated strains on the co-located FBG sensors [28,38,41]. The position of the fiber in 3D space is derived from the shape most frequently by integrating the curvature vector, however the use of Frenet-Serret frames is also common [42,43]. Moreover, a few studies have also used parallel transport or Bishop frames for reconstructing the fiber’s position [44].

These techniques have been used in numerous instruments developed for clinical applications. Xu *et al.* sense the shape and also the tip force of a concentric tube robot [35]. Liu *et al.* use FBG sensors to sense large deflection in manipulators for minimally invasive surgery [45]. Accuracy of needle position using FBG is shown by Henken *et al.* and Roesthuis *et al.* [46,47]. Real time needle tracking using FBG sensors for brachytherapy is conducted by Battisti *et al.* [48]. FBG sensors have also been applied for endovascular procedures by Jäckle *et al.* [49]. Automatic insertion of medical instruments with FBG sensors for feedback in close loop control has been demonstrated by Shahriari *et al.*, Abayazid *et al.*, and Roesthuis *et al.* [50–52]. Research in FBG sensors for medical applications has been extensive and it continues to be an interesting topic due to its high potential in enhancing medical instruments. As an example, the Philips’ Fiber Optic Real Shape (FORS) project that utilizes FBG sensors for 3D visualization of a catheter for cardiovascular procedure has been through human trials and is in preparation for the market [53]. The research in this thesis also adds to the literature and its main contributions are presented in the next section.

1.3 Main Contributions

The research in this thesis is part of a Horizon 2020 European project called Enhanced Delivery Ecosystem for Neurosurgery (EDEN2020) [54]. The objective of the project is to provide a step change in the technology for minimally invasive neurosurgery. An artistic impression of the EDEN2020

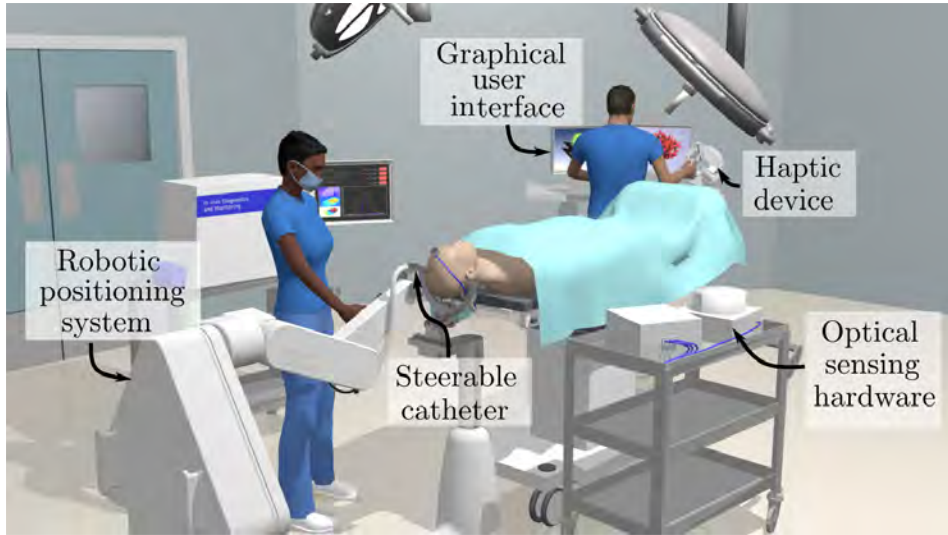


Figure 1.6: Artistic impression of the Enhanced Delivery Ecosystem for Neurosurgery (EDEN2020) project platform. The steerable catheter is controlled by the surgeon using a haptic device. The graphical user interface displays the catheter’s tip pose acquired from fiber Bragg grating sensors.

platform is shown in Figure 1.6. One of the aims is to utilize a novel steerable catheter in minimally invasive neurosurgery such that the surgeon has control over both the position and orientation of the catheter’s tip. This feature provides the ability to approach a target such as a tumor from a desired angle and also facilitates avoidance of critical structures. Moreover, the project aims to develop and integrate the following key areas of technologies: pre-operative MRI and diffusion MRI imaging; intra-operative ultrasound; robotics assisted catheter steering; brain diffusion modeling and a pre-commercial prototype of a robotics assisted neurosurgical product [54]. The research in this thesis is utilized in the EDEN2020 project for steering, with robotics assistance, the novel catheter that is produced for this project. In order to accurately steer the catheter, knowledge of its tip pose, that is the position and orientation of its tip, is essential. Thus, acquiring the tip pose of a catheter was a research goal of this thesis and that lead to the following contributions:

1. Shape and position measurements with FBG sensors in multi-core fibers (Chapter 2) [55].
2. Acquisition of tip pose using multi-core fibers with FBG sensors (Chap-

- ter 3) [56].
3. Comparison of measurement accuracy between two FBG inscribed multi-core fibers; one with straight cores and the other with helical cores (Chapter 4) [57].
 4. Tracking a magnetically actuated catheter with a multi-core fiber with FBG sensors (Chapter 5) [58].
 5. Force sensing based on shape measurements acquired from a bundle of single core fibers with FBG sensors (Chapter 6) [59].

The following chapters give details on the above mentioned contributions. Chapter 2 and 3 utilizes multi-core fiber with straight cores that have co-located FBG sensors and the curvatures of the fiber are derived from the FBG strain measurements in conjunction with their position on the fiber's cross section. In the experiments for Chapter 2, the instrument is sensorized with several multi-core fibers and the curvatures of all the fibers are merged to get the instrument's curvature. Next, using Frenet-Serret equations the instrument is reconstructed in Euclidean space and that gives the position of all the points along the length of the instrument. Chapter 3 extends the technique in Chapter 2 to acquire orientation in addition to position and utilizes Bishop frames instead of Frenet-Serret frames. For the experiments, the tip pose of four multi-core fibers are compared against ground truth values of the fiber tips. In Chapter 2 and 3 multi-core fibers with straight cores were used, however the FBGs were not sensitive to shear strain. In order to measure shear strain the FBGs are inscribed on multi-core fibers with helical cores. In Chapter 4, a comparative study is conducted between a multi-core fiber with straight cores and a multi-core fiber with helical cores. Both fibers have FBG sensors and the accuracy of the fibers in measuring curvature, twist and pose are compared. The fibers are modeled as elastic rods and equations for elastic rods are applied to get the tip pose of the fibers. The curvature and twist is calculated based on the FBG measurements and their position on the fiber's cross section. In Chapter 5 and 6, the techniques from Chapter 2 and 3 are applied to track a catheter's tip and estimate its tip force. In Chapter 5, a single multi-core fiber in conjunction with ultrasound images are used to track the tip of a magnetically actuated catheter. Chapter 6 presents an algorithm to estimate the forces at a flexible instrument's tip based on the shape of the instrument. Lastly, Chapter 7 concludes the thesis with a discussion of the results and future work.

References

- [1] G. Wan, Z. Wei, L. Gardi, D. B. Downey, and A. Fenster, “Brachytherapy needle deflection evaluation and correction,” *Medical Physics*, vol. 4, no. 32, pp. 902–909, 2005.
- [2] Mayo Clinic Staff, “Coronary angioplasty and stents,” [mayoclinic.org, https://www.mayoclinic.org/tests-procedures/coronary-angioplasty/about/pac-20384761](https://www.mayoclinic.org/tests-procedures/coronary-angioplasty/about/pac-20384761) (accessed June 05, 2020).
- [3] National Heart, Lung, and Blood Institute, “Percutaneous coronary intervention,” [nhlbi.nih.gov, https://www.nhlbi.nih.gov/health-topics/percutaneous-coronary-intervention](https://www.nhlbi.nih.gov/health-topics/percutaneous-coronary-intervention) (accessed June 05, 2020).
- [4] M. Bruce and J. Choi, “Detection of endoscopic looping during colonoscopy procedure by using embedded bending sensors,” *Medical devices*, vol. 11, pp. 171–191, 2018.
- [5] M. Borot de Battisti, B. Denis de Senneville, G. Hautvast, D. Binnekamp, J. J. W. Langendijk, M. Maenhout, and M. A. Moerland, “A novel adaptive needle insertion sequencing for robotic, single needle MR-guided high-dose-rate prostate brachytherapy,” *Physics in Medicine & Biology*, vol. 62, no. 10, p. 4031-4045, 2017.
- [6] Mayo Clinic Staff, “Brachytherapy,” [mayoclinic.org https://www.mayoclinic.org/tests-procedures/brachytherapy/about/pac-20385159](https://www.mayoclinic.org/tests-procedures/brachytherapy/about/pac-20385159), accessed (June 06, 2020).
- [7] Memorial Sloan Kettering Cancer Center, “What is Brachytherapy?” [www.mskcc.org, https://www.mskcc.org/cancer-care/diagnosis-treatment/cancer-treatments/radiation-therapy/what-brachytherapy](https://www.mskcc.org/cancer-care/diagnosis-treatment/cancer-treatments/radiation-therapy/what-brachytherapy) (accessed June 06, 2020).
- [8] J. E. Wickham, “The new surgery,” *British Medical Journal*, vol. 295, no. 6613, pp. 1581–1582, 1987.
- [9] K. Ahmed, M. S. Khan, A. Vats, K. Nagpal, O. Priest, V. Patel, J. A. Vecht, H. Ashrafian, G. Yang, T. Athanasiou, and A. Darzi, “Current status of robotic assisted pelvic surgery and future developments,” *International Journal of Surgery*, vol. 7, no. 5, pp. 431–440, 2009.
- [10] T. K. Morimoto, E. W. Hawkes, and A. M. Okamura, “Design of a compact actuation and control system for flexible medical robots,” *IEEE Robotics and Automation Letters*, vol. 2, no. 3, pp. 1579–1585, 2017.

-
- [11] S. Y. Ko and F. Rodriguez y Baena, "Towards a miniaturized needle steering system with path planning for obstacle avoidance," *IEEE Transactions on Biomedical Engineering*, vol. 60, no. 4, pp. 910–917, 2013.
- [12] P. E. Dupont, J. Lock, B. Itkowitz, and E. Butler, "Design and control of concentric-tube robots," *IEEE Transactions on Robotics*, vol. 26, no. 2, pp. 209–225, 2010.
- [13] H. Abidi, G. Gerboni, M. Brancadoro, J. Frascas, A. Diodato, M. Cianchetti, H. Wurdemann, K. Althoefer, and A. Menciassi, "Highly dexterous 2-module soft robot for intra-organ navigation in minimally invasive surgery," *The International Journal of Medical Robotics and Computer Assisted Surgery*, vol. 14, no. 1, 2018.
- [14] T. E. T. Seah, T. N. Do, N. Takeshita, K. Y. Ho, and S. J. Phee, "Future of flexible robotic endoscopy systems," *ArXiv*, vol. abs/1703.05569, 2017.
- [15] National Research Council (US) and Institute of Medicine (US) Committee on the Mathematics and Physics of Emerging Dynamic Biomedical Imaging, "Chapter 12, Image-guided minimally invasive diagnostic and therapeutic interventional procedures," <https://www.ncbi.nlm.nih.gov/books/NBK232483/> (accessed May 31, 2020).
- [16] M. K. Feldman, S. Katya, and M. S. Blackwood, "US Artifacts," *RadioGraphics*, vol. 29, no. 4, pp. 1179–1189, 2009.
- [17] C. Humphries, "New Tools for Minimally Invasive Surgery," MIT Technology Review, <https://www.technologyreview.com/2006/08/09/100596/new-tools-for-minimally-invasive-surgery/> (accessed June 01, 2020).
- [18] A. M. Franz, T. Haidegger, W. Birkfellner, K. Cleary, T. Peters, and L. Maier-Hein, "Electromagnetic tracking in medicine—a review of technology, validation, and applications," *IEEE Transactions on Medical Imaging*, vol. 33, no. 8, pp. 1702–1725, 2014.
- [19] X. Du, M. Allan, A. Dore, S. Ourselin, D. Hawkes, J. D. Kelly, and D. Stoyanov, "Combined 2D and 3D tracking of surgical instruments for minimally invasive and robotic-assisted surgery," *International Journal*

- of Computer Assisted Radiology and Surgery*, vol. 11, no. 6, pp. 1109–1119, 2016.
- [20] M. Runciman, A. Darzi, and G. P. Mylonas, “Soft robotics in minimally invasive surgery,” *Soft Robotics*, vol. 6, no. 4, pp. 423–443, 2019.
- [21] A. Mendez, “Medical applications of fiber-optics: Optical fiber sees growth as medical sensors,” www.laserfocusworld.com, <https://www.laserfocusworld.com/fiber-optics/article/16562291/medical-applications-of-fiberoptics-optical-fiber-sees-growth-as-medical-sensors> (accessed June 10, 2020).
- [22] Nai-Group, “Advances in medical fiber optic technology for improving patient care,” nai-group.com, <https://www.nai-group.com/medical-fiber-optic-technology-patient-care/> (accessed June 10, 2020).
- [23] S. Poeggel, D. Tosi, D. Duraibabu, G. Leen, D. McGrath, and E. Lewis, “Optical fibre pressure sensors in medical applications,” *Sensors*, vol. 15, no. 7, pp. 17 115–17 148, 2015.
- [24] R. Correia, S. James, S. Lee, S. P. Morgan, and S. Korposh, “Biomedical application of optical fibre sensors,” *Journal of Optics*, vol. 20, no. 7, pp. 1–26, 2018.
- [25] K. O. Hill and G. Meltz, “Fiber Bragg grating technology fundamentals and overview,” *Journal of Lightwave Technology*, vol. 15, no. 8, pp. 1263–1276, 1997.
- [26] S. Sefati, M. Pozin, F. Alambeigi, I. Iordachita, R. H. Taylor, and M. Armand, “A highly sensitive fiber Bragg grating shape sensor for continuum manipulators with large deflections,” in *Proceedings of IEEE Sensors*, pp. 1-3, Glasgow, UK, 2017.
- [27] S. C. Ryu and P. E. Dupont, “Fbg-based shape sensing tubes for continuum robots,” in *Proceedings of IEEE International Conference on Robotics and Automation (ICRA)*, pp. 3531-3537, Hong Kong, China, 2014.
- [28] H. Wang, R. Zhang, W. Chen, X. Liang, and R. Pfeifer, “Shape detection algorithm for soft manipulator based on fiber Bragg gratings,” *IEEE/ASME Transactions on Mechatronics*, vol. 21, no. 6, pp. 2977–2982, 2016.

-
- [29] H. Moon, J. Jeong, S. Kang, K. Kim, Y. Song, and J. Kim, "Fiber-Bragg-grating-based ultrathin shape sensors displaying single-channel sweeping for minimally invasive surgery," *Optics and Lasers in Engineering*, vol. 59, pp. 50–55, 2014.
- [30] D. Barrera, I. Gasulla, and S. Sales, "Multipoint two-dimensional curvature optical fiber sensor based on a nontwisted homogeneous four-core fiber," *Journal of Lightwave Technology*, vol. 33, no. 12, pp. 2445–2450, 2015.
- [31] K. Bronnikov, A. Wolf, S. Yakushin, A. Dostovalov, O. Egorova, S. Zhuravlev, S. Semjonov, S. Wabnitz, and S. Babin, "Durable shape sensor based on FBG array inscribed in polyimide-coated multicore optical fiber," *Opt. Express*, vol. 27, no. 26, pp. 38 421–38 434, 2019.
- [32] H. Zhang, Z. Wu, P. P. Shum, R. Wang, X. Q. Dinh, S. Fu, W. Tong, and M. Tang, "Fiber Bragg gratings in heterogeneous multicore fiber for directional bending sensing," *Journal of Optics*, vol. 18, no. 8, pp. 1–7, 2016.
- [33] B. Van Hoe, J. Van Roosbroeck, C. Voigtländer, J. Vlekken, and E. Lindner, "Distributed strain and curvature measurements based on tailored draw tower gratings," in *Proceedings of IEEE Avionics and Vehicle Fiber-Optics and Photonics Conference (AVFOP)*, pp. 285–286, California, USA, 2016.
- [34] R. G. Duncan and M. T. Raum, "Characterization of a fiber-optic shape and position sensor," in *Proceedings of Smart Structures and Materials 2006: Smart Sensor Monitoring Systems and Applications*, pp. 26–36, California, USA, 2006.
- [35] R. Xu, A. Yurkewich, and R. V. Patel, "Curvature, torsion, and force sensing in continuum robots using helically wrapped fbg sensors," *IEEE Robotics and Automation Letters*, vol. 1, no. 2, pp. 1052–1059, 2016.
- [36] P. S. Westbrook, K. S. Feder, T. Kremp, T. F. Taunay, E. Monberg, J. Kelliher, R. Ortiz, K. Bradley, K. S. Abedin, D. Au, and G. Puc, "Integrated optical fiber shape sensor modules based on twisted multicore fiber grating arrays," in *Proceedings of Optical Fibers and Sensors for Medical Diagnostics and Treatment Applications XIV*, pp. 88–94, California, USA, 2014.

- [37] C. G. Askins, G. A. Miller, and E. J. Friebele, “Bend and twist sensing in a multi-core optical fiber,” in *Proceedings of 21st Annual Meeting of the IEEE Lasers and Electro-Optics Society*, pp. 109-110, Acapulco, Mexico, 2008.
- [38] P. S. Westbrook, T. Kremp, K. S. Feder, W. Ko, E. M. Monberg, H. Wu, D. A. Simoff, T. F. Taunay, and R. M. Ortiz, “Continuous multicore optical fiber grating arrays for distributed sensing applications,” *Journal of Lightwave Technology*, vol. 35, no. 6, pp. 1248–1252, 2017.
- [39] K. K. C. Lee, A. Mariampillai, M. Haque, B. A. Standish, V. X. D. Yang, and P. R. Herman, “Temperature-compensated fiber optic 3D shape sensor based on femtosecond laser direct-written Bragg grating waveguides,” *Optics Express*, vol. 21, no. 20, pp. 24 076–24 086, 2013.
- [40] N. Papachristou, J. Morton, R. M. Carter, R. R. J. Maier, and W. N. MacPherson, “Temperature effects upon a multicore optical fibre curvature sensor,” in *Proceedings of IEEE Sensors*, pp. 1-3, Glasgow, UK, 2017.
- [41] S. Jäckle, J. Strehlow, and S. Heldmann, *Shape Sensing with Fiber Bragg Grating Sensors: A Realistic Model of Curvature Interpolation for Shape Reconstruction*, 2019, pp. 258–263.
- [42] J. P. Moore, “Shape sensing using multi-core fiber,” in *Proceedings of Optical Fiber Communications Conference and Exhibition*, pp. 1-3, California, USA, 2015.
- [43] P. Leyendecker and R. Haslinger, “Fiber optic curvature sensor,” in *Proceedings of IEEE Sensors*, pp. 43-46, Valencia, Spain, 2014.
- [44] J. Cui, S. Zhao, C. Yang, and J. Tan, “Parallel transport frame for fiber shape sensing,” *IEEE Photonics Journal*, vol. 10, no. 1, pp. 1–12, 2018.
- [45] H. Liu, A. Farvardin, S. A. Pedram, I. Iordachita, R. H. Taylor, and M. Armand, “Large deflection shape sensing of a continuum manipulator for minimally-invasive surgery,” in *Proceedings of IEEE International Conference on Robotics and Automation*, pp. 201-206, Washington State, USA, 2015.
- [46] K. R. Henken, J. Dankelman, J. J. van den Dobbelsteen, L. K. Cheng, and M. S. van der Heiden, “Error analysis of fbg-based shape sensors for

- medical needle tracking,” *IEEE/ASME Transactions on Mechatronics*, vol. 19, no. 5, pp. 1523–1531, 2014.
- [47] R. J. Roesthuis, M. Kemp, J. J. van den Dobbelen, and S. Misra, “Three-dimensional needle shape reconstruction using an array of fiber Bragg grating sensors,” *IEEE/ASME Transactions on Mechatronics*, vol. 19, no. 4, pp. 1115–1126, 2014.
- [48] M. B. Battisti, B. D. Senneville, M. Maenhout, J. Legendijk, M. Vulpen, G. Hautvast, D. Binnekamp, and M. Moerland, “Fiber Bragg gratings-based sensing for real-time needle tracking during mr-guided brachytherapy,” *Medical Physics*, vol. 43, no. 10, pp. 5288–5297, 2016.
- [49] S. Jäckle, T. Eixmann, H. Schulz-Hildebrandt, G. Hüttmann, and T. T. Pätz, “Fiber optical shape sensing of flexible instruments for endovascular navigation,” *International Journal of Computer Assisted Radiology and Surgery*, vol. 14, no. 1, pp. 1–9, 2019.
- [50] N. Shahriari, R. J. Roesthuis, N. J. van de Berg, J. J. van den Dobbelen, and S. Misra, “Steering an actuated-tip needle in biological tissue: Fusing fbg-sensor data and ultrasound images,” in *Proceedings of IEEE International Conference on Robotics and Automation*, pp. 4443–4449, Stockholm, Sweden, 2016.
- [51] M. Abayazid, M. Kemp, and S. Misra, “3D flexible needle steering in soft-tissue phantoms using fiber Bragg grating sensors,” in *Proceedings of IEEE International Conference on Robotics and Automation*, pp. 5843–5849, Karlsruhe, Germany, 2013.
- [52] R. J. Roesthuis and S. Misra, “Steering of multisegment continuum manipulators using rigid-link modeling and fbg-based shape sensing,” *IEEE Transactions on Robotics*, vol. 32, no. 2, pp. 372–382, 2016.
- [53] Koninklijke Philips N.V., “Fiber optic real shape (FORS) technology - sparking a new era in device visualization,” philips.com, <https://www.philips.com/a-w/research/research-programs/fors.html> (accessed November 24, 2020).
- [54] Eden Team, “Enhanced Delivery Ecosystem for Neurosurgery in 2020,” eden2020.eu, <https://www.eden2020.eu/> (accessed November 13, 2020).

- [55] **F. Khan**, A. Denasi, D. Barrera, J. Madrigal, S. Sales, and S. Misra, “Multi-core optical fibers with Bragg gratings as shape sensor for flexible medical instruments,” *IEEE Sensors Journal*, vol. 19, no. 14, pp. 5878–5884, 2019.
- [56] **F. Khan**, A. Donder, S. Galvan, F. Rodriguez y Baena, and S. Misra, “Pose measurement of flexible medical instruments using fiber Bragg gratings in multi-core fiber,” *IEEE Sensors Journal*, vol. 20, no. 18, pp. 10 955–10 962, 2020.
- [57] **F. Khan**, D. Barrera, S. Sales, and S. Misra, “Curvature, twist and pose measurements using fiber Bragg gratings in multi-core fiber: A comparative study between helical and straight core fibers,” *Sensors and Actuators A: Physical*, vol. 317, pp. 112 442–112 449, 2021.
- [58] A. Denasi, **F. Khan**, K. J. Boskma, M. Kaya, C. Hennersperger, R. Göbl, M. Tirindelli, N. Navab, and S. Misra, “An observer-based fusion method using multicore optical shape sensors and ultrasound images for magnetically-actuated catheters,” in *Proceedings of IEEE International Conference on Robotics and Automation*, pp. 50-57, Queensland, Australia, 2018.
- [59] **F. Khan**, R. J. Roesthuis, and S. Misra, “Force sensing in continuum manipulators using fiber Bragg grating sensors,” in *Proceedings of IEEE International Conference on Intelligent Robots and Systems*, pp. 2531-2536, British Columbia, Canada, 2017.

Part II

Shape and Pose Sensing

In the previous part, the literature was reviewed and the motivation for the research was presented. This part discusses the theoretical framework developed in order to meet the research goals of this thesis. Chapter 2 gives the algorithms used to acquire the shape and position of a multi-core fiber with FBG sensors. This work is extended in Chapter 3 where in addition to shape and position, the fiber's tip orientation is also acquired. Lastly, Chapter 4 is a comparative study on shape sensing using straight and helical core fibers. This part shows that shape and pose measurements are feasible with FBG sensors. The work described in this part is based on the following peer-reviewed publications:

- **F. Khan**, D. Barrera, S. Sales, and S. Misra, "Curvature, Twist and Pose Measurements using Fiber Bragg Gratings in Multi-Core Fiber: A Comparative Study between Straight and Helical Core Fiber", *Sensors and Actuators A: Physical*, vol. 317, pp. 112442-112449, 2021.
- **F. Khan**, A. Donder, S. Galvan, F. Rodriguez y Baena and S. Misra "Pose Measurement of Flexible Medical Instruments using Fiber Bragg Gratings in Multi-Core Fiber", *IEEE Sensors Journal*, vol. 20, no. 18, pp. 10955-10962, 2020.
- **F. Khan**, A. Denasi, D. Barrera, J. Madrigal, S. Sales, and S. Misra, "Multi-core optical fibers with Bragg gratings as shape sensor for flexible medical instruments", *IEEE Sensors Journal*, vol. 19, no. 14, pp. 5878-5884, 2019.

Chapter 2

Shape Acquisition

Abstract

This chapter presents a technique to reconstruct the shape of a flexible instrument in three dimensional Euclidean space based on data from Fiber Bragg Gratings (FBG) that are inscribed in multi-core fibers. Its main contributions are the application of several multi-core fibers with FBGs as shape sensor for medical instruments and a thorough presentation of the reconstruction technique. The data from the FBG sensors is first converted to strain measurements, which is then used to calculate the curvature and torsion of the fibers. The shape of the instrument is reconstructed using Frenet-Serret equations in conjunction with the calculated curvature and torsion of the instrument. The reconstruction technique is validated with a catheter sensorized with 4 multi-core fibers that have FBG sensors. The catheter is placed in 8 different configurations and the reconstruction is compared to the ground truth. The maximum reconstruction error among all the configurations is found to be 1.05 mm. The results show that shape sensing for flexible medical instruments is feasible with FBG sensors in multi-core fibers.

2.1 Introduction

The spatial information of a medical instrument inside the patient during a procedure is crucial for the accurate manipulation of the instrument. There exist a range of clinical applications which can benefit from the instruments spatial information, such as epidural administration, colonoscopy, biopsies, and cardiac procedures [1,2]. Among the aforementioned applications, in

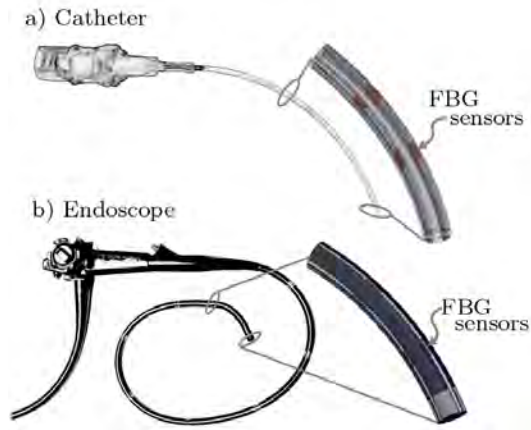


Figure 2.1: Multi-core optical fibers can be placed in numerous flexible medical instruments due to their small size, flexibility, light weight, immunity to electromagnetic interference and compatibility with medical imaging modalities. Fibers with Bragg Gratings (FBG) are shown embedded in a) a catheter and b) an endoscope.

the case of epidural administration procedure, a catheter is inserted into the epidural space in order to deliver drugs for pain relief. In practice, most doctors identify the epidural space based on the resistance felt through the catheter and in some cases ultrasound or fluoroscopy is utilized. However, each method has their drawbacks, the tactile feedback is very subjective, the catheter can be invisible in ultrasound images and the patient is exposed to harmful radiation in fluoroscopy [3, 4]. An alternative to these methods is to use optical sensors in the catheter for its spatial information.

Optical sensors can be used in numerous medical instruments such as endoscopes and catheters as illustrated in Figure 2.1. They are well suited for the medical environment, since they are small in size, flexible, lightweight, immune to electromagnetic interference and compatible with medical imaging modalities [5]. Thus, they have been utilized in numerous studies to provide feedback from medical instruments. They have been used to monitor muscle fatigue, cardiac activities and body temperature [6–8]. In addition, they have been applied in cardiovascular diagnosis, artery pressure detection, artery detection, intra-aortic balloon pumping, prostatic implants, and urology [1, 9]. There are also many patents on medical instruments that use these sensors [10–13]. Particularly, FBG sensors are used as force sensors to recognize the interface between different tissues in order to aid in accu-

rately placing a catheter in the epidural space [14]. They have also been used to display the shape of a colonoscope and the shape of a needle in real-time [2, 15]. Moreover, FBG sensors have been applied to many different shape sensing applications. They have been used for 3D shape recognition of solid objects, shape recognition of flexible morphine wing and curvature detection of a continuum manipulator [16–18]. The studies presented thus far use FBG sensors in single core fiber however FBG sensors can also be present in multi-core fiber. FBGs in multi-core fiber have been shown to work as curvature sensor and 3D shape sensor [19–25]. Multi-core fibers are more expensive than single core fibers, whereas the cross sectional area of the shape sensor with multi-core fibers is smaller than the shape sensor with single core fibers. For certain instruments, such as the one used in this study, multi-core fibers have to be utilized due to the limited space. Moreover, in multi-core fibers the cores are mechanically coupled, the relative distance between the cores remain constant and the cores experience identical temperature. These properties make multi-core fibers more advantageous than single core fiber. Therefore, in this study, Fiber Bragg Grating (FBG) sensors written on multi-core optical fibers are used as shape sensors for flexible instruments.

This study is unique for its application of several multi-core fibers with FBGs as a shape sensor for a catheter. More specifically, four multi-core fibers are used although a single multi-core fiber with 3 or more cores that have FBG sensors is sufficient for reconstructing the shape of a flexible instrument. Redundant number of multi-core fibers increases the reliability of the sensing system against individual FBG sensor failure. A technique is presented in this article to reconstruct the catheter’s center curve based on measurements from the FBG sensors on the four multi-core fibers. The technique is experimentally validated using Plexiglas plates and 3D printed rig which serve as ground truth. The theoretical framework utilized in the study is presented in Section 2.2. This is followed by the description of the experimental setup and the corresponding shape reconstruction results in Section 2.3. Finally, the conclusion is provided in Section 2.4.

2.2 Theoretical Framework

This section presents the theoretical framework utilized to reconstruct the shape of a catheter sensorized by four fibers inscribed with FBG sensors. The shape of the catheter is characterized by its center curve that is described in Section 2.2.3. The proposed reconstruction technique consists of

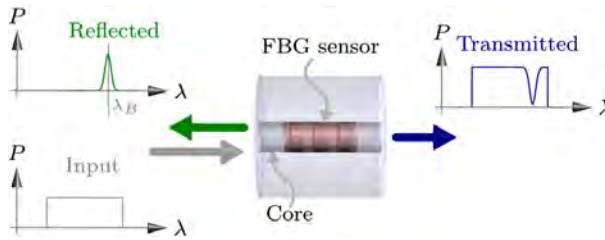


Figure 2.2: A Fiber Bragg Grating (FBG) sensor reflects back a certain range of wavelength, $\lambda \in \mathbb{R}_{>0}$ for a given input and transmits the rest. The Bragg wavelength $\lambda_B \in \mathbb{R}_{>0}$ is the wavelength at which the power $P \in \mathbb{R}_{\geq 0}$ of the reflected spectrum is the highest.

the following four steps. First, the strain on each fiber is calculated using the measurements obtained from the FBG sensors, as presented in Section 2.2.1. Next, the curvature and the torsion of each fiber is calculated using those strains, Section 2.2.2. Then, the curvature and torsion of the catheter's center curve is determined based on the four fibers' curvature and torsion, Section 2.2.3. Lastly, the catheter's center curve is determined using the calculated curvature and torsion in conjunction with the Frenet-Serret equations in Section 2.2.3.

2.2.1 Strain calculation based on FBG sensors

The strain on an individual fiber can be calculated at discretized locations where the FBG sensors are present. An FBG is a periodic or quasi-periodic modulation of the refractive index of the fiber core. This perturbation causes light to be coupled from the incident core mode to the core mode propagated in the opposite direction [26]. Thus, part of the light spectrum is reflected back and the wavelength at which the reflection is the highest is called the Bragg wavelength, $\lambda_B \in \mathbb{R}_{>0}$. Figure 2.2 illustrates an FBG sensor and its working principle.

If the FBG sensor experiences strain or change in temperature, then the Bragg wavelength, λ_B , is shifted. The Bragg wavelength is related to the applied strain and temperature as follows [27]:

$$\frac{d\lambda_B}{\lambda_B} = Sd\epsilon + \Sigma dT, \quad (2.1)$$

where $S \in \mathbb{R}$ is the gauge factor and $\Sigma \in \mathbb{R}$ is the temperature sensitivity. The differentials $d\lambda$, $d\epsilon$ and dT are of the wavelength, strain and tempera-

ture, respectively. Integrating (2.1) results in:

$$\ln \frac{\lambda_B}{\lambda_{B0}} = S(\epsilon - \epsilon_0) + \Sigma(T - T_0), \quad (2.2)$$

where $\epsilon \in \mathbb{R}$ is the strain, $T \in \mathbb{R}$ is the temperature and $\lambda_{B0} \in \mathbb{R}_{>0}$ is the reference Bragg wavelength at the reference strain $\epsilon_0 \in \mathbb{R}$ and reference temperature $T_0 \in \mathbb{R}$. The change in strain and temperature are related to the FBG sensor measurements by (2.2). This relation can be used to obtain the strain when the temperature remains constant i.e. $T = T_0$ and the reference strain (ϵ_0) along with the reference Bragg wavelength (λ_{B0}) are known.

2.2.2 Shape reconstruction for a single multi-core fiber

The shape of a fiber is reconstructed using the curvature and torsion parameters which can be calculated from the strains on the fiber [28]. The fibers used in this study have four cores with multiple sets of FBG sensors. A section of the fiber in pure bending and a set of FBG sensors are shown in Figure 2.3. A set consists for four FBG sensors that are co-located and have the same reference wavelength. The sensor sets are distributed along the length of the fiber, $L \in \mathbb{R}_{>0}$. The location of the sets on the fiber and other associated quantities such as strains are parametrized using the arc length parameter, $s \in \mathbb{R}$ defined in the interval $\Omega \subset \mathbb{R}$ with $\Omega = (0, L)$. The arc length is defined for the neutral axis of the fiber. The relation between the strain ϵ_i on an FBG sensor in core i and the curvature κ is based on mechanics of a bending beam presented in Chapter 6.3 of [28]. The relation is given as:

$$\epsilon_i(s) = -\kappa(s)y_i(s) = -\kappa(s)r_i\cos(\theta_i(s)), \quad (2.3)$$

where $\epsilon_i : \Omega \rightarrow \mathbb{R}$ is the strain, $\kappa : \Omega \rightarrow \mathbb{R}$ is the curvature and $i \in \{a, b, c, d\}$ is the index of the four cores. Further, $y_i : \Omega \rightarrow \mathbb{R}$ is the orthogonal distance between the neutral surface and the FBG sensor on core i , $r_i \in \mathbb{R}_{>0}$ is the radial distance from the center of the fiber cross-section to the FBG sensor on core i and $\theta_i : \Omega \rightarrow (-\pi, \pi]$ is the angle between the curvature direction vector $\boldsymbol{\alpha} : \Omega \rightarrow \mathbb{R}^3$ and r_i (see Figure 2.3). The curvature direction $\boldsymbol{\alpha}(s)$ in this study is a unit vector that lies on the plane of a fiber cross section. Further, it is orthogonal to the neutral surface and it points towards the compressed region of the cross section.

The measurement $\epsilon_{i_m} : \Omega \rightarrow \mathbb{R}$ from the FBG sensor in core i includes the effects of both the change in strain and temperature experienced by the

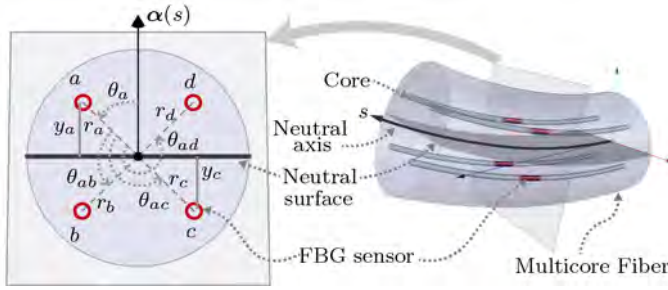


Figure 2.3: Multi-core fiber with one set of Fiber Bragg Grating (FBG) sensors. The arc length of the neutral axis is represented with the variable $s \in \mathbb{R}$ defined in the interval $\Omega \subset \mathbb{R}$ with $\Omega = (0, L)$. The index i for the cores are a, b, c and d , respectively. At a given cross-section with FBG sensors, the curvature direction vector $\boldsymbol{\alpha}(s)$ is orthogonal to the neutral surface. The angle between $\boldsymbol{\alpha}(s)$ and core a is θ_a , whereas the angles between core a and the other cores are θ_{ab}, θ_{ac} and θ_{ad} , respectively. The radial distance from the center of the fiber to the center of the cores are labeled as r_a, r_b, r_c and r_d , respectively. The perpendicular distance from the neutral surface to the cores a and c are y_a and y_c , respectively.

FBG sensor. According to (2.2) the measurement $\epsilon_{i_m}(s)$ is

$$\epsilon_{i_m}(s) = S_i(\epsilon_i(s) - \epsilon_{i0}) + \Sigma_i(T(s) - T_0(s)), \quad (2.4)$$

where the subscript m denotes a measurement. Substituting (2.3) in (2.4) results in

$$\epsilon_{i_m}(s) = S_i(-\kappa(s)r_i \cos(\theta_i(s)) - \epsilon_{i0}) + \Sigma_i(T(s) - T_0(s)). \quad (2.5)$$

In the following derivations, it is assumed that the term $\Sigma_i(T(s) - T_0(s))$ in (2.5) is the same for all the four cores due to the close proximity of the cores. For the ease of the following derivations, the term $\Sigma_i(T(s) - T_0(s))$ is represented by a new variable $\epsilon_t(s)$. In addition, by selecting the reference strain to be zero the following equations apply to the measurements from the sensors in the four cores:

$$\epsilon_{a_m}(s) = -S_a \kappa(s) r_a \cos(\theta_a(s)) + \epsilon_t(s), \quad (2.6)$$

$$\epsilon_{b_m}(s) = -S_b \kappa(s) r_b \cos(\theta_a(s) + \theta_{ab}) + \epsilon_t(s), \quad (2.7)$$

$$\epsilon_{c_m}(s) = -S_c \kappa(s) r_c \cos(\theta_a(s) + \theta_{ac}) + \epsilon_t(s), \quad (2.8)$$

$$\epsilon_{d_m}(s) = -S_d \kappa(s) r_d \cos(\theta_a(s) + \theta_{ad}) + \epsilon_t(s), \quad (2.9)$$

where $\theta_{ab} = \frac{\pi}{2}$, $\theta_{ac} = \pi$ and $\theta_{ad} = \frac{3\pi}{2}$ for the multi-core fiber used in this study. The relations given by (2.6)-(2.9) can be represented in matrix form as follows:

$$\underbrace{\begin{bmatrix} \epsilon_{a_m}(s) \\ \epsilon_{b_m}(s) \\ \epsilon_{c_m}(s) \\ \epsilon_{d_m}(s) \end{bmatrix}}_{\boldsymbol{\epsilon}_m(s)} = \underbrace{\begin{bmatrix} -S_a r_a & 0 & 1 \\ 0 & S_b r_b & 1 \\ S_c r_c & 0 & 1 \\ 0 & -S_d r_d & 1 \end{bmatrix}}_{\mathbf{M}} \underbrace{\begin{bmatrix} \kappa(s) \cos(\theta_a(s)) \\ \kappa(s) \sin(\theta_a(s)) \\ \epsilon_t(s) \end{bmatrix}}_{\mathbf{v}(s)}. \quad (2.10)$$

By solving (2.10) for $\mathbf{v}(s)$, a solution for the angle $\theta_a(s)$ and curvature $\kappa(s)$ can be found. The solution $\mathbf{v}(s)$ from (2.10) can be computed as:

$$\mathbf{v}(s) = \mathbf{M}^\dagger \boldsymbol{\epsilon}_m(s), \quad (2.11)$$

where \mathbf{M}^\dagger is the Moore-Penrose pseudo-inverse of \mathbf{M} . Using the relation (2.11), the curvature $\kappa(s)$, the torsion $\tau(s)$ with $\tau : \Omega \rightarrow \mathbb{R}$ and the angle $\theta_a(s)$ can be obtained as follows:

$$\kappa(s) = \sqrt{v_1^2(s) + v_2^2(s)}, \quad (2.12)$$

$$\theta_a(s) = \text{atan2}(v_2(s), v_1(s)), \quad (2.13)$$

$$\tau(s) = \frac{d\theta_a(s)}{ds}. \quad (2.14)$$

In (2.12), the positive solution is selected for the curvature because the Frenet-Serret formulation assumes $\kappa > 0$. The sign of the curvature determines the direction of bending in a planar curve, however for 3D curves the torsion is used for the bending direction. The derivative operator introduced for the torsion parameter $\tau(s)$ in (2.14) can be numerically approximated as follows:

$$\tau(s) \approx \frac{\theta_a(s) - \theta_a(s - \Delta s)}{\Delta s} \quad (2.15)$$

where Δs is the difference in the arc length between the two consecutive FBG sensor sets. Consequently, the curvature and torsion for a single fiber can be found using (2.12) and (2.14) at the locations where the FBG sensor sets are present.

2.2.3 Center curve reconstruction for a catheter

The curvature (2.12) and torsion (2.14) derived for an individual fiber in the previous section are used to obtain the curvature and torsion of the center

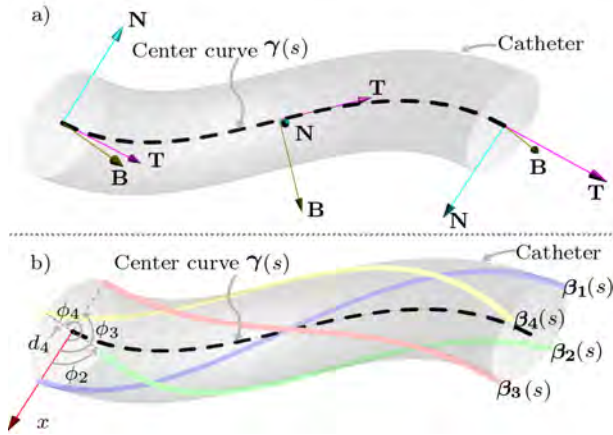


Figure 2.4: a) The center curve of the catheter with the Frenet-Serret frames
 b) Catheter with four multi-core fibers where each fiber is represented with a curve $\beta_1 : \Omega \rightarrow \mathbb{R}^3$, $\beta_2 : \Omega \rightarrow \mathbb{R}^3$, $\beta_3 : \Omega \rightarrow \mathbb{R}^3$ and $\beta_4 : \Omega \rightarrow \mathbb{R}^3$, respectively. The distance from the center of the catheter to fiber 4 is $d_4 \in \mathbb{R}_{>0}$. The angles from the reference x -axis to fiber 2, 3, and 4 are ϕ_2 , ϕ_3 and ϕ_4 , respectively. The center curve of the catheter is $\gamma(s)$ where s is the arc length parameter of the curve.

curve of the catheter shown in Figure 2.4. In the following derivation, it is assumed that the center curve is represented as a unit speed space curve that is smooth and has a non-zero curvature along its arc length [29]. This curve can be reconstructed with the knowledge of its own curvature $\tilde{\kappa} : \Omega \rightarrow \mathbb{R}$ and torsion $\tilde{\tau} : \Omega \rightarrow \mathbb{R}$ parameters using the Frenet-Serret equations as follows:

$$\frac{d\gamma(s)}{ds} = \mathbf{T}(s), \quad (2.16)$$

$$\frac{d\mathbf{T}(s)}{ds} = \tilde{\kappa}(s)\mathbf{N}(s), \quad (2.17)$$

$$\frac{d\mathbf{N}(s)}{ds} = -\tilde{\kappa}(s)\mathbf{T}(s) + \tilde{\tau}(s)\mathbf{B}(s), \quad (2.18)$$

$$\frac{d\mathbf{B}(s)}{ds} = -\tilde{\tau}(s)\mathbf{N}(s), \quad (2.19)$$

where $\gamma : \Omega \rightarrow \mathbb{R}^3$ is the position vector, $\mathbf{T} : \Omega \rightarrow \mathbb{R}^3$, $\mathbf{N} : \Omega \rightarrow \mathbb{R}^3$ and $\mathbf{B} : \Omega \rightarrow \mathbb{R}^3$ are the tangent, the normal and the bi-normal orthogonal vectors, respectively. The relations (2.16)-(2.19) can be rewritten in matrix

form as follows:

$$\frac{d}{ds}\mathbf{X}(s) = \mathbf{X}(s)\mathbf{A}(s), \quad (2.20)$$

where the pose $\mathbf{X}(s) : \Omega \rightarrow SE(3)$ and the twist $\mathbf{A}(s) : \Omega \rightarrow \mathfrak{se}(3)$ are given by:

$$\mathbf{X}(s) = \begin{bmatrix} \mathbf{R}(s) & \boldsymbol{\gamma}(s) \\ \mathbf{0}_3^T & 1 \end{bmatrix} = \begin{bmatrix} \mathbf{T}(s) & \mathbf{N}(s) & \mathbf{B}(s) & \boldsymbol{\gamma}(s) \\ 0 & 0 & 0 & 1 \end{bmatrix} \quad (2.21)$$

$$\mathbf{A}(s) = \begin{bmatrix} 0 & -\tilde{\kappa}(s) & 0 & 1 \\ \tilde{\kappa}(s) & 0 & -\tilde{\tau}(s) & 0 \\ 0 & \tilde{\tau}(s) & 0 & 0 \\ 0 & 0 & 0 & 0 \end{bmatrix}. \quad (2.22)$$

In (2.21), $\mathbf{R}(s) = [\mathbf{T}(s) \ \mathbf{N}(s) \ \mathbf{B}(s)]$ with $\mathbf{R} : \Omega \rightarrow SO(3)$ describes the orthonormal frame in terms of the vectors $\mathbf{T}(s)$, $\mathbf{N}(s)$, and $\mathbf{B}(s)$ [30]. Further, $\mathbf{0}_3$ is a three dimensional vector of zeros. The aforementioned frame is illustrated at three different locations on the center curve of the catheter in Figure 2.4a. In order to reconstruct the center curve described by the position vector $\boldsymbol{\gamma}(s)$, the relation (2.20) should be solved. The solution to (2.20) can be obtained assuming that $\mathbf{A}(s)$ is held constant between two consecutive discretized locations on the center curve. Thus, Equation 2.20 can be discretized as:

$$\mathbf{X}(s + \Delta s) = \mathbf{X}(s) \exp(\mathbf{A}(s)\Delta s). \quad (2.23)$$

Consequently, the position vector $\boldsymbol{\gamma}(s)$ can be extracted from the last column of the solution given by (2.23). The center curve of the catheter described by the vector $\boldsymbol{\gamma}(s)$ and the shape of each individual fiber described by $\boldsymbol{\beta}_j : \Omega \rightarrow \mathbb{R}^3$ (see Figure 2.4b) are related as follows:

$$\boldsymbol{\beta}_j(s) = \boldsymbol{\gamma}(s) + d_j(-\cos(\phi_j)\mathbf{N}(s) + \sin(\phi_j)\mathbf{B}(s)) \quad (2.24)$$

where $j \in \{1, 2, 3, 4\}$ is the index of the fiber. Further, $d_j \in \mathbb{R}_{>0}$ is the distance from the center of the catheter to the j^{th} fiber's center and ϕ_j is the angle between the x axis and the vector from the center of the catheter to the center of the j^{th} fiber (see Figure 2.4b) [29]. For a given small d_j in (2.24), $\boldsymbol{\beta}_j(s) \approx \boldsymbol{\gamma}(s)$ holds. Consequently, the curvature and torsion calculated for the fibers can be used for the reconstruction of the center curve of the catheter.

The theoretical framework described throughout the Section 2.2 can be implemented using the Algorithms 1, 2 and 3, respectively. The following

algorithms are described for the case of 6 FBG sensor sets and 118 interpolation points. However, they can be generalized to arbitrary numbers of FBG sensor sets and interpolation points.

Algorithm 1 Reconstruction of the center curve of the catheter. Input λ_i is a 4×6 matrix; each column is the data from one FBG set on the i^{th} fiber. Output γ is a 3×118 matrix that holds the 3D co-ordinates of the 118 points of the catheter’s center curve. Variables κ_i , τ_i , κ_{cath} and τ_{cath} are 1×6 vectors. Variables κ_{interp} , τ_{interp} and l are 1×118 vectors. X_0 is a 4×4 matrix

Input: λ_i where $i = (1, 2, 3, 4)$

Output: γ

ReconstructCath:

- 1: **for** $i = 1$ to 4 **do**
 - 2: $[\kappa_i, \tau_i] \leftarrow \text{getShape}(\lambda_i)$
 - 3: **end for**
 - 4: $\kappa_{cath} \leftarrow \text{mean}(\kappa_1, \kappa_2, \kappa_3, \kappa_4)$
 - 5: $\tau_{cath} \leftarrow \text{mean}(\tau_1, \tau_2, \tau_3, \tau_4)$
 - 6: $\kappa_{interp} \leftarrow$ linear interpolation κ_{cath}
 - 7: $\tau_{interp} \leftarrow$ linear interpolation τ_{cath}
 - 8: $l \leftarrow$ points on catheter center curve at which the values of κ_{cath} and τ_{cath} are interpolated
 - 9: $X_0 \leftarrow$ initial condition
 - 10: $\gamma \leftarrow \text{reconstruct}(\kappa_{interp}, \tau_{interp}, l, X_0)$
 - 11: **return** γ
-

2.3 Experiments

The reconstruction technique presented in Section 2.2 is validated with experimental setup that is described in Section 2.3.1 and the results are given in Section 2.3.2.

2.3.1 Experimental setup

The hardware used in the experiments is shown in Figure 2.5. The catheter is 2.5 mm in diameter and has 4 segments that are interlocked and the segments can slide relative to each other [32]. Every segment has a channel, thus four multi-core fibers can be placed in the catheter. The fibers have four cores that are straight and in a cross sectional view of the fiber the

Algorithm 2 The *getShape* function in Algorithm 1. Input λ is 4×6 matrix, each column is the data from one FBG set on the fiber. Output κ and τ are 1×6 vectors, the i^{th} element is the curvature and torsion value at the i^{th} FBG set location on the fiber. The value $r_a = r_b = r_c = r_d = 25.46 \mu\text{m}$, this is from the manufacture's datasheet for the fiber. The strain gauge factor $S_a = S_b = S_c = S_d = 0.777$ that is the default value from the interrogator's user manual [31].

Input: λ

Output: κ, τ

getShape:

```

1: for  $j = 1$  to 6 do
2:   for  $i = 1$  to 4 do
3:      $\epsilon_m(i) \leftarrow \ln \frac{\lambda(i, j)}{\lambda_{B0}(i, j)}$ 
4:   end for
5:    $\kappa(j) \leftarrow$  solution to (2.12)
6:    $\tau(j) \leftarrow$  solution to (2.15)
7: end for
8: return [  $\kappa, \tau$  ]
```

cores fall on the corners of a $36 \mu\text{m}$ wide square. There are 6 sets of 10 mm long FBG sensors that are equally spaced over a distance of 118 mm on every fiber. A set consists of 4 FBG sensors, one on each core, with the same reference Bragg wavelength. The sets are inscribed using continuous wave frequency-doubled Argon-ion laser and a phase mask technique. The FBG sensors are simultaneously inscribed in all the cores, as a result the FBG sensors in all cores are co-located and have the same wavelength. The reference Bragg wavelength of the FBG sensors is unique for every set. The data from the FBG sensors of one set is required for the curvature and torsion calculations. Thus, every fiber has 6 locations where the curvature and torsion can be calculated. The fan-out box holds four fan-outs, each fan-out connects the 4 cores of a multi-core fiber to four single core fibers. The 16 outputs from the fan-out box are merged to 4 outputs using four 1×4 optical couplers in order to measure them using the channels of the interrogator. Lastly, the interrogator is the device which provides the light source and measures the reflected light from the FBGs in the fibers.

The catheter is designed by the Mechatronics In Medicine Lab (London, United Kingdom) and produced by Xograph (Stonehouse, United Kingdom). The FBG sensors are inscribed on the multi-core fiber in the iTeam

Algorithm 3 The *reconstruct* function in Algorithm 1. The inputs $\boldsymbol{\kappa}$, $\boldsymbol{\tau}$, \mathbf{l} are 1×118 vectors. $\boldsymbol{\kappa}$ and $\boldsymbol{\tau}$ contain the curvature and torsion of the catheter’s center curve at the arclength given in \mathbf{l} , respectively. \mathbf{X}_0 is a 4×4 matrix that holds the initial value of the catheter’s center curve.

Input: $\boldsymbol{\kappa}$, $\boldsymbol{\tau}$, \mathbf{l} , \mathbf{X}_0

Output: $\boldsymbol{\rho}$

reconstruct:

```

1:  $\mathbf{X}(1) \leftarrow \mathbf{X}_0$ 
2:  $\boldsymbol{\rho} \leftarrow$  the fourth column of  $\mathbf{X}(1)$ 
3: for  $i = 1$  to 118 do
4:    $\mathbf{A} \leftarrow \begin{bmatrix} 0 & -\tilde{\kappa}(i) & 0 & 1 \\ \tilde{\kappa}(i) & 0 & -\tilde{\tau}(i) & 0 \\ 0 & \tilde{\tau}(i) & 0 & 0 \\ 0 & 0 & 0 & 0 \end{bmatrix}$  from (2.22)
5:   if  $i > 1$  then
6:      $\delta \leftarrow \mathbf{l}(i) - \mathbf{l}(i - 1)$ 
7:   else
8:      $\delta \leftarrow 1$ 
9:   end if
10:   $\mathbf{X}(i + \delta) \leftarrow \mathbf{X}(i) \exp(\mathbf{A}\delta)$  from (2.23)
11:   $\boldsymbol{\rho}(i + \delta) \leftarrow$  the fourth column of  $\mathbf{X}(i + \delta)$ 
12: end for
13: return  $\boldsymbol{\rho}$ 

```

lab (Valencia, Spain). The multi-core fibers and the fan-outs are from Fibercore (Southampton Science Park, United Kingdom) and the product number is FAN-4C and SM-4C1500, respectively. The optical couplers are from Newport Corporation (California, USA) with the product number F-CPL-B14350-FCAPC. The model of the interrogator is FBG-scan 840D from FBGS International NV (Geel, Belgium).

The catheter is sensorized by inserting four multi-core fibers into the channels of the catheter’s segments and fixing the fibers at the base of the catheter. The experiments to validate the reconstruction procedure consists of placing the sensorized catheter in known configurations and observing the error between the known configuration and the reconstructed catheter shape. The values of curvature and torsion in the configurations were selected such that they are similar to the values expected in future in-vitro and ex-vivo studies. Past experiments with similar catheters show

Table 2.1: Description of the ground truth configurations. C1 and C2 are planar curves with constant curvature. C3 - C5 are planar curves and the curvature increases linearly along the arc length. C6 - C8 are three dimensional curves with constant curvature and constant torsion.

Config	Curvature (mm^{-1})	Torsion (mm^{-1})
C1	constant: 0.0057	constant: 0
C2	constant: 0.0020	constant: 0
C3	linearly varying: $4e^{-3}$ to $12.5e^{-3}$	constant: 0
C4	linearly varying: $4e^{-3}$ to $10e^{-3}$	constant: 0
C5	linearly varying: $4e^{-3}$ to $8.3e^{-3}$	constant: 0
C6	constant: $16.7e^{-3}$	constant: $2.77e^{-4}$
C7	constant: $14.3e^{-3}$	constant: $6.11e^{-4}$
C8	constant: $12.5e^{-3}$	constant: $3.12e^{-4}$

that it can take on curvatures in the range of 0.002 mm^{-1} to 0.02 mm^{-1} ; thus, the curvature values within that range are selected for the configurations. The catheter is expected to have minimal torsion as a result small torsion values are used in this study [33]. Table 2.1 gives the description of the eight configurations used for validating the reconstruction procedure

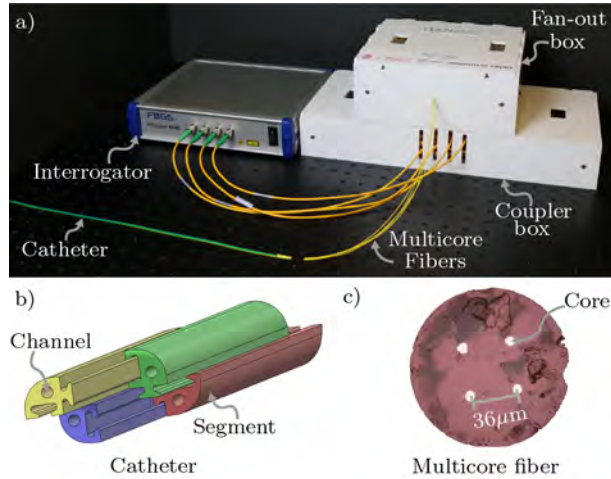


Figure 2.5: a) The experimental setup consists of an interrogator, a coupler box, a fan-out box, multi-core fibers and a multi-segment catheter. b) The catheter consists of four segments and channels for multi-core fiber. c) Photograph of the multi-core fiber's cross sectional view under a microscope.

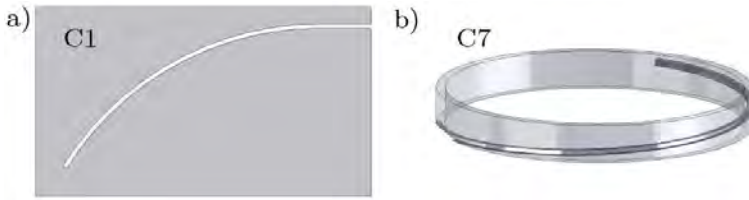


Figure 2.6: Representative images of the ground truth configurations. a) Computer Aided Design (CAD) model of configuration C1, which is a planar curve with a constant curvature of 0.0057 mm^{-1} . Configurations C1 till C5 are created by laser cutting Plexiglas plates. b) CAD model of configuration C7, which is a curve with constant curvature of $14.3e^{-3}$ and constant torsion of $6.11e^{-4}$. Configurations C6 till C8 are 3D printed.

and the Computer Aided Design (CAD) of configurations C1 and C7 are illustrated in Figure 2.6.

2.3.2 Shape Reconstruction Results

The sensorized catheter is placed in all of the configurations described in Table 2.1. For every configuration the data from the interrogator is collected and the catheter's center curve is reconstructed offline in MATLAB according to Algorithm 1. The reconstruction of the fiber and the catheter is compared to the ground truth via absolute error $r_e \in \mathbb{R}_{\geq 0}$, normalized

Table 2.2: Catheter Reconstruction errors. $\bar{r}_e = \max(r_e)$ and $\bar{r}_{en} = \max(r_{en})$ where r_e and r_{en} are from (2.25) and (2.26), respectively. r_{em} is from (2.27).

Config	C1	C2	C3	C4	C5	C6	C7	C8
\bar{r}_e (mm)	0.96	0.19	0.54	0.82	1.05	0.49	0.84	0.41
\bar{r}_{en} (%)	0.9	0.2	0.8	0.7	0.9	0.4	0.7	0.4
r_{em} (mm)	0.44	0.12	0.35	0.13	0.21	0.13	0.23	0.12

error $r_{en} \in \mathbb{R}_{\geq 0}$ and mean error $r_{em} \in \mathbb{R}_{\geq 0}$ which is calculated as follows:

$$r_e(k) = \|\mathbf{r}_{gt}(k) - \boldsymbol{\gamma}(k)\|, \quad (2.25)$$

$$r_{en}(k) = \frac{r_e(k)}{k}, \quad (2.26)$$

$$r_{em} = \frac{1}{n} \sum_{k=1}^n r_e(k), \quad (2.27)$$

where, $k \in \mathbb{Z}_{\geq 0}$ representing the 118 points along the arc length at which the error calculation is conducted, $\mathbf{r}_{gt} \in \mathbb{R}^3$ is the ground truth curve and $\boldsymbol{\gamma}$ is the reconstruction based on proposed technique from Section 2.2. The reconstruction and the error r_e in reconstruction over the arc length for the catheter is shown in Figure 2.7 and the maximum error measures $\bar{r}_e = \max(r_e)$ and $\bar{r}_{en} = \max(r_{en})$ in conjunction with the mean error for catheter is given in Table 2.2.

The reconstruction error r_e as defined in (2.25) is shown in Figure 2.7b and 2.7d. The error increases with the arc length because the reconstruction is conducted by numerical integration thus the error accumulates. However, the maximum absolute error and maximum mean error in the 8 configurations is 1.05 mm and 0.44 mm, respectively. This error can be due to the difference between the catheter center curve and the configuration curve caused by placement inaccuracies during the experiments. It could also be due to misalignment in the longitudinal axis of the FBGs in the four fibers due to misplacement of the fibers in the catheter. Lastly, since the fibers were not fixed along the length of the catheter the twist experienced by the catheter may not be transferred completely to the fibers.

2.4 Conclusions

A shape reconstruction technique which uses redundant number of multi-core fibers with FBG sensors as shape sensor for flexible medical instruments is proposed in this work. The technique is validated on a multi-segment catheter where each segment contains a multi-core fiber with FBG sensors inscribed on it. The presence of several multi-core fibers increases the reliability of the shape sensing system against sensor failure. The proposed technique is experimentally validated for 8 different configurations where a maximum reconstruction error of 1.05 mm is observed. Further, it can be deduced that shape sensing using several multi-core fibers for flexible medical instruments is feasible.

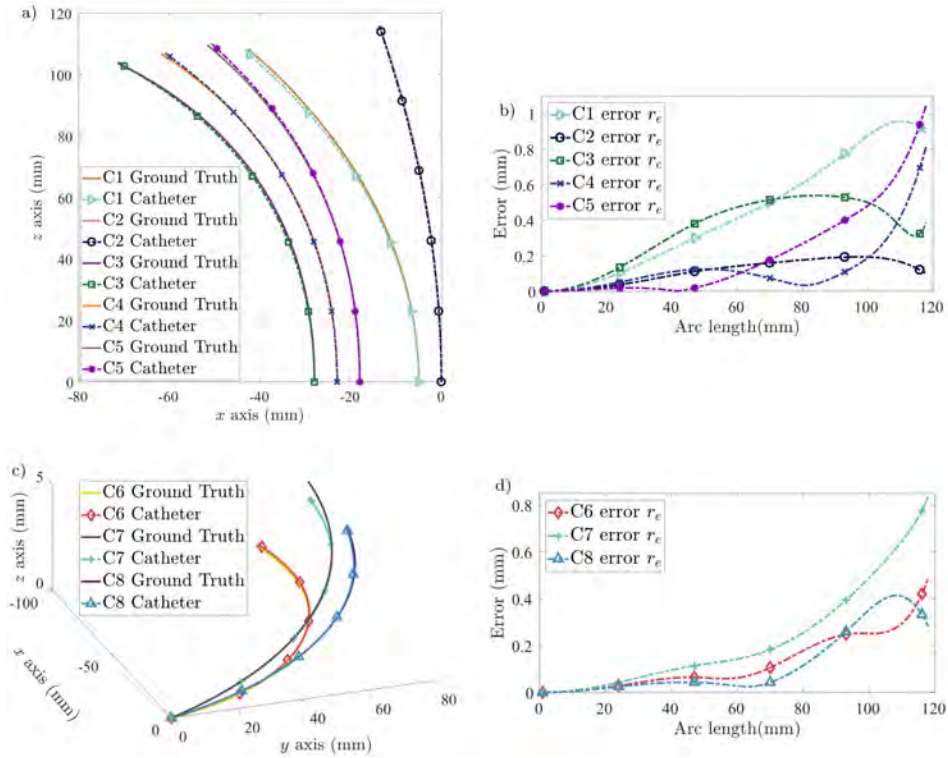


Figure 2.7: a) Reconstruction plots of the planar curves, configuration C1-C5. b) The error r_e plot along the arc length of the catheter for the planar curves, configuration C1-C5. c) Reconstruction plots of the 3D curves, configuration C6-C8. d) The error r_e plot along the arc length of the catheter for the 3D curves, configuration C6-C8.

Acknowledgments

The authors would like to thank the Mechatronics In Medicine Lab (Imperial College London) for providing the computer aided design and the samples of the catheter. We appreciate the help of Luigi Capuano (Surface technology and tribology group, University of Twente) for generating the cross sectional photograph of the multi-core fiber.

References

- [1] D. Tosi, E. Schena, C. Molardi, and S. Korganbayev, "Fiber optic sensors for sub-centimeter spatially resolved measurements: Review and biomedical applications," *Optical Fiber Technology*, vol. 43, pp. 6 – 19, 2018.
- [2] Y. Xinhua, W. Mingjun, and C. Xiaomin, "Deformation sensing of colonoscope on fbg sensor net," *TELKOMNIKA : Indonesian Journal of Electrical Engineering*, vol. 10, pp. 2253–2260, 2012.
- [3] M. Nikooseresht, M. Hashemi, S. A. Mohajerani, F. Shahandeh, and M. Agah, "Ultrasound as a screening tool for performing caudal epidural injections," *Iranian Journal of Radiology*, vol. 11, no. 2, 2014.
- [4] H. Gharries, "Is ultrasound guided spine injection safe," *Journal of Anesthesia & Critical Care: Open Access*, vol. 10, no. 4, pp. 131–138, 2018.
- [5] V. Mishra, N. Singh, U. Tiwari, and P. Kapur, "Fiber grating sensors in medicine: Current and emerging applications," *Sensors and Actuators A: Physical*, vol. 167, no. 2, pp. 279 – 290, 2011.
- [6] D. Polito, M. A. Caponero, A. Polimadei, P. Saccomandi, C. Massaroni, S. Silvestri, and E. Schena, "A needle like probe for temperature monitoring during laser ablation based on fiber bragg grating: Manufacturing and characterization," *Journal of Medical Devices*, vol. 9, no. 4, 2015.
- [7] K. Chethana, A. S. G. Prasad, S. N. Omkar, and S. Asokan, "Fiber bragg grating sensor based device for simultaneous measurement of respiratory and cardiac activities," *Journal of Biophotonics*, vol. 10, no. 2, pp. 278 – 285, 2017.
- [8] P. F. Nascimento, A. P. G. O. Franco, R. Fiorin, M. A. de Souza, H. J. Kalinowski, and I. Abe, "Case study of muscle fatigue in para-functional patient using occlusal device with fiber bragg grating sensors," *Journal of microwaves, optoelectronics and electromagnetic applications*, vol. 17, no. 2, pp. 306 – 318, 2018.
- [9] S. C. M. Ho, W. Li, M. Razavi, and G. Song, "Fiber bragg grating based arterial localization device," *Smart Materials and Structures*, vol. 26, pp. 1–10, 2017.

- [10] G. W. T. Hooft, “Optical shape sensing system and method for sensing a position and/or shape of a medical device using backscatter reflectometry,” Patent US20 180 128 600A1, June 08, 2016.
- [11] G. Leo, N. Aeby, and D. Inaudi, “Medical apparatus system having optical fiber sensing capability,” Patent US9 907 618B2, Jan 25, 2012.
- [12] D. K. Gifford, F. Barbagli, S. Y. Chang, A. B. Kowshik, O. J. Wagner, M. D. Paris, and M. E. Froggatt, “Force sensing in a distal region of an instrument including single-core or multi-core optical fiber,” Patent US20 180 128 599A1, March 06, 2018.
- [13] T. Bosselmann and O. Schuetz, “Medical instrument for insertion into an examination subject, and medical examination/treatment device employing same,” Patent US6 470 205B2, Oct 22, 2002.
- [14] B. Carotenuto, A. Micco, A. Ricciardi, E. Amorizzo, M. Mercieri, A. Cutolo, and A. Cusano, “Optical guidance systems for epidural space identification,” *IEEE Journal of Selected Topics in Quantum Electronics*, vol. 23, no. 2, pp. 371–379, 2017.
- [15] R. J. Roesthuis, M. Kemp, J. J. van den Dobbelen, and S. Misra, “Three-dimensional needle shape reconstruction using an array of fiber bragg grating sensors,” *IEEE/ASME Transactions on Mechatronics*, vol. 19, no. 4, pp. 1115–1126, Aug 2014.
- [16] L. Xu, J. Ge, J. H. Patel, and M. P. Fok, “3-dimensional soft shape sensor based on dual-layer orthogonal fiber bragg grating mesh,” in *Proceedings of the Optical Fiber Communications Conference and Exhibition (OFC)*, pp. 1-3, California, USA, March 2017.
- [17] G. Sun, Y. Wu, H. Li, and L. Zhu, “3d shape sensing of flexible morphing wing using fiber bragg grating sensing method,” *Optik*, vol. 156, pp. 83 – 92, 2018.
- [18] S. Sefati, M. Pozin, F. Alambeigi, I. Iordachita, R. H. Taylor, and M. Armand, “A highly sensitive fiber bragg grating shape sensor for continuum manipulators with large deflections,” in *Proceedings of IEEE Sensors*, pp. 1-3, Glasgow, UK, Oct 2017.
- [19] F. M. Araújo, L. A. Ferreira, and J. L. Santos, “Simultaneous determination of curvature, plane of curvature, and temperature by use of a miniaturized sensing head based on fiber bragg gratings,” *Applied Optics*, vol. 41, no. 13, pp. 2401–2407, 2002.

-
- [20] D. Zheng, J. Madrigal, H. Chen, D. Barrera, and S. Sales, "Multicore fiber-bragg-grating-based directional curvature sensor interrogated by a broadband source with a sinusoidal spectrum," *Optics Letters*, vol. 42, no. 18, pp. 3710–3713, 2017.
- [21] G. M. H. Flockhart, W. N. MacPherson, J. S. Barton, J. D. C. Jones, L. Zhang, and I. Bennion, "Two-axis bend measurement with bragg gratings in multicore optical fiber," *Optics Letters*, vol. 28, no. 6, pp. 387–389, 2003.
- [22] J. P. Moore and M. D. Rogge, "Shape sensing using multi-core fiber optic cable and parametric curve solutions," *Optics Express*, vol. 20, no. 3, pp. 2967–2973, 2012.
- [23] J. P. Moore, "Shape sensing using multi-core fiber," in *Proceedings of Optical Fiber Communications Conference and Exhibition (OFC)*, pp.1-3, California, USA, March 2015.
- [24] D. Barrera, I. Gasulla, and S. Sales, "Multipoint two-dimensional curvature optical fiber sensor based on a nontwisted homogeneous four-core fiber," *Journal of Lightwave Technology*, vol. 33, no. 12, pp. 2445–2450, 2015.
- [25] A. Denasi, **F. Khan**, K. J. Boskma, M. Kaya, C. Hennersperger, R. Göbl, M. Tirindelli, N. Navab, and S. Misra, "An observer-based fusion method using multicore optical shape sensors and ultrasound images for magnetically-actuated catheters," in *Proceedings of the IEEE International Conference on Robotics and Automation (ICRA)*, pp. 50-57, Brisbane, Australia, May 2018.
- [26] K. O. Hill and G. Meltz, "Fiber bragg grating technology fundamentals and overview," *Journal of Lightwave Technology*, vol. 15, no. 8, pp. 1263–1276, 1997.
- [27] J. V. Roosbroeck, C. Chojetzki, J. Vlekken, E. Voet, and M. Voet, "A new methodology for fiber optic strain gage measurements and its characterization," in *Proceedings of the SENSOR+TEST Conferences*, vol. OPTO 2 - Optical Fiber Sensors, pp. 59 - 64, Nürnberg, Germany, May 2009.
- [28] R. C. Hibbeler, *Mechanics of materials*, 8th ed. Upper Saddle River, New Jersey, United States: Pearson Prentice Hall, 2011.

- [29] A. Gray, *Modern Differential Geometry of Curves and Surfaces with Mathematica*. Boca Raton, Florida, United States of America: Chapman & Hall/CRC, 2006.
- [30] S. Patil, J. Pan, P. Abbeel, and K. Goldberg, “Planning curvature and torsion constrained ribbons in 3d with application to intracavitary brachytherapy,” *IEEE Transactions on Automation Science and Engineering*, vol. 12, no. 4, pp. 1332–1345, 2015.
- [31] *Manual ‘ILLumiSense’ software*, Version 2.3, FBGS International, Bell Telephonaan 2H, Geel Belgium.
- [32] A. Leibinge, M. J. Oldfield, and F. B. Rodriguez, “Minimally disruptive needle insertion: a biologically inspired solution,” *INTERFACE FOCUS*, vol. 6, no. 3, 2016.
- [33] L. Frasson, F. Ferroni, S. Y. Ko, G. Dogangil, and F. Rodriguez y Baena, “Experimental evaluation of a novel steerable probe with a programmable bevel tip inspired by nature,” *Journal of Robotic Surgery*, vol. 6, no. 3, pp. 189–197, 2012.

Chapter 3

Pose Measurement

Abstract

Accurate navigation of flexible medical instruments like catheters require the knowledge of its pose, that is its position and orientation. In this chapter multi-core fibers inscribed with fiber Bragg gratings (FBG) are utilized as sensors to measure the pose of a multi-segment catheter. A reconstruction technique that provides the pose of such a fiber is presented. First, the measurement from the Bragg gratings are converted to strain then the curvature is deduced based on those strain calculations. Next, the curvature and the Bishop frame equations are used to reconstruct the fiber. This technique is validated through experiments where the mean error in position and orientation is observed to be less than 4.69 mm and 6.48 degrees, respectively. The main contributions of the study are the use of Bishop frames in the reconstruction and the experimental validation of the acquired pose.

3.1 Introduction

Flexible medical instruments are frequently used for procedures in cardiology and urology. Accurate navigation of these instruments require spatial information such as the pose, as shown in Figure 3.1. Conventionally, fluoroscopy or ultrasound are used to monitor these instruments, even though both methods have their drawbacks [1]. Fluoroscopy exposes the patient to contrast agents and to radiation. In addition, the workflow of the procedure is disrupted to allow the medical personnel time to retreat during imaging. On the other hand, ultrasound images have low resolution and

the instruments can cause artifacts [2]. Thus, there is a need to develop imaging and other sensing techniques to acquire the spatial information of flexible instruments.

In the literature there are studies that used endoscopic images for retrieving spatial information of flexible instruments. Relink *et al.* used markers on an instrument and a state estimator to acquire the position of the instrument [3]. Cabaras *et al.* used feature detection along with learning methods to detect the pose of a flexible instrument from monocular endoscopic images [4]. Although these studies show the feasibility of acquiring the instrument tip position from endoscopic images; they require an unobstructed view of the surgical site. Thus, they are difficult to use in practice and are applicable only to procedures that use endoscopes. An alternative technology that mitigates the requirement of unobstructed view is electromagnetic (EM) tracking. However, it has a limited workspace and the tracking accuracy degrades significantly in the presence of electronic and metallic instruments [5]. Thus, EM tracking is better suited for controlled environments than clinical settings.

Another approach for acquiring spatial information is using optical fibers. This is an attractive approach due to the compatibility of the sensors with the medical environment. Optical fibers are biocompatible, nontoxic, immune to electromagnetic interference and sterilizable [6]. In addition, they are small and highly flexible, and thus can be easily integrated into medical instruments [1] [7]. Sareh *et al.* have used the bend sensitivity of optical fibers to get the pose of the instrument tip [8]. This approach leads to low-cost sensing hardware, but multiple fibers are required that must be routed in a specific manner and it has a complex calibration procedure. The required routing renders it inapplicable to instruments like catheters and needles. These issues can be mitigated by employing fiber Bragg grating (FBG) sensors in the optical fibers.

Moore *et al.* calculated the shape of a multi-core fiber with FBG sensors using Frenet-Serret equations [9]. Numerous other studies have used FBG sensors for sensing shape of flexible instruments such as colonoscope, needle and catheter. Xinhua *et al.* acquired the shape of a colonoscope from optical fibers with FBG sensors in order to reduce the probability of loop formation during colonoscopy [10]. Park *et al.* placed optical fibers with two sets of FBG sensors on a needle to provide tip deflection, bend profile and temperature compensation [11]. Roesthuis *et al.* acquired the 3D shape of a needle using four sets of FBG sensors in optical fibers [12]. Khan *et al.* reconstructed the shape of a multi-segment catheter in 3D space

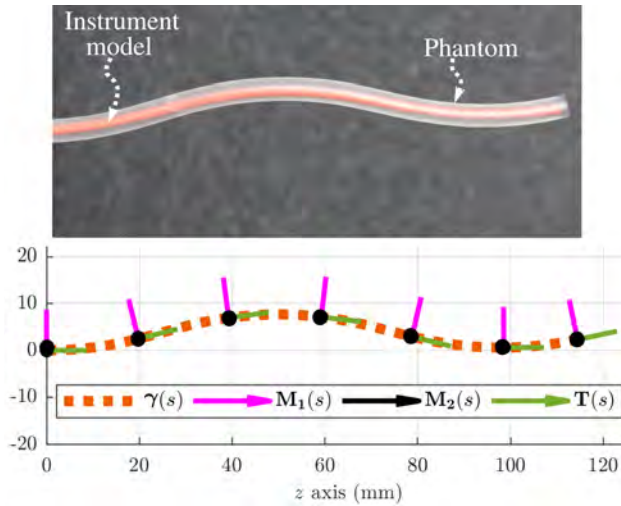


Figure 3.1: Top: A flexible instrument model placed in a vascular phantom. Bottom: Ideal reconstruction of the instrument along the arc length s with position given as a curve, $\gamma(s)$, and the orientation as a frame $\{\mathbf{M}_1(s), \mathbf{M}_2(s), \mathbf{T}(s)\}$.

using multi-core fibers with six sets of FBGs in each fiber [13]. Lastly, Henken *et al.* calculated the needle tip deflection based on strains derived from measurements from two sets of FBG sensors [14]. Nevertheless, these studies have focused on acquiring only the position of the instrument.

The study presented in this chapter extends the use of FBG sensors for acquiring the orientation of an instrument in addition to its position. This information can be utilized for improving the navigation accuracy of flexible medical instruments. The sensors are written in multi-core fibers instead of being written on several single-core fibers due to the space restriction in these instruments. The contributions of this study include the use of Bishop frames in the reconstruction and validation of the acquired pose. The reconstruction technique is described in Section 3.2, followed by the experiments, discussion and conclusion in Section 3.3, 3.4 and 3.5, respectively.

3.2 Theory

This section outlines the technique for reconstructing a multi-core fiber with FBG sensors. The fiber is modeled as a regular unit-speed space curve that is reconstructed in Euclidean space using curvature vectors and Bishop frame equations [15] [16]. The curvature vectors of the fiber are calculated

at every FBG sensor set using strains that are derived from the wavelength measurements of the sensors in the set. Description of FBG sensor and the derivation of strain values is given in Section 3.2.1, followed by an explanation of the curvature vector calculation in Section 3.2.2. Lastly, the reconstruction using Bishop frame equations is presented in Section 3.2.3.

3.2.1 Fiber Bragg Grating for Strain Measurement

An FBG reflects back a narrow band of wavelengths from the optical input and transmits the rest. The reflection is due to the grating being a periodic variation in the refractive index of the fiber over a short segment. The properties of the grating are altered by strain and temperature; as a result the reflected wavelength band shifts when a change in strain or change in temperature is experienced by the grating [17]. The wavelength which has the highest reflection is called the Bragg wavelength, $\lambda_B \in \mathbb{R}_{>0}$. It is related to strain and temperature on the grating according to the following equation [18]:

$$\ln \frac{\lambda_B}{\lambda_{B0}} = S(\epsilon - \epsilon_0) + \Sigma(T - T_0), \quad (3.1)$$

where, $S \in \mathbb{R}$ is the gauge factor; $\Sigma \in \mathbb{R}$ is the temperature sensitivity; $\epsilon \in \mathbb{R}$ is the strain and $T \in \mathbb{R}$ is temperature. λ_{B0} , ϵ_0 and T_0 are the initial values of the Bragg wavelength, strain and temperature, respectively.

In this study, the initial Bragg wavelength λ_{B0} is collected when the fiber is straight so that the fiber is strain-free and ϵ_0 can be assumed to be zero. In addition, an FBG sensor is placed in the central core of the fiber so that the strain on the sensor is zero when the fiber is bent and the term $\Sigma(T - T_0)$ can be acquired from it. The value of λ_B is measured and S is a known constant. Thus, the strain on an FBG sensor can be calculated.

The next section presents the details on acquiring the curvature vectors of the fiber given the arrangement of the FBG sensors within the fiber and their strain values.

3.2.2 Curvature Vector

The curve representing the fiber can be reconstructed if the curvature vectors are known for the complete length of the curve. In this study, the curvature vectors are acquired from sets of FBG sensors placed along the length of the multi-core fiber. Each set of FBG sensors contains four co-located FBGs, one in the center core and three in the outer cores as shown

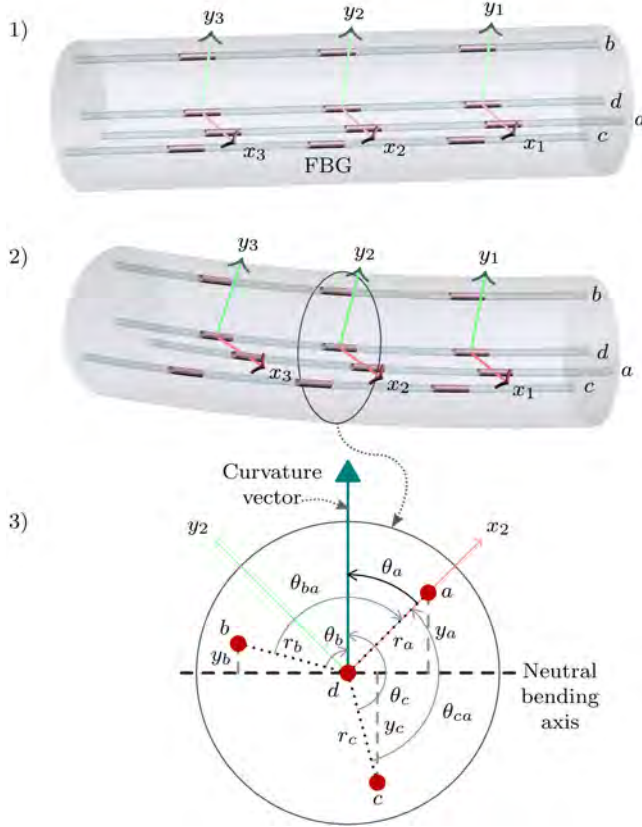


Figure 3.2: 1) A segment of the multi-core fiber in its initial configuration. The four cores of the fiber are labeled a , b , c and d . Three sets of fiber Bragg gratings (FBG) sensors and their local frames for curvature vector calculation are shown. 2) The segment of the multi-core fiber in a bent configuration. 3) The fiber cross section at the second set of FBG sensors when the fiber is bent. The variables required for the curvature vector calculation are illustrated; $y_i \in \mathbb{R}_{>0}$ (where $i \in a, b, c, d$) is the perpendicular distance from the FBG sensor on core i to the neutral bending axis; $r_i \in \mathbb{R}_{>0}$ is the radial distance from the center to core i ; $\theta_i \in (-\pi, \pi]$ is the angle from r_i to the curvature vector; θ_{ba} is the angle between r_b and r_a and θ_{ca} is the angle between r_c and r_a .

in Figure 3.2. An orthogonal frame is attached to each FBG set such that the x and y axis are on the fiber cross section and the x axis is from the center of the fiber to one of the outer core, see Figure 3.2. The curvature

vector for a set is calculated with respect to the allocated orthogonal frame by utilizing the relation between curvature and strain provided by the theory of bending mechanics [19]. The strain experienced by the FBG sensors on the outer cores is proportional to their perpendicular distance from the neutral bending axis. Adapting the sign convention for the strain to be positive for tension and negative for compression, the relation between strain and curvature is as follows:

$$\epsilon_i(s) = -\kappa(s)y_i(s) = -\kappa(s)r_i\cos(\theta_i(s)), \quad (3.2)$$

where, $s \in \mathbb{R}$ is the parameter for the arc length of the fiber and is defined in the interval $\Omega \subset \mathbb{R}$ such that $\Omega = (0, L)$; $L \in \mathbb{R}_{>0}$ is the length of the fiber. $\epsilon_i(s) \in \mathbb{R}_{>0}$ is the strain on the FBG in core $i \in \{a, b, c, d\}$; $\kappa(s) \in \mathbb{R}_{>0}$ is the magnitude of curvature; $y_i(s) \in \mathbb{R}$ is the perpendicular distance from the FBG in core i to the neutral axis; $r_i \in \mathbb{R}_{>0}$ is the radial distance from the center to core i ; and $\theta_i(s) \in (-\pi, \pi]$ is the angle from r_i to the curvature vector. These variables are illustrated in Figure 3.2.3.

The curvature value $\kappa(s)$ and the angle $\theta_a(s)$ are the magnitude and angle of the curvature vector for the set of FBG sensors at arc length s of the fiber. The location of the FBG sensor set on the fiber is known *a priori*; $\kappa(s)$ and $\theta_s(s)$ are acquired from the four FBG sensor measurements at a location s using the following method. Let $\xi_i(s) = \ln \frac{\lambda_{Bi}(s)}{\lambda_{B0i}(s)}$, where $\lambda_{Bi}(s)$ is the measured Bragg wavelength and $\lambda_{B0i}(s)$ is the Bragg wavelength when no strain is applied on the fiber so that $\epsilon_0 = 0$, then from (3.1)

$$\xi_i(s) = S\epsilon_i(s) + c_t(s), \quad (3.3)$$

where $c_t(s) = \Sigma(T_i(s) - T_{0i}(s))$ and is assumed to be the same in all the FBG sensors that are in one set due to their close proximity. The strain value ϵ_d from the FBG sensor in core d is set to be zero because it is on the neutral bending axis, thus $\xi_d(s) = c_t(s)$. Given these assumptions and substituting (3.2) into (3.3) the following set of equations hold:

$$\xi_a(s) - \xi_d(s) = -S\kappa(s)r_a\cos(\theta_a(s)), \quad (3.4)$$

$$\xi_b(s) - \xi_d(s) = -S\kappa(s)r_b\cos(\theta_a(s) + \theta_{ba}), \quad (3.5)$$

$$\xi_c(s) - \xi_d(s) = -S\kappa(s)r_c\cos(\theta_a(s) + \theta_{ca}), \quad (3.6)$$

where, θ_{ba} is the angle between r_b and r_a ; similarly, θ_{ca} is the angle between r_c and r_a . Applying trigonometric angle sum identities, Equations (3.4)-(3.6) can be represented as a matrix equation

$$\boldsymbol{\xi}(s) = \mathbf{C}\mathbf{v}(s), \quad (3.7)$$

where,

$$\boldsymbol{\xi}(s) = \begin{bmatrix} \xi_a(s) - \xi_d(s) \\ \xi_b(s) - \xi_d(s) \\ \xi_c(s) - \xi_d(s) \end{bmatrix}, \mathbf{C} = \begin{bmatrix} -Sr_a & 0 \\ -Sr_b \cos(\theta_{ba}) & Sr_b \sin(\theta_{ba}) \\ -Sr_c \cos(\theta_{ca}) & Sr_c \sin(\theta_{ca}) \end{bmatrix},$$

$$\mathbf{v}(s) = \begin{bmatrix} v_1(s) \\ v_2(s) \end{bmatrix} = \begin{bmatrix} \kappa(s) \cos(\theta_a(s)) \\ \kappa(s) \sin(\theta_a(s)) \end{bmatrix}.$$

The components of $\mathbf{v}(s)$ can be solved using the pseudo-inverse of \mathbf{C}

$$\mathbf{v}(s) = \mathbf{C}^\dagger \boldsymbol{\xi}(s), \quad (3.8)$$

then using the definition of $\mathbf{v}(s)$ from (3.7),

$$\kappa(s) = \sqrt{v_1^2(s) + v_2^2(s)}, \quad (3.9)$$

$$\theta_a(s) = \text{atan2}(v_2(s), v_1(s)). \quad (3.10)$$

The parameters $\kappa(s)$ and $\theta_a(s)$ give the curvature vector of the fiber for one set of FBG sensors at location s . This calculation can be repeated for all the FBG sensor sets on the fiber to get the curvature vectors which are required for the reconstruction as explained in the next subsection.

3.2.3 Reconstruction

The Bishop frame is used to reconstruct the curve that represents the fiber. It is selected over the more common Frenet-Serret frame because it has less restrictions on the curve than the Frenet-Serret frame [16]. More specifically, Bishop frame is valid for curves that are twice differentiable whereas Frenet-Serret frame require three times differentiability. This enables Bishop frames to be better suited for curves that have local linearity or discontinuity in curvature; as demonstrated in simulation by Shiyuan *et al.* [20]. Let $\boldsymbol{\gamma}(s) \in \mathbb{R}^3$ be the position vector of the curve. The frame at s consists of three orthonormal vectors $\mathbf{T}(s) \in \mathbb{R}^3$, $\mathbf{M}_1(s) \in \mathbb{R}^3$, and $\mathbf{M}_2(s) \in \mathbb{R}^3$. The derivatives of the position and the frame with respect to

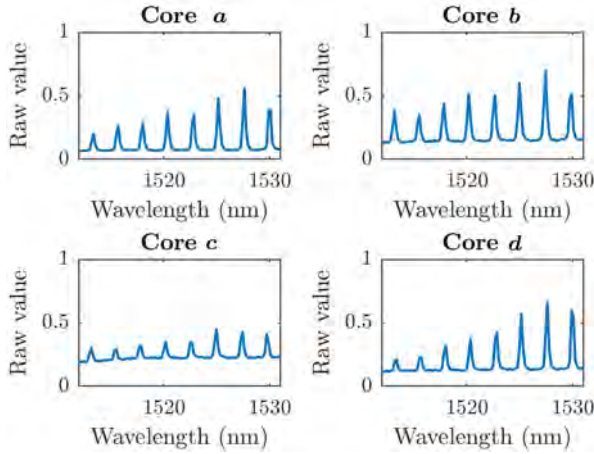


Figure 3.3: Spectra from the four cores labeled a , b , c , and d of a fiber as provided by the software of the interrogator FBG-scan 804D (FBGS International NV (Geel, Belgium)). The raw values in the y-axis of the plots are the output of the interrogator and they are the result of normalization by the saturation value of the interrogator's light sensors.

the arc length of the curve are as follows [16]:

$$\frac{d\gamma(s)}{ds} = \mathbf{T}(s), \quad (3.11)$$

$$\frac{d\mathbf{T}(s)}{ds} = k_1(s)\mathbf{M}_1(s) + k_2(s)\mathbf{M}_2(s), \quad (3.12)$$

$$\frac{d\mathbf{M}_1(s)}{ds} = -k_1(s)\mathbf{T}(s), \quad (3.13)$$

$$\frac{d\mathbf{M}_2(s)}{ds} = -k_2(s)\mathbf{T}(s). \quad (3.14)$$

In this study, the parameters $k_1(s) \in \mathbb{R}$ and $k_2(s) \in \mathbb{R}$ are calculated from the values of the curvature vector $\kappa(s)$ and $\theta_a(s)$ using the following relation:

$$k_1(s) = v_1(s) = \kappa(s)\cos(\theta_a(s)), \quad (3.15)$$

$$k_2(s) = v_2(s) = \kappa(s)\sin(\theta_a(s)). \quad (3.16)$$

This gives values of $k_1(s)$ and $k_2(s)$ at the locations of the FBG sensor sets. The values of $k_1(s)$ and $k_2(s)$ in between the FBG sensor set locations are estimated using linear interpolation. The interpolated values are denoted

as $\tilde{k}_1(s)$ and $\tilde{k}_2(s)$. The position $\boldsymbol{\gamma}(s)$ and the frame $\{\mathbf{M}_1(s), \mathbf{M}_2(s), \mathbf{T}(s)\}$ are solved using the following matrix form of (3.11)-(3.14):

$$\frac{d}{ds}\mathbf{X}(s) = \mathbf{X}(s)\mathbf{A}(s), \quad (3.17)$$

where,

$$\mathbf{X}(s) = \begin{bmatrix} \mathbf{T}(s) & \mathbf{M}_1(s) & \mathbf{M}_2(s) & \boldsymbol{\gamma}(s) \\ 0 & 0 & 0 & 1 \end{bmatrix}, \quad (3.18)$$

$$\mathbf{A}(s) = \begin{bmatrix} 0 & -\tilde{k}_1(s) & -\tilde{k}_2(s) & 1 \\ \tilde{k}_1(s) & 0 & 0 & 0 \\ \tilde{k}_2(s) & 0 & 0 & 0 \\ 0 & 0 & 0 & 0 \end{bmatrix}. \quad (3.19)$$

The discretized solution to (3.17) assuming $\mathbf{A}(s)$ is held constant between two consecutive values of $\tilde{k}_1(s)$, and $\tilde{k}_2(s)$ is given as:

$$\mathbf{X}(s + \Delta s) = \mathbf{X}(s) \exp(\mathbf{A}(s)\Delta s). \quad (3.20)$$

The tip pose is given by $\mathbf{X}(L)$, where L is the length of the fiber. The initial position is assumed to be $\boldsymbol{\gamma}(0) = [0\ 0\ 0]^T$ and the orientation to be $\mathbf{M}_1(0) = [1\ 0\ 0]^T$, $\mathbf{M}_2(0) = [0\ 1\ 0]^T$, $\mathbf{T}(0) = [0\ 0\ 1]^T$.

The reconstruction technique presented in Section 3.2 is empirically validated in the next Section.

3.3 Experiments

Three different experiments are conducted to validate the reconstructed pose using the technique presented in Section 3.2. Particularly, the tip pose is used for validation since the reconstruction error is the largest there due to the accumulation of error over the length in (3.20). The difference in tip pose between the reconstruction and the ground truth is calculated using three measures; one measure is the magnitude of the error in position $r_e \in \mathbb{R}$, the second is the angle between the orientation vector $\phi_e \in \mathbb{R}$, and the last measure is the difference in the rotation angles about the orientation vector $\theta_e \in \mathbb{R}$. The error measures are calculated as follows:

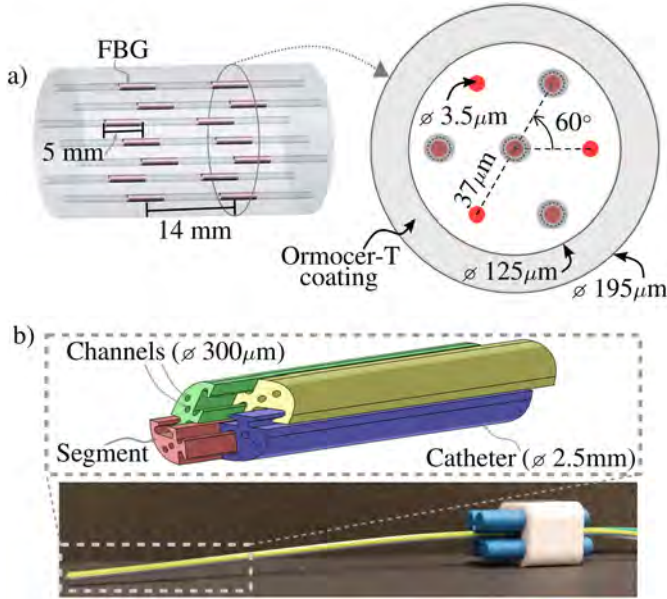


Figure 3.4: a) Cross-section and side view of the fibers utilized for the experiments. Each fiber has seven cores with eight groups of fiber Bragg grating (FBG) sensors. Two groups of sensors and the fiber cross-section are shown. A set of sensors used for the curvature vector calculations consists of four out of the seven sensors, as highlighted on the cross-section with gray discs. b) Photograph of the four-segment catheter used in the experiments along with an inset that shows the tip. Each segment can move independently in the axial direction and has two channels that are utilized for an electromagnetic (EM) sensor and a fiber.

$$r_e(k) = \|\mathbf{r}(k) - \mathbf{r}_{gt}(k)\| \quad (3.21)$$

$$\phi_e(k) = \cos^{-1} \left(\frac{\mathbf{v}_{gt}(k) \cdot \mathbf{v}(k)}{\|\mathbf{v}_{gt}(k)\| \|\mathbf{v}(k)\|} \right) \quad (3.22)$$

$$\theta_e(k) = \|\theta(k) - \theta_{gt}(k)\| \quad (3.23)$$

where, $k \in \mathbb{Z}_{\geq 0}$ represents the sample of the data; $\mathbf{r}(k) \in \mathbb{R}^3$ is the reconstructed tip position; $\mathbf{r}_{gt}(k) \in \mathbb{R}^3$ is the ground truth of the tip position; $\mathbf{v}(k) \in \mathbb{R}^3$ is the reconstructed tip orientation vector, $\mathbf{v}_{gt}(k) \in \mathbb{R}^3$ is the true orientation vector, $\theta(k) \in \mathbb{R}$ is the angle of rotation about the reconstructed orientation vector and $\theta_{gt}(k) \in \mathbb{R}$ is the angle of rotation about the true orientation vector. Details on the hardware and software for the experiments are given in Section 3.3.1. Descriptions of the three experiments

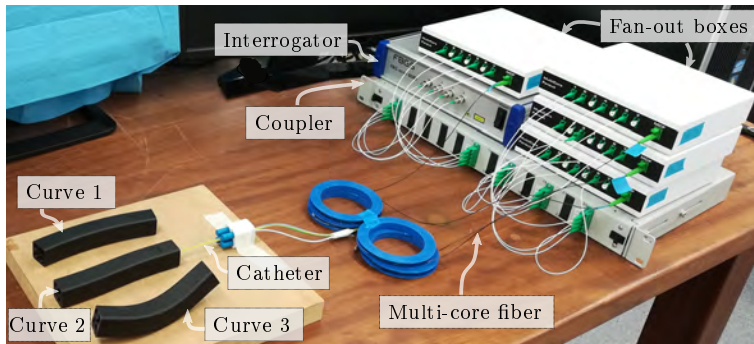


Figure 3.5: Setup for Experiment 1. The catheter is sensorized with four multi-core fibers that have fiber Bragg gratings (FBG); each catheter segment has one fiber. The experiment utilizes four multi-core fibers, fan-out boxes, interrogator, coupler, catheter, and three molds.

and the results are given in Sections 3.3.2, 3.3.3 and 3.3.4. Registration between the reference frame of the fibers and the reference frame of the ground truth is conducted for each experiment. A set of points in each frame is collected and the transformation between the frames is solved using least square estimation [21].

3.3.1 Setup

The hardware for the three experiments consists of a four-segment catheter, four multi-core fibers with eight sets of FBG sensors, an interrogator, four fan out boxes and a coupler. In addition, Experiment 1 includes 3D printed molds; Experiment 2 and 3 uses four EM sensors placed at the tip of the four segments; lastly, Experiment 3 utilizes a gelatin phantom and an actuation unit. The setup for Experiments 1, 2 and 3 are shown in Figures 3.5, 3.7 and 3.9, respectively.

Table 3.1: The curvature and torsion along the arc length of the centerline in the molds used for Experiment 1.

Configuration	Curvature (mm^{-1})	Torsion (mm^{-1})
Curve 1: Single bend	constant: $3.3e^{-3}$	constant: 0
Curve 2: Double bend	linear: $2.5e^{-3}$ to $-2.5e^{-3}$	constant: 0
Curve 3: Space curve	constant: $1.0e^{-2}$	constant: $2.2e^{-2}$

The FBG sensors are written using the Draw Tower Grating technique on all the cores at eight locations on each of the four fibers [22]. The spectra from a strain-free fiber are shown in Figure 3.3. The nominal Bragg wavelength differ between consecutive FBG sensors by 2.4 nm and the wavelength range on the four fibers are 1513–1529.8 nm, 1532.2–1549 nm, 1551.4–1568.2 nm, and 1570.6–1587.4 nm. As shown in Figure 3.4a, every sensor is 5 mm long and the sensor sets are 14 mm apart which means the sensorized section of each fiber is 103 mm. The core and the cladding of the fiber are composed of fused silica and their refractive indices are 1.454 and 1.444, respectively. The operating temperature range of the fiber is -20°C to 200°C [23]. FBGS International NV (Geel, Belgium) supplied the fibers with FBG sensors, the value of the gauge factor $S = 0.777$ in (1), the interrogator (FBG-scan 804D), four fan out boxes and a coupler [24].

The catheter is 2.5 mm in diameter and manufactured with medical-grade polymer by Xograph Healthcare Ltd. (Gloucestershire, United Kingdom). It is illustrated in Figure 3.4b. Further information on the catheter manufacturing procedure and material properties are given in Watts *et al.* [25]. The shape of the catheter can be controlled with the relative difference in the insertion length of the segments. The insertion of each catheter segment is controlled and executed by the actuation box that is described in Watts *et al.* [25].

The EM sensor is part of the Aurora System from NDI Medical (Ontario, Canada), it is 0.3 mm in diameter and has five degrees of freedom which include position in three dimensions, pitch and yaw. The root mean square error of the EM sensors is 0.70 mm and 0.20° in position and orientation, respectively [26].

The gelatin phantom is produced to mimic soft brain tissue from 4.5% by weight bovine gelatin [27]. The 3D printed molds and the actuation unit are designed and built in-house. The software used in the experiments is also developed in-house for Ubuntu 16.04.

3.3.2 Experiment 1: Static tests

A four-segment catheter with four fibers is placed in 3D printed molds and the reconstructed catheter tip pose is compared to the tip pose of the mold's centerline. Table 3.1 describes the curves that form the centerline of the three molds. Each fiber is reconstructed using (3.20) and the catheter's centerline is calculated as the mean of the reconstructed position and orientation of the fibers at particular arc lengths. Data from Curve 1 are used to solve for the transformation between the reconstruction frame and the

ground truth frame.

The reconstruction of the catheter centerline is validated by the error in the tip pose. The error measures of (3.21), (3.22) and (3.23) are used where $\mathbf{v}(k)$ is the axis and $\theta(k)$ is the angle from the axis-angle representation of the tip orientation frame $\{\mathbf{M}_1(L), \mathbf{M}_2(L), \mathbf{T}(L)\}$ and $\mathbf{r}(k)$ is $\gamma(L)$ at sample k . Similarly, the ground truth values $\mathbf{r}_{gt}(k)$, $\theta_{gt}(k)$ and $\mathbf{v}_{gt}(k)$ are

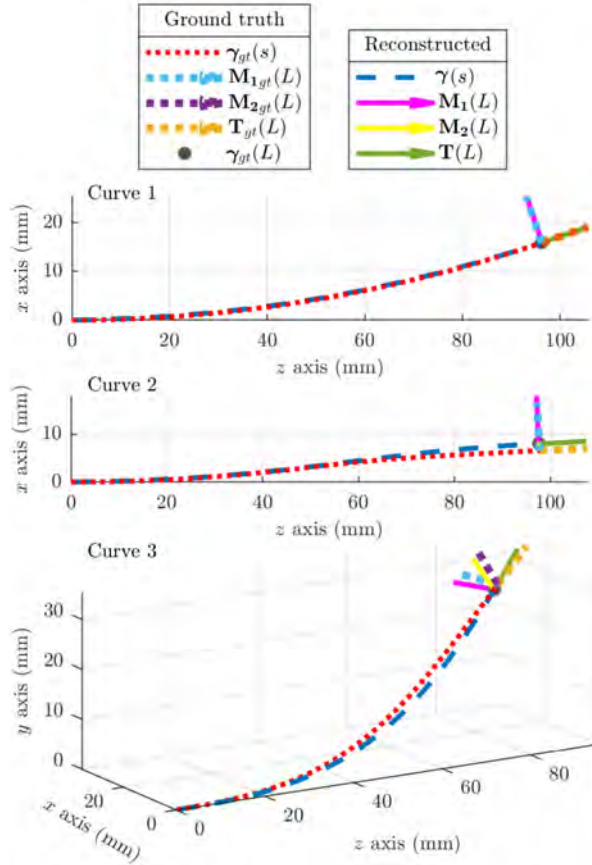


Figure 3.6: The ground truth and the reconstruction plots of the three curves from one sample in Experiment 1. In the legend, $\gamma(s) \in \mathbb{R}^3$, is the reconstructed curve, where $s \in \mathbb{R}$ is the arc length parameter. $\mathbf{M}_1(L) \in \mathbb{R}^3$, $\mathbf{M}_2(L) \in \mathbb{R}^3$ and $\mathbf{T}(L) \in \mathbb{R}^3$ represent the orientation at the curve's tip. Similarly, $\gamma_{gt}(s) \in \mathbb{R}^3$, $\mathbf{M}_{1_{gt}}(L) \in \mathbb{R}^3$, $\mathbf{M}_{2_{gt}}(L) \in \mathbb{R}^3$, $\mathbf{T}_{gt}(L) \in \mathbb{R}^3$ are the analogous values from the ground truth. Lastly, $\gamma_{gt}(L) \in \mathbb{R}^3$ is the ground truth curve's tip position.

Table 3.2: Mean ($\bar{r}_e, \bar{\phi}_e, \bar{\theta}_e$) and standard deviation ($\sigma_{r_e}, \sigma_{\phi_e}, \sigma_{\theta_e}$) of the error in catheter tip pose from (3.21), (3.22) and (3.23) over the samples collected for each curve in Experiment 1.

	Curve 1	Curve 2	Curve 3
\bar{r}_e (σ_{r_e}) (mm)	0.09 (0.03)	1.45 (0.06)	1.73 (0.05)
$\bar{\phi}_e$ (σ_{ϕ_e}) (degree)	1.01 (0.09)	0.66 (0.04)	0.37 (0.03)
$\bar{\theta}_e$ (σ_{θ_e}) (degree)	0.34 (0.06)	0.32 (0.05)	1.94 (0.06)

acquired from the mold’s centerline curve. For this experiment the ground truth values are constant for all samples. The mean of the error measures and the standard deviation given in Table 3.2 are over all samples. The reconstruction and the ground truth from a sample of the three curves are shown in Figure 3.6.

3.3.3 Experiment 2: Dynamic tests conducted in air

In this experiment, the catheter is moved in air by manually pushing on it from different directions. The objective is to validate the reconstruction by comparing the reconstructed fiber tip pose to an EM sensor pose. Each of the catheter’s four segments is sensorized with a fiber and an EM sensor, which is placed at the segment’s tip. The four fibers’ tip pose from the reconstruction and the four EM sensors’ pose are collected over time.

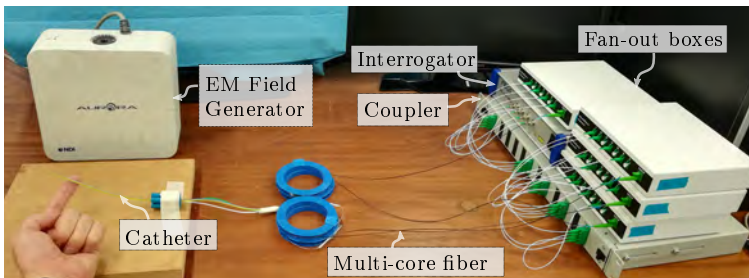


Figure 3.7: Setup for Experiment 2. The catheter is sensorized with fiber Bragg gratings (FBG) inscribed multi-core fibers and electromagnetic (EM) sensors. The hardware utilized consists of four multi-core fibers, fan-out boxes, interrogator, coupler, four-segment catheter, four electromagnetic (EM) sensors and EM field generator.

The catheter is manually moved for three trials and an additional trial is conducted in order to solve for the transformation between the EM sensor frame and the reconstruction frame. The tip pose of each fiber is reconstructed using (3.20) and it is compared to the pose of the EM sensor in the same segment as the fiber. The error is calculated using (3.21) and (3.22) where, $\mathbf{r}(k)$ is $\gamma(L)$ and $\mathbf{v}(k)$ is $\mathbf{T}(L)$ at sample k . The value for $\mathbf{r}_{gt}(k)$ and $\mathbf{v}_{gt}(k)$ are acquired from the EM sensor measurements. Since the EM sensors have 5 degrees of freedom, the rotation about the orientation axis is not available. Table 3.3 gives the mean and standard deviation of the error measures among all the segments over the duration of every trial. The trajectory of a fiber tip and of the corresponding EM sensor during the first trial is given in Figure 3.8.

3.3.4 Experiment 3: Dynamic tests conducted in gelatin

The catheter is inserted into a gelatin phantom that mimics soft brain tissue [25]. The aim is to validate the reconstruction when distributed force is applied along the catheter from the environment. The catheter is sensorized as in Experiment 2. Three insertions into the phantom are

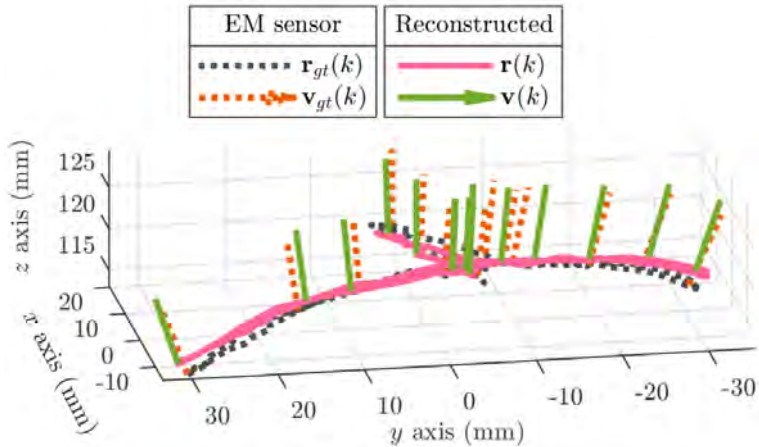


Figure 3.8: The trajectory traced by an electromagnetic (EM) sensor and the corresponding fiber tip placed in the catheter during Trial 1. The orientation vectors at selected samples are also shown on the trajectory. $k \in \mathbb{R}$ represents a sample in time, $\mathbf{r}(k) \in \mathbb{R}^3$ is the fiber tip position, $\mathbf{v}(k) \in \mathbb{R}^3$ is the fiber tip orientation vector. $\mathbf{r}_{gt}(k) \in \mathbb{R}^3$ and $\mathbf{v}_{gt}(k) \in \mathbb{R}^3$ are the position and orientation from the EM sensor, respectively.

Table 3.3: Mean ($\bar{r}_e, \bar{\phi}_e$) and standard deviation ($\sigma_{r_e}, \sigma_{\phi_e}$) of the fiber tip pose error according to (3.21) and (3.22) over the samples collected from all four fibers during Experiment 2.

	Trial 1	Trial 2	Trial 3
\bar{r}_e (σ_{r_e}) (mm)	2.20 (1.28)	2.95 (1.88)	2.89 (1.42)
$\bar{\phi}_e$ (σ_{ϕ_e}) (degree)	3.50 (1.38)	3.52 (1.10)	3.37 (1.27)

conducted; in the first insertion the catheter follows a straight path, in the second the catheter follows a single bend path and finally in the third, the catheter follows a double bend path. Each insertion is controlled by an actuation unit as described in Watts *et al.* so that the catheter follows the pre-determined path [25]. For each insertion, data from the FBG sensors in the fibers and the EM sensors are collected simultaneously.

The fiber tip is reconstructed using (3.20). The error between the reconstructed fiber tip pose and the EM sensor on the same catheter segment is calculated using (3.21) and (3.22) where the variables have the same assignment as in Experiment 2. The EM frame and the reconstruction frame are registered using data from a trial that constituted of manually moving the catheter in air. Figure 3.10 shows the plot of a catheter segment's tip trajectory during the second insertion which consisted of a single bend path. The mean and standard deviation of the error measures for the three insertions are given in Table 3.4.

3.4 Discussion

In the static experiments, the difference in error between this study and Khan *et al.* is possibly due to the different FBG inscription method utilized

Table 3.4: Mean ($\bar{r}_e, \bar{\phi}_e$) and standard deviation ($\sigma_{r_e}, \sigma_{\phi_e}$) of the fiber tip pose error according to (3.21) and (3.22) for the three insertions in Experiment 3. The mean and standard deviation is over all the tip pose collected from the four fibers and EM sensors during each insertion.

	Insertion 1	Insertion 2	Insertion 3
\bar{r}_e (σ_{r_e}) (mm)	1.54 (1.34)	4.35 (2.17)	4.69 (2.81)
$\bar{\phi}_e$ (σ_{ϕ_e}) (degree)	2.85 (2.11)	6.48 (3.18)	3.49 (2.51)

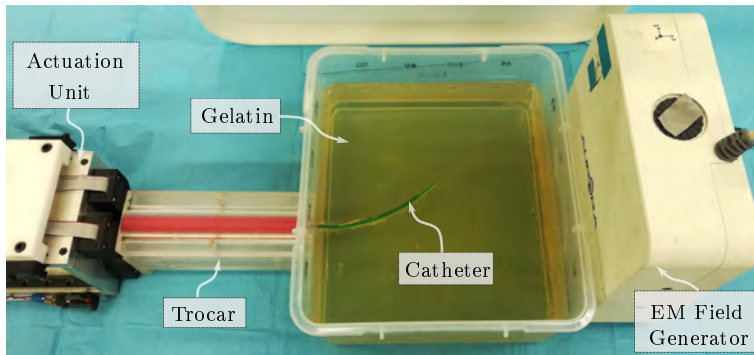


Figure 3.9: Setup for Experiment 3. The catheter followed a single bend path. It is sensorized with multi-core fibers that have fiber Bragg gratings (FBG) and electromagnetic (EM) sensors. The experiment utilizes hardware from Experiment 2 and in addition requires an actuation unit, trocar to hold the catheter and gelatin phantom.

for the sensors. In this study Draw Tower Grating (DTG) technique is used whereas Khan *et al.* used a Phase Mask (PM) technique [13]. The DTG technique produced sensors with reflectivity of 3% of the input light whereas the PM technique produced sensors with reflectivity of at least 30%. The higher reflectivity of the sensors inscribed with PM technique could lead to more accurate detection of the Bragg wavelength, which would result in a lower reconstruction error. However, for the PM technique the fiber coating is removed before inscription, which made the fiber very fragile and unsuitable for dynamic experiments with gelatine or soft tissue. In the DTG technique the sensors are inscribed just after the fiber is drawn and before the coating is applied [28]. Since the original coating of the fiber remained intact the resulting fiber had high breakage strength, which is necessary for dynamic experiments. For this reason, sensors inscribed with DTG technique are utilized in this study.

In the dynamic experiments, the error may be caused by the fiber's motion relative to the catheter. The fibers are attached to the segments at a single point near the catheter base, so that they can be detached and reused. Thus, the fibers are free within the channel and can move relative to the catheter. The error due to fiber motion may be reduced by incorporating a mechanics model of the catheter in the pose measurement.

3.5 Conclusions and Future Work

A technique for acquiring the pose of a flexible instrument from FBG measurements is presented in the chapter. The measurements from the FBG sensors are first converted to strain and then the curvature vectors are calculated at the locations on the fiber with co-located FBG sensors. The curvature calculation uses the strain values from the sensors and the theory of bending mechanics. Once the curvature is calculated, the fiber is reconstructed using Bishop Frames. The reconstruction provides the pose of the fiber along its arc length and the tip pose is validated in two dynamics experiments. The reconstruction of four fibers is utilized to deduce an instrument's tip pose which is validated in static experiments. The results from all the experiments show that the mean error in position is less than 4.69 mm and mean error in orientation is less than 6.48 degrees. Thus, acquiring the pose of a flexible instrument is feasible with FBG sensors in multi-core fiber. In future work, temperature sensing and temperature compensation using FBG sensors in multi-core fiber will be studied.

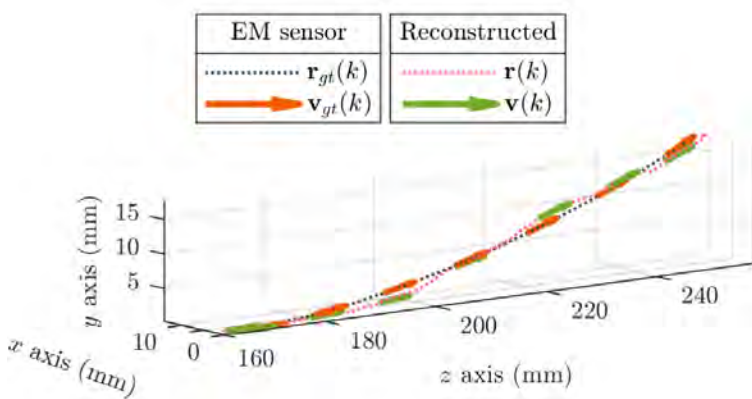


Figure 3.10: The trajectory during insertion 2 of the electromagnetic (EM) sensor and the fiber tip from one of the catheter's segments. $k \in \mathbb{R}$ represents a sample in time, $\mathbf{r}(k) \in \mathbb{R}^3$ is the fiber tip position, and $\mathbf{v}(k) \in \mathbb{R}^3$ is the fiber tip orientation vector. $\mathbf{r}_{gt}(k) \in \mathbb{R}^3$ and $\mathbf{v}_{gt}(k) \in \mathbb{R}^3$ are the position and orientation from the EM sensors, respectively.

Acknowledgments

The authors would like to thank Dr. Riccardo Secoli and Ms. Eloise Matheson for their help with Experiment 3. In addition, the authors appreciate the valuable feedback on the manuscript from Dr. Venkat Kalpathy Venkiteswaran and Mr. Jakub Sikorski.

References

- [1] D. Tosi, E. Schena, C. Molardi, and S. Korganbayev, "Fiber optic sensors for sub-centimeter spatially resolved measurements: Review and biomedical applications," *Optical Fiber Technology*, vol. 43, pp. 6 – 19, 2018.
- [2] C. Shi, X. Luo, P. Qi, T. Li, S. Song, Z. Najdovski, T. Fukuda, and H. Ren, "Shape sensing techniques for continuum robots in minimally invasive surgery: A survey," *IEEE Transactions on Biomedical Engineering*, vol. 64, no. 8, pp. 1665–1678, 2017.
- [3] R. Reilink, S. Stramigioli, and S. Misra, "Pose reconstruction of flexible instruments from endoscopic images using markers," in *2012 IEEE International Conference on Robotics and Automation*, May 2012, pp. 2938–2943.
- [4] P. Cabras, F. Nageotte, P. Zanne, and C. Doignon, "An adaptive and fully automatic method for estimating the 3D position of bendable instruments using endoscopic images," *The International Journal of Medical Robotics + Computer Assisted Surgery : MRCAS*, vol. 13, no. 7, pp. 1–14, 2017.
- [5] A. M. Franz, T. Haidegger, W. Birkfellner, K. Cleary, T. Peters, and L. Maier-Hein, "Electromagnetic tracking in medicine-a review of technology, validation, and applications," *IEEE Transactions on Medical Imaging*, vol. 33, no. 8, pp. 1702–1725, 2014.
- [6] F. Taffoni, D. Formica, P. Saccomandi, G. Di Pino, and E. Schena, "Optical fiber-based MR-compatible sensors for medical applications: An overview," *Sensors*, vol. 13, no. 10, pp. 14 105–14 120, 2013.
- [7] B. Lee, "Review of the present status of optical fiber sensors. optical fiber technology 9, 57-79," *Optical Fiber Technology*, vol. 9, no. 2, pp. 57–79, 2003.

- [8] S. Sareh, Y. Noh, M. Li, T. Ranzani, H. Liu, and K. Althoefer, “Macrobend optical sensing for pose measurement in soft robot arms,” *Smart Materials and Structures*, vol. 24, pp. 1–14, 2015.
- [9] J. P. Moore and M. D. Rogge, “Shape sensing using multi-core fiber optic cable and parametric curve solutions,” *Opt. Express*, vol. 20, no. 3, pp. 2967–2973, 2012.
- [10] Y. Xinhua, W. Mingjun, and C. Xiaomin, “Deformation sensing of colonoscope on FBG sensor net,” *TELKOMNIKA : Indonesian Journal of Electrical Engineering*, vol. 10, no. 8, pp. 2253–2260, 2012.
- [11] Y. Park, S. Elayaperumal, B. Daniel, S. C. Ryu, M. Shin, J. Savall, R. J. Black, B. Moslehi, and M. R. Cutkosky, “Real-time estimation of 3-D needle shape and deflection for MRI-guided interventions,” *IEEE/ASME Transactions on Mechatronics*, vol. 15, no. 6, pp. 906–915, 2010.
- [12] R. J. Roesthuis, M. Kemp, J. J. van den Dobbelsteen, and S. Misra, “Three-dimensional needle shape reconstruction using an array of fiber bragg grating sensors,” *IEEE/ASME Transactions on Mechatronics*, vol. 19, no. 4, pp. 1115–1126, 2014.
- [13] **F. Khan**, A. Denasi, D. Barrera, J. Madrigal, S. Sales, and S. Misra, “Multi-core optical fibers with bragg gratings as shape sensor for flexible medical instruments,” *IEEE Sensors Journal*, vol. 19, no. 14, pp. 5878–5884, 2019.
- [14] K. Henken, D. van Gerwen, J. Dankelman, and J. Dobbelsteen, “Accuracy of needle position measurements using fiber bragg gratings,” *Minimally Invasive Therapy & Allied Technologies*, vol. 21, no. 6, pp. 408–414, 2012.
- [15] A. Gray, *Modern Differential Geometry of Curves and Surfaces with Mathematica*. Boca Raton, Florida, United States of America: Chapman & Hall/CRC, 2006.
- [16] R. L. Bishop, “There is more than one way to frame a curve,” *The American Mathematical Monthly*, vol. 82, no. 3, pp. 246–251, 1975.
- [17] K. O. Hill and G. Meltz, “Fiber Bragg grating technology fundamentals and overview,” *Journal of Lightwave Technology*, vol. 15, no. 8, pp. 1263–1276, 1997.

-
- [18] J. Van Roosbroeck, C. Chojetzki, J. Vlekken, E. Voet, and M. Voet, "A new methodology for fiber optic strain gage measurements and its characterization," in *Proceedings of the SENSOR+TEST Conferences*, vol. OPTO 2 - Optical Fiber Sensors, pp. 59 - 64, Nürnberg, Germany, May 2009.
- [19] R. C. Hibbeler, *Mechanics of materials*, 8th ed. Upper Saddle River, New Jersey, United States: Pearson Prentice Hall, 2011.
- [20] Z. Shiyuan, J. Cui, C. Yang, and J. Tan, "Parallel transport frame for fiber shape sensing," *IEEE Photonics Journal*, vol. 10, no. 1, pp. 1–13, 2018.
- [21] S. Umeyama, "Least-squares estimation of transformation parameters between two point patterns," *IEEE Transactions on Pattern Analysis and Machine Intelligence*, vol. 13, no. 4, pp. 376–380, 1991.
- [22] B. Van Hoe, J. Van Roosbroeck, C. Voigtländer, J. Vlekken, and E. Lindner, "Distributed strain and curvature measurements based on tailored draw tower gratings," in *IEEE Avionics and Vehicle Fiber-Optics and Photonics Conference (AVFOP)*, pp. 285-286, California, USA, Oct 2016.
- [23] FBGS International NV, "Draw Tower Gratings (DTG)," Jan 2019. [Online]. Available: <https://fbgs.com/components/draw-tower-gratings-dtgs/> [Accessed: January 7, 2020].
- [24] *Manual 'ILLumiSense' software*, Version 2.3, FBGS International, Bell Telephonelaan 2H, Geel Belgium, 2014.
- [25] T. Watts, R. Secoli, and F. Rodriguez y Baena, "A mechanics-based model for 3-D steering of programmable bevel-tip needles," *IEEE Transactions on Robotics*, vol. 35, no. 2, pp. 371–386, 2019.
- [26] NDI Medical, "Aurora-Medical," Sept 2013. [Online]. <https://www.ndigital.com/medical/products/aurora/> [Accessed: January 7, 2020].
- [27] A. Leibinger, A. E. Forte, Z. Tan, M. J. Oldfield, F. Beyrau, D. Dini, and F. Rodriguez y Baena, "Soft tissue phantoms for realistic needle insertion: A comparative study," *Annals of Biomedical Engineering*, vol. 44, no. 8, pp. 2442–2452, 2016.

- [28] FBGS International NV, “DTG & FSG Technology,” Jan 2019. [Online]. Available: <https://fbgs.com/technology/dtg-fsg-technology/> [Accessed: January 7, 2020].

Chapter 4

Straight and Helical Core Fibers

Abstract

This paper presents a technique to acquire measurements of curvature, twist and pose for two multi-core fibers; one with straight cores and the other with helical cores. Both the fibers have multiple fiber Bragg grating (FBG) sensors inscribed in the cores and the fibers are placed in known configurations in order to compare their measurement accuracy. For the curvature measurements both the fibers are placed in constant curvature slots; for the twist measurements, a set of twists are applied to each fiber and for the pose measurements the fibers are placed in moulds of different shape. The mean curvature errors are 0.22 m^{-1} and 0.13 m^{-1} , in the helical and straight core fiber respectively. For the twist measurement the mean errors are 26.57 degrees/m and 146.50 degrees/m in the helical and straight core fiber, respectively. Lastly, the pose measurement consists of position and orientation where the orientation is represented in the axis-angle form. The mean position errors are 0.49 mm and 0.27 mm, the mean axis orientation errors are 0.12 degrees and 0.26 degrees and the mean angle orientation errors are 1.10 degrees and 1.18 degrees, for the helical and straight core fiber, respectively. The results show that the twist measurement error is significantly low with the helical core fiber, thus helical core fiber is better suited than straight core fiber for applications where twist measurements are required.

4.1 Introduction

Fiber Bragg gratings (FBG) have been applied in various fields such as oil and gas industry, security, structural health monitoring and have promising applications for monitoring medical instruments [1] [2]. This is due to their compactness, light weight, flexibility, tensile strength, immunity to electromagnetic interference and high tolerance to temperature [3]. This study focuses on application of the FBG sensors for curvature, twist and pose measurements of minimally invasive medical instruments. Spatial information of minimally invasive instruments during medical procedures is essential for accurate navigation. The instrument's tip pose, which is the position and orientation, is particularly important for avoiding critical structures inside the body. Currently, this information is commonly acquired using fluoroscopy or ultrasound. However, the instruments can be difficult to observe in ultrasound due to artifacts and low resolution, while fluoroscopy exposes patients to harmful radiation. These issues are mitigated with the use of FBG sensors because they are safe and can provide good resolution data in space and time; thus these sensors are an attractive alternative [4].

In the literature, several studies have validated the use of FBG sensors inscribed in optical fibers for position measurements and its application in medical procedures [1, 5–8]. Nevertheless, Duncan *et. al* have observed error in position measurement from FBG sensors in straight core fiber due to their insufficient sensitivity to twist [9]. In order to acquire more accurate twist measurement researchers have inscribed FBG sensors on helical core fibers and validated its accuracy as twist sensors [3, 4, 7, 10–12]. However, a comparison in measurement accuracy between FBG sensors in helical core fiber and in straight core fiber has not been presented [13]. In this study, the measurement accuracy of curvature, twist and pose are presented for both helical and straight core fiber. Each fiber has multiple sets of co-located FBG sensors as shown in Figure 4.1. The results show that the helical core fiber is better suited than the straight core fiber for applications with twist. The main contributions of this study are the application of an elastic rod model to the helical core fiber in order to acquire the pose of the tip and the comparative study of the measurement accuracy between the helical and straight core fiber. The theoretical background utilized to acquire the results, and description of the experiments are presented in Sections 4.2 and 4.3, respectively.

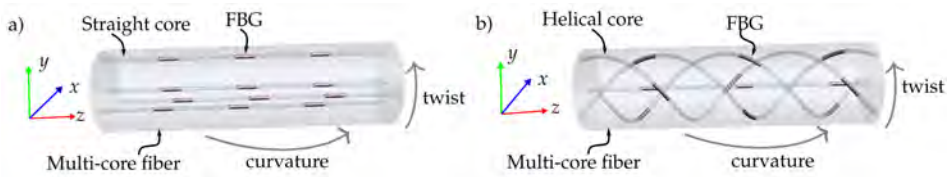


Figure 4.1: a) Straight core fiber with three sets of co-located fiber Bragg grating (FBG) sensors. b) Helical core fiber with three sets of co-located FBG sensors. Curvature is induced due to a torque about a vector in the x - y plane and twist is due to torque about the z -axis.

4.2 Theoretical Background

The technique to acquire the curvature, twist and pose measurements using FBG sensors in the multi-core fibers with helical and straight cores is presented in this section. It is based on mechanics of materials and the elastic rod theory [14, 15]. The curvature and twist is determined from the strain on the fiber. According to the mechanics of materials, the fiber's curvature is related to its normal strain and its twist to its shear strain by the following equations [15]:

$$\epsilon_{\kappa} = -\kappa y, \quad (4.1)$$

$$\epsilon_{\tau} = G \frac{\Delta\phi}{\Delta z} r, \quad (4.2)$$

where, $\epsilon_{\kappa} \in \mathbb{R}$ is the strain due to curvature, $\kappa \in \mathbb{R}_{\geq 0}$ is the curvature value, $y \in \mathbb{R}_{\geq 0}$ is the perpendicular distance between the neutral axis and the location of the strain on the cross section. The strain due to the twist is $\epsilon_{\tau} \in \mathbb{R}$ at a radial distance $r \in \mathbb{R}_{> 0}$ and $G \in \mathbb{R}_{> 0}$ is the material constant relating shear strain with angular difference. The applied twist will cause the cross sections along the arc length of the fiber to rotate with respect to each other. The angular change between two cross sections is given by $\Delta\phi \in \mathbb{R}$ and the difference in arc length between those cross sections is $\Delta z \in \mathbb{R}_{> 0}$. $\Delta z = z_2 - z_1$ in Figure 4.2, which illustrates the variables in (4.1)-(4.2) on the multi-core fiber cross-section.

The strains on the fiber can be calculated from the measured Bragg wavelength of the FBG sensors. In this study, the sensors are placed along the fiber such that there are sets of four co-located sensors, which means there are four sensors at particular cross sections of the fiber. These sensors enable measurements of strains at four locations on the cross section, as

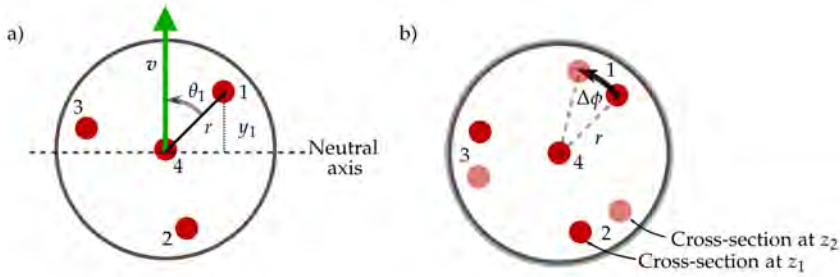


Figure 4.2: Cross-section of the straight core fiber and the helical core fiber with numerical labels $\{1, 2, 3, 4\}$ for the cores. a) Parameters for curvature measurement. $\mathbf{v} \in \mathbb{R}^2$ is the curvature vector, $\|\mathbf{v}\| = \kappa \in \mathbb{R}$, $\theta_1 \in \mathbb{R}$ is the angle between core 1 and the curvature vector, $r \in \mathbb{R}$ is the radial distance to the cores, $y_1 \in \mathbb{R}$ is the perpendicular distance from core 1 to the neutral axis. b) Parameters for twist measurement. Overlay of two cross sections of the fiber, one at arc length $z_1 \in \mathbb{R}_{>0}$ and the other at $z_2 \in \mathbb{R}_{>0}$, $\Delta z = z_2 - z_1$. An applied twist will cause the cross sections to be rotated with respect to each other, this rotation is $\Delta\phi \in \mathbb{R}$.

shown in Figure 4.2. These strain measurements can be used to solve for the curvature and twist. The relation between strain and the Bragg wavelength of an FBG sensor can be approximated with the following linear equation [16]:

$$\frac{\Delta\lambda_{B0}}{\lambda_{B0}} = S(\epsilon - \epsilon_0), \quad (4.3)$$

where, $\lambda_{B0} \in \mathbb{R}$ and $\epsilon_0 \in \mathbb{R}$ are the initial values of the Bragg wavelength and strain, respectively. $S \in \mathbb{R}_{>0}$ is the gauge factor and $\epsilon \in \mathbb{R}$ is the strain. However, a general relation that also incorporates the temperature is the following [17]:

$$\ln \frac{\lambda_B}{\lambda_{B0}} = S(\epsilon - \epsilon_0) + \Sigma(T - T_0), \quad (4.4)$$

where, $\lambda_B \in \mathbb{R}$ is the measured Bragg wavelength, $\Sigma \in \mathbb{R}_{>0}$ is the temperature sensitivity, $T \in \mathbb{R}$ is temperature, and $T_0 \in \mathbb{R}$ is the initial temperature.

The strain on the external cores, shown as cores 1-3 in Figure 4.2, is due to both curvature and twist; whereas the strain on the central core, labeled 4, is theoretically zero since it is at the center of the cross section. Any change in Bragg wavelength of sensor 4 is due to change in temperature, thus it can be used to eliminate the effect of temperature in cores 1-3. The

strain due to twist is the same on the sensors 1-3 and since they are $\frac{2\pi}{3}$ radians apart the mean of the three sensors will give the strain due to twist, see 4.5 for details. The remainder of the strain on cores 1-3 is due to the curvature. Thus, the following equations hold:

$$\epsilon_{i\kappa} = -\kappa r \cos\left(\theta_1 + \frac{2\pi}{3}(i-1)\right) \quad (4.5)$$

$$\epsilon_\tau = \frac{1}{3S} \sum_{i=1}^3 m_{i\Delta\epsilon} \quad (4.6)$$

where $i \in \{1, 2, 3\}$ is the sensor number, $\epsilon_{i\kappa} \in \mathbb{R}$ is the strain due to curvature κ on the FBG sensor in core i , r is the radial distance to the cores, $\theta_1 \in \mathbb{R}$ is the angle between the vector from center to core 1 and the curvature vector \mathbf{v} , $\epsilon_\tau \in \mathbb{R}$ is the strain on the cores due to twist, S is the gauge factor of the FBG sensors, $m_{i\Delta\epsilon} = m_i - m_4$ and $m_i \in \mathbb{R}$ is $\ln \frac{\lambda_B}{\lambda_{B0}}$, which is the measurement from sensor i . The curvature κ and twist $\Delta\phi$ can be evaluated as:

$$\kappa = \sqrt{v_1^2 + v_2^2} \quad (4.7)$$

$$\Delta\phi = \epsilon_\tau \frac{\Delta z}{Gr} \quad (4.8)$$

$$\text{where, } \mathbf{v} = \begin{bmatrix} v_1 \\ v_2 \end{bmatrix} = \begin{bmatrix} \kappa \cos(\theta_1) \\ \kappa \sin(\theta_1) \end{bmatrix} = \mathbf{C}^\dagger \boldsymbol{\zeta}, \quad \mathbf{C} = \begin{bmatrix} -Sr & 0 \\ \frac{1}{2}Sr & \frac{\sqrt{3}}{2}Sr \\ \frac{1}{2}Sr & -\frac{\sqrt{3}}{2}Sr \end{bmatrix}, \quad \boldsymbol{\zeta} = \begin{bmatrix} \zeta_1 \\ \zeta_2 \\ \zeta_3 \end{bmatrix}$$

\mathbf{C}^\dagger is the Moore-Penrose pseudo-inverse of \mathbf{C} and $\zeta_i = m_i - m_4 - S\epsilon_\tau$. Appendix 4.5 contains the derivations of (4.5)-(4.8).

The fiber's pose can be reconstructed using the curvature vectors and the twist values that are evaluated along its length. Let $n \in \mathbb{Z}_{>0}$ be the number of co-located sets of sensors. Then, the curvature vectors $\mathbf{v}[n]$ and twist values $\Delta\phi[n]$ can be acquired using (4.7) and (4.8). In this study $\Delta\phi[1]$ is set to be zero. The fiber is modeled as an elastic rod with the center-line represented by a unit-speed curve $\boldsymbol{\gamma}(s) \in \mathbb{R}^3$ and the material frames given by a set of orthonormal vectors $\{\mathbf{d}_1(s) \in \mathbb{R}^3, \mathbf{d}_2(s) \in \mathbb{R}^3, \mathbf{d}_3(s) \in \mathbb{R}^3\}$, where $s \in \mathbb{R}_{\geq 0}$ is the parameter for the arc length of the fiber, as illustrated

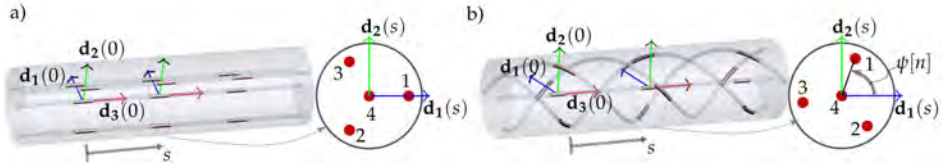


Figure 4.3: Schematic of the straight core fiber and the helical core fiber with the material frames $\{\mathbf{d}_1(s) \in \mathbb{R}^3, \mathbf{d}_2(s) \in \mathbb{R}^3, \mathbf{d}_3(s) \in \mathbb{R}^3\}$ are shown in a) and b), respectively. The arc length of the fiber is parameterized by $s \in \mathbb{R}$, the sensor set number is parameterized by $n \in \mathbb{Z}$, $\psi[n] \in \mathbb{R}$ is the angle between \mathbf{d}_1 and core 1 in set n .

in Figure 4.3. The equations for an elastic rod are as follows:

$$\frac{d}{ds} \boldsymbol{\gamma}(s) = \mathbf{d}_3(s) \quad (4.9)$$

$$\frac{d}{ds} \mathbf{d}_1(s) = \tilde{\phi}(s) \mathbf{d}_2(s) - \tilde{\chi}_2(s) \mathbf{d}_3(s) \quad (4.10)$$

$$\frac{d}{ds} \mathbf{d}_2(s) = -\tilde{\phi}(s) \mathbf{d}_1(s) + \tilde{\chi}_1(s) \mathbf{d}_3(s) \quad (4.11)$$

$$\frac{d}{ds} \mathbf{d}_3(s) = \tilde{\chi}_2(s) \mathbf{d}_1(s) - \tilde{\chi}_1(s) \mathbf{d}_2(s) \quad (4.12)$$

where, $\tilde{\phi}(s) \in \mathbb{R}$, $\tilde{\chi}_1(s) \in \mathbb{R}$ and $\tilde{\chi}_2(s) \in \mathbb{R}$ are the rotations of the center-line $\boldsymbol{\gamma}(s) \in \mathbb{R}^3$ about $\mathbf{d}_3(s)$, $\mathbf{d}_1(s)$ and $\mathbf{d}_2(s)$, respectively [14]. These rotations are related to the curvature $\mathbf{v}[n]$ and twist $\Delta\phi[n]$ calculated from the FBG sensors. For both the helical and straight core fiber, linearly interpolating $\Delta\phi[n]$ over the arc length s gives the rotation about $\mathbf{d}_3(s)$ which is $\tilde{\phi}(s)$. Similarly, for the straight core fiber, linear interpolation of $v_1[n]$ and $v_2[n]$ gives $\tilde{\chi}_1(s)$ and $\tilde{\chi}_2(s)$, respectively. However, for the helical core fiber since $\mathbf{d}_1(s)$ does not coincide with core 1 for all s , the calculated curvature vector $\mathbf{v}[n]$ must be adjusted such that it is with respect to the material frame. This is achieved by subtracting the angle $\psi[n] \in \mathbb{R}$ between \mathbf{d}_1 and core 1 on cross-section of the sensor set n from $\theta_1[n]$, see Figure 4.3. The angle $\psi[n]$ is related to the rate at which the fiber is twisted in order to create the helical cores. Thus, $\psi[n]$ can be either calculated from the twist rate or deduced experimentally. For the helical core fiber $\tilde{\chi}_1(s)$ and $\tilde{\chi}_2(s)$ are interpolation of $\chi_1[n] = \kappa[n] \cos(\theta_1[n] - \psi[n])$ and $\chi_2[n] = \kappa[n] \sin(\theta_1[n] - \psi[n])$, respectively. Then, the pose of both the fibers can be acquired using the discretized solution of (4.9)-(4.12) which is:

$$\mathbf{X}(s + \Delta s) = \mathbf{X}(s) \exp(\mathbf{A}(s) \Delta s), \quad (4.13)$$

$$\text{where, } \mathbf{X}(s) = \begin{bmatrix} \mathbf{d}_1(s) & \mathbf{d}_2(s) & \mathbf{d}_3(s) & \boldsymbol{\gamma}(s) \\ 0 & 0 & 0 & 1 \end{bmatrix},$$

$$\mathbf{A}(s) = \begin{bmatrix} 0 & -\tilde{\phi}(s) & \tilde{\chi}_2(s) & 0 \\ \tilde{\phi}(s) & 0 & -\tilde{\chi}_1(s) & 0 \\ -\tilde{\chi}_2(s) & \tilde{\chi}_1(s) & 0 & 1 \\ 0 & 0 & 0 & 0 \end{bmatrix},$$

$\boldsymbol{\gamma}(0) = [0 \ 0 \ 0]^T$, $\mathbf{d}_1(0) = [1 \ 0 \ 0]^T$, $\mathbf{d}_2(0) = [0 \ 1 \ 0]^T$, and $\mathbf{d}_3(0) = [0 \ 0 \ 1]^T$ [18]. The fiber tip position is $\boldsymbol{\gamma}(L)$ and tip orientation in matrix form is $[\mathbf{d}_1(L) \ \mathbf{d}_2(L) \ \mathbf{d}_3(L)]$, where L is the length of the fiber. The equations for acquiring the curvature, twist and pose measurements are validated through a set of experiments which are presented in the next section.

4.3 Experiments and Results

The equations presented in the previous section are utilized in three experiments that are conducted to compare the curvature, twist, and pose measurement accuracy between two multi-core fibers, one with helical cores and another with straight cores. The FBG sensors in both the fibers are inscribed using phase masks and ultra-violet laser. They are inscribed in the multi-core fiber with straight cores in-house and in the multi-core fiber with helical cores by Fujikura (Tokyo, Japan). Table 4.1 lists the specifications of the fibers. The insertion loss of the straight core fiber including the fan-out is 1.5 dB and of the helical core fiber including the fan out is 2.2 dB. There are 8 sets of FBG sensors, where each set consists of four co-located sensors that have the same Bragg wavelength. In the straight core fiber, the Bragg wavelengths range from 1537 nm to 1554 nm with an increment of approximately 2 nm. In the helical core fiber, the Bragg wavelengths range from 1542 nm to 1556 nm with an increment of approximately 2 nm. The light source and the spectrum analyzer for the sensors are provided by the interrogator FBG-804D (FBGS International NV, Geel). The wavelength data is processed offline in Matlab 2017b (MathWorks, Massachusetts).

4.3.1 Curvature

The experiments for curvature accuracy utilizes an acrylic board with seven fixed curvature slots that range from 1.33 m^{-1} to 5.71 m^{-1} . These slots are created using laser cutter and then smoothed by fine sandpaper. Figure 4.4a shows a photograph of the board. The accuracy of the two fibers are

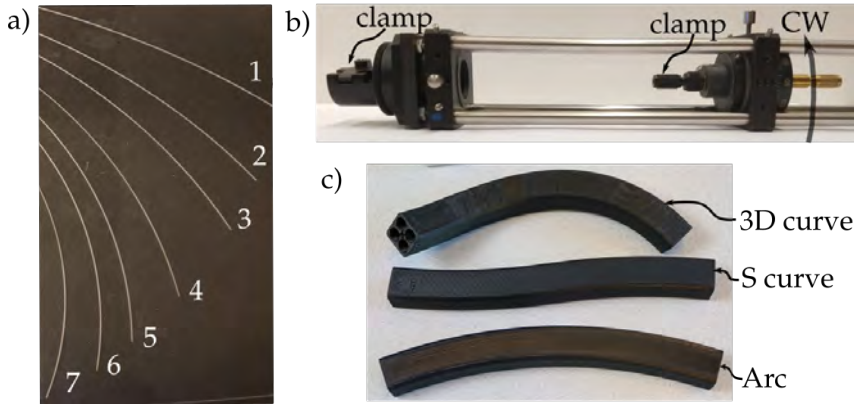


Figure 4.4: a) Slots of fixed curvature on an acrylic board used for determining curvature accuracy of the two multi-core fibers. Each slot is numbered and has a unique curvature in the range from 1.33 m^{-1} to 5.71 m^{-1} . b) A cage mechanism where a fiber can be clamped such that one end is fixed and the other end can be rotated. This setup is utilized for the twist experiments, where the fiber is rotated in clockwise (CW) and counter-clockwise (CCW) directions in steps of 10° . The distance between the two clamps is 175 mm . c) The three moulds used for the pose experiments. The arc has a constant curvature of 3.33 m^{-1} , the S curve has a linearly changing curvature starting from 2.5 m^{-1} to -2.5 m^{-1} and the 3D curve is a helix with radius of 0.1 m and pitch of $2.05 \times 10^{-1} \text{ m}$.

evaluated by placing them in the slots and getting the difference between the measured curvature and the curvature of the slot. Figure 4.5a plots each slot's curvature as the ground truth and the corresponding calculated

Table 4.1: Specifications of the straight and helical multi-core fibers

Core	Sensorized Length	FBG Length	Twist rate	Center to Core
Helical	175 mm	11 mm	50 turns/m	$35 \mu\text{m}$
Straight	115.5 mm	10 mm	N/A	$35 \mu\text{m}$
Core	Cladding diameter	Coating diameter	Core angles	Coating type
Helical	$125 \mu\text{m}$	$200 \mu\text{m}$	120°	Acrylate
Straight	$125 \mu\text{m}$	$250 \mu\text{m}$	120°	Acrylate

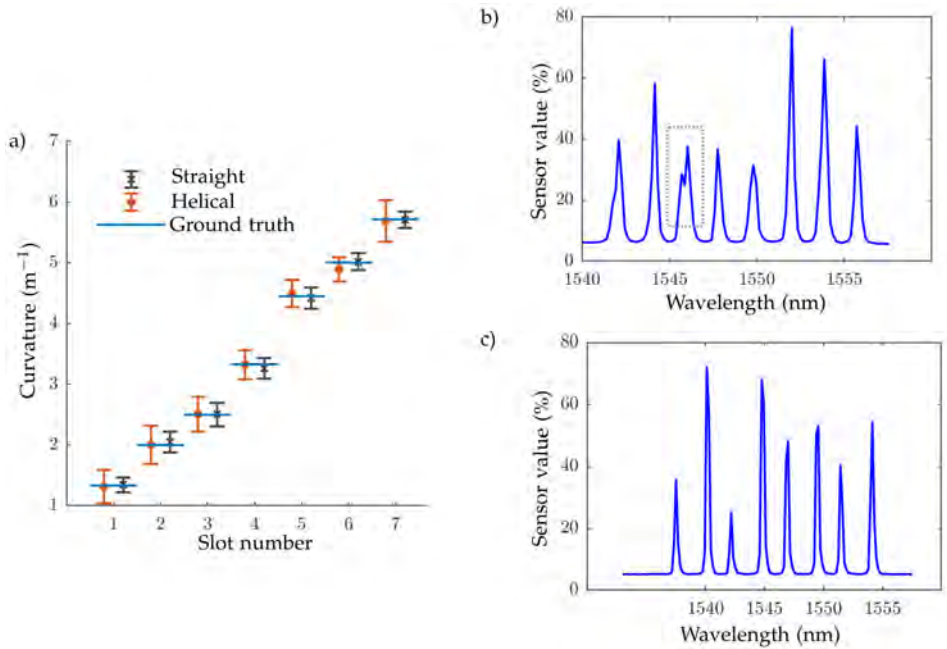


Figure 4.5: a) The mean and standard deviation of the curvature measurements along with the ground truth. The slot number is a unique number given to each slot with fixed curvature and the slot's curvature is the ground truth value. b) A spectra from fiber Bragg grating sensors on the helical core fiber with double peaks, which are highlighted with a gray dashed box. c) A spectra from fiber Bragg grating sensors on the straight core fiber.

curvature using (4.7), where r is the center to core distance of the fiber and S is determined through calibration for each FBG set. The calibration procedure consists of collecting measurements from the fiber and solving for the value of S that leads to the minimum difference between the measurements and the ground truth. The curvature error measure $\kappa_e \in \mathbb{R}_{\geq 0}$ utilized is the absolute difference between the ground truth $\kappa_{gt} \in \mathbb{R}_{\geq 0}$ and the measured curvature $\kappa_m \in \mathbb{R}_{\geq 0}$:

$$\kappa_e = |\kappa_{gt} - \kappa_m|, \quad (4.14)$$

The error κ_e is calculated for each sensor set and the mean error of the sensor sets over all the slots is 0.22 m^{-1} and 0.13 m^{-1} for helical and straight core fiber, respectively. The standard deviation of the error is 0.11 m^{-1} and 0.07 m^{-1} for helical and straight core fiber, respectively. The results show that

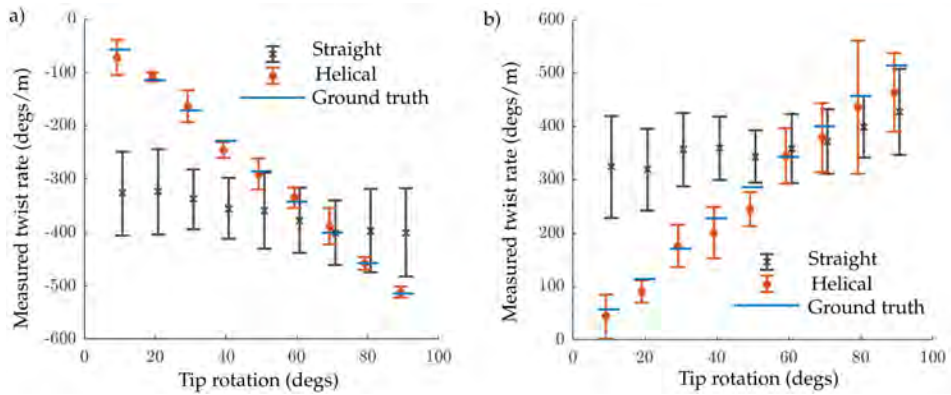


Figure 4.6: The mean and standard deviation of the twist measurements in clock-wise (a) and counter-clockwise direction (b).

the straight core fiber is more accurate in measuring the curvature however not significantly more. One source of inaccuracy in the helical fiber could be due to multiple peaks reflected from the sensors when the slot curvature is greater than 4 m^{-1} . For this study the mean of the multi-peaks is considered to be the shifted Bragg wavelength. Figure 4.5b illustrates a spectra, where one of the sensors has double peaks. The phenomenon of multiple peaks may be reduced by using apodized FBG sensors.

4.3.2 Twist

The accuracy of measuring twist using the two fibers is determined by clamping one end of the fiber and applying a rotation at the other end, which is the tip of the fiber. This experiment is conducted using an in-house assembled cage mechanism, as shown in Figure 4.4b. The rotating end of the mechanism consists of a dial with angular graduations of five degrees. During the experiment, the fiber is clamped on both ends and the dial is rotated in steps of 10° from 10° to 90° in clockwise (CW) and counter-clockwise (CCW) directions, as shown in Figure 4.4b. The error in twist measurement $\phi_e \in \mathbb{R}$ is determined by the absolute difference between the applied twist $\phi_{app} \in \mathbb{R}$ and the measured twist $\phi_m \in \mathbb{R}$ as per the following equation:

$$\phi_e = |\phi_{app} - \phi_m|, \quad (4.15)$$

The measured twist ϕ_m is calculated using (4.8), where Δz is the distance between the FBG sensor sets, r is the center to core distance. G is de-

terminated by calibration where a set of experiment data is used to find the value of G for which the twist error is minimized. Figure 4.6 shows the plot of the ground truth, which is the applied twist, and the measured twist for both the straight and helical core fiber. The applied twist along the fiber is related to the tip rotation as: $\phi_{app} = \theta_t/L$ where, $\theta_t \in \mathbb{R}$ is the tip rotation and L is 175 mm since that is the fiber length over which the twist is applied. The mean twist error is 26.57 degrees/m and 146.50 degrees/m for helical and straight core fibers, respectively. The standard deviation in twist error is 29.96 degrees/m and 59.74 degrees/m for helical and straight core fibers, respectively.

The results show that the helical core fiber can measure the twist with more accuracy than the straight core fiber. This is because with the straight core the FBG sensing of shear strain is very low whereas in helical core since the FBGs are on a helix the twist translates into elongation thus the FBG sensors register the shear strain more accurately. Another observation is that the helical core fiber does not have a symmetric response for clockwise and counter-clockwise twist. This could be due to the non-symmetric response of the sensors to elongation and compression.

4.3.3 Pose

In this experiment, each of the two fibers is placed in a catheter which is then placed in three moulds with the following center-line curve: arc, S curve and 3D curve, as shown in Figure 4.4c. The arc is a planar curve with a constant curvature of 3.33 m^{-1} , the S curve is also a planar curve with curvature changing from 2.5 m^{-1} to -2.5 m^{-1} , lastly the 3D curve is a segment of a helix with radius of 0.1 m and pitch of $2.05 \times 10^{-1} \text{ m}$. Thus, the tip pose of the three curves are known and utilized as ground truths. The tip pose of the fiber is acquired using (4.13), where $\psi[n]$ is found by placing the fiber in a fixed curvature slot and calculating the difference between the measured frame and the actual frame. Moreover, the fiber tip position $\mathbf{r} \in \mathbb{R}^3$ is $\gamma(L)$, where L is the length from the first sensor set to the last. The orientation of the fiber tip is given by the material frames \mathbf{d}_1 , \mathbf{d}_2 , \mathbf{d}_3 , since they are orthonormal they form an orientation matrix and the orientation at the tip is given by the matrix $[\mathbf{d}_1(L) \ \mathbf{d}_2(L) \ \mathbf{d}_3(L)]$. For error calculations we use axis-angle representation of orientation that is derived from the tip orientation matrix [19]. The axis which is the tip orientation vector is given as $\mathbf{v} \in \mathbb{R}^3$ and the angle which is the angle of rotation about the orientation vector is given as $\omega \in \mathbb{R}$. The pose error measures are calculated as follows [18]:

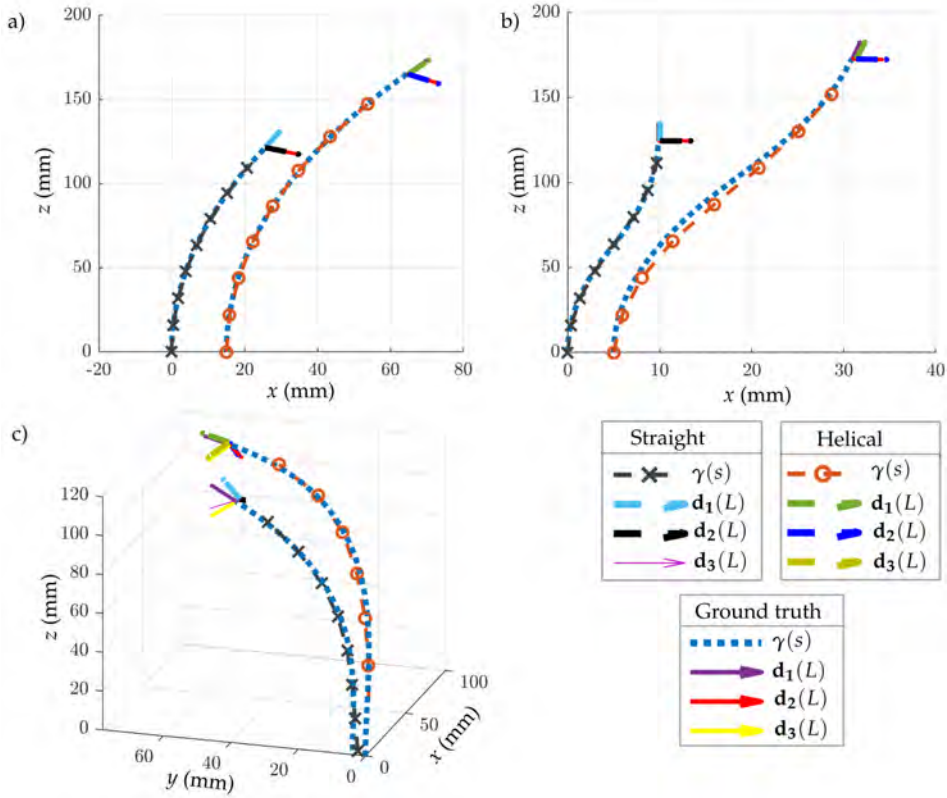


Figure 4.7: The pose measurement based on the fiber Bragg grating sensors and the ground truth for the three moulds. The helical core measurements in the plots are shifted about the x axis for visual clarity. The curves for the straight core fiber is shorter than the helical core fiber because the sensorized length of the straight and helical core fiber are 115.5 mm and 175 mm, respectively. The tip pose and the center-line of the straight and helical core fiber for the arc, S curve and 3D curve are shown in (a), (b) and (c), respectively.

$$r_e = \|\mathbf{r} - \mathbf{r}_{gt}\| \quad (4.16)$$

$$v_e = \cos^{-1} \left(\frac{\mathbf{v}_{gt} \cdot \mathbf{v}}{\|\mathbf{v}_{gt}\| \|\mathbf{v}\|} \right) \quad (4.17)$$

$$\omega_e = \|\omega - \omega_{gt}\| \quad (4.18)$$

where, $\mathbf{r}_{gt} \in \mathbb{R}^3$ is the ground truth of the tip position, $\mathbf{v}_{gt} \in \mathbb{R}^3$ is the true orientation vector and $\omega_{gt} \in \mathbb{R}$ is the angle of rotation about the true orientation vector. The catheter with the fiber is inserted in each mould five times. Table 4.2 gives the mean pose errors and the standard deviation over all the trials. Figure 4.7 shows the reconstructions of the three curves and the tip pose for one of the trials. The results show that both the fibers have similar error measures, however the helical core fiber gives a slightly lower error in orientation for the space curve pose.

4.4 Conclusions

In this study, multi-core fibers with FBG sensors are utilized to acquire curvature, twist and pose measurements. Moreover, the accuracy of the measurements from the FBG sensors in a helical core fiber is compared to that of the sensors in a straight core fiber. The mean error in curvature for helical and straight core fiber are 0.22 m^{-1} and 0.13 m^{-1} , respectively, whereas in twist measurement the mean error measures are 26.57 degrees/m and 146.50 degrees/m , respectively. Lastly, the mean error in position for the helical and straight core fiber are 0.49 mm and 0.27 mm , respectively; in axis orientation is 0.12 degrees and 0.26 degrees ; and in angle orientation is 1.10 degrees and 1.18 degrees , respectively. The accuracy for the pose measurement is similar for both fibers. However, for applications with twist, FBG sensors on helical core fiber will produce more accurate results than FBG sensors on straight core fiber.

Acknowledgements

The authors would like to thank Francis Kalloor Joseph and Frans Segerink from University of Twente for their assistance in building the twist experiment setup. In addition, the authors really appreciate the assistance pro-

Table 4.2: The mean and standard deviation in brackets over multiple trials of the position, axis and angle error according to (4.16)- (4.18), respectively.

	Helical	Straight
r_e (mm)	0.49 (0.24)	0.27 (0.14)
v_e (degs)	0.12 (0.16)	0.26 (0.14)
ω_e (degs)	1.10 (0.71)	1.18 (1.06)

vided by Fujikura in understanding the spectra from the helical core fibers and by FBGS International NV with the strain to wavelength equation.

4.5 Appendix

The derivation of (4.5)-(4.8) is given in this appendix. The curvature and twist are evaluated from the Bragg wavelength measurements of the FBG sensors. First, the strain on the fiber is calculated from the wavelength measurements and then the curvature and twist is evaluated from the strain using material mechanics [15]. The relation between the strain and the wavelength is given in (4.4) as:

$$\ln \frac{\lambda_B}{\lambda_{B0}} = S(\epsilon - \epsilon_0) + \Sigma(T - T_0), \quad (4.19)$$

The left hand side of (4.19) is a direct measurement from the sensors. Let $i \in \{1, 2, 3, 4\}$ represent the FBG sensor number,

$$\ln \frac{\lambda_{Bi}}{\lambda_{B0i}} = m_i, \quad \text{and} \quad (4.20)$$

$$S(\epsilon_i - \epsilon_{0i}) = S(\epsilon_{i\kappa} + \epsilon_\tau) = m_i \Delta\epsilon, \quad (4.21)$$

where $m_i \in \mathbb{R}$, (4.21) is based on $\epsilon_{0i} = 0$ which is true if λ_{B0i} is measured when fiber is stress-free. $\epsilon_{i\kappa} \in \mathbb{R}$ is strain due to curvature and ϵ_τ is axial twist strain which is the same in sensors 1, 2 and 3. All four FBG sensors will experience the same temperature change because they are close in proximity, thus the value of the term $\Sigma(T - T_0)$ is the same in all sensors. Moreover, sensor 4 theoretically will be strain free because it is in the center of the fiber, thus:

$$\Sigma(T_i - T_{0i}) = m_4. \quad (4.22)$$

$$\epsilon_{i\kappa} = -\kappa r \cos \left(\theta_1 + \frac{2\pi}{3}(i-1) \right), \quad (4.23)$$

where $\epsilon_{i\kappa} \in \mathbb{R}$ is the strain is sensor $i \in \{1, 2, 3\}$; $\epsilon_{4\kappa} = 0$. (4.23) is based on material mechanics, for further details see Khan *et. al* [1]. The following holds for sensors $i \in \{1, 2, 3\}$ using (4.20)-(4.21):

$$m_i = m_i \Delta\epsilon + m_4 \quad (4.24)$$

Substituting (4.21), (4.23) into (4.24) and applying trigonometric angle sum identities the following holds:

$$m_1 - m_4 = m_{1\Delta\epsilon} = S(-\kappa r \cos(\theta_1) + \epsilon_\tau) \quad (4.25)$$

$$m_2 - m_4 = m_{2\Delta\epsilon} = S\left(\frac{1}{2}\kappa r \cos(\theta_1) + \frac{\sqrt{3}}{2}\sin(\theta_1) + \epsilon_\tau\right) \quad (4.26)$$

$$m_3 - m_4 = m_{3\Delta\epsilon} = S\left(\frac{1}{2}\kappa r \cos(\theta_1) - \frac{\sqrt{3}}{2}\sin(\theta_1) + \epsilon_\tau\right) \quad (4.27)$$

Summing (4.25)- (4.27) leads to the trigonometry terms to add to zero and the following is achieved:

$$\frac{1}{3S} \sum_{i=1}^3 m_{i\Delta\epsilon} = \epsilon_\tau \quad (4.28)$$

Thus, the strain due to twist can be calculated using (4.28) and the twist can be calculated by rearranging (4.2) into:

$$\Delta\phi = \epsilon_\tau \frac{\Delta z}{Gr}, \quad (4.29)$$

which is the twist equation (4.8). The curvature value can be solved by rearranging (4.25)- (4.27) as

$$\zeta = \mathbf{C}\mathbf{v}, \quad (4.30)$$

$$\text{where, } \zeta = \begin{bmatrix} \zeta_1 \\ \zeta_2 \\ \zeta_3 \end{bmatrix} = \begin{bmatrix} m_1 - m_4 - S\epsilon_\tau \\ m_2 - m_4 - S\epsilon_\tau \\ m_3 - m_4 - S\epsilon_\tau \end{bmatrix} \quad \mathbf{C} = \begin{bmatrix} -Sr & 0 \\ \frac{1}{2}Sr & \frac{\sqrt{3}}{2}Sr \\ \frac{1}{2}Sr & -\frac{\sqrt{3}}{2}Sr \end{bmatrix}$$

$$\mathbf{v} = \begin{bmatrix} v_1 \\ v_2 \end{bmatrix} = \begin{bmatrix} \kappa \cos(\theta_1) \\ \kappa \sin(\theta_1) \end{bmatrix}$$

Then $\mathbf{v} = \mathbf{C}^\dagger \zeta$, where \mathbf{C}^\dagger is the Moore-Penrose pseudo-inverse of \mathbf{C} and

$$\kappa = \|\mathbf{v}\| = \sqrt{v_1^2 + v_2^2} \quad (4.31)$$

gives the curvature equation (4.7).

References

- [1] **F. Khan**, A. Denasi, D. Barrera, J. Madrigal, S. Sales, and S. Misra, “Multi-core optical fibers with Bragg gratings as shape sensor for flexible medical instruments,” *IEEE Sensors Journal*, vol. 19, no. 14, pp. 5878–5884, 2019.
- [2] P. S. Westbrook, T. Kremp, K. S. Feder, W. Ko, E. M. Monberg, H. Wu, D. A. Simoff, T. F. Taunay, and R. M. Ortiz, “Continuous multicore optical fiber grating arrays for distributed sensing applications,” *Journal of Lightwave Technology*, vol. 35, no. 6, pp. 1248–1252, 2017.
- [3] A. Wolf, A. Dostovalov, K. Bronnikov, and S. Babin, “Arrays of fiber Bragg gratings selectively inscribed in different cores of 7-core spun optical fiber by IR femtosecond laser pulses,” *Opt. Express*, vol. 27, no. 10, pp. 13 978–13 990, 2019.
- [4] C. G. Askins, G. A. Miller, and E. J. Friebele, “Bend and twist sensing in a multi-core optical fiber,” in *Proceedings of 21st Annual Meeting of the IEEE Lasers and Electro-Optics Society*, pp. 109-110, Acapulco, Mexico, 2008.
- [5] J. P. Moore and M. D. Rogge, “Shape sensing using multi-core fiber optic cable and parametric curve solutions,” *Opt. Express*, vol. 20, no. 3, pp. 2967–2973, 2012.
- [6] S. Jäckle, T. Eixmann, H. Schulz-Hildebrandt, G. Hüttmann, and T. Pätz, “Fiber optical shape sensing of flexible instruments for endovascular navigation,” *International Journal of Computer Assisted Radiology and Surgery*, vol. 14, pp. 2137–2145, 2019.
- [7] R. Xu, A. Yurkewich, and R. V. Patel, “Curvature, torsion, and force sensing in continuum robots using helically wrapped FBG sensors,” *IEEE Robotics and Automation Letters*, vol. 1, no. 2, pp. 1052–1059, 2016.
- [8] R. J. Roesthuis, M. Kemp, J. J. van den Dobbelsteen, and S. Misra, “Three-dimensional needle shape reconstruction using an array of fiber Bragg grating sensors,” *IEEE/ASME Transactions on Mechatronics*, vol. 19, no. 4, pp. 1115–1126, 2014.
- [9] R. G. Duncan and M. T. Raum, “Characterization of a fiber-optic shape and position sensor,” in *Proceedings of Smart Structures and Materials*

-
- 2006: *Smart Sensor Monitoring Systems and Applications*, pp. 26-36, California, USA, 2006.
- [10] Y. Wang, C. Xu, and V. Izraelian, "Bragg gratings in spun fibers," *IEEE Photonics Technology Letters*, vol. 17, no. 6, pp. 1220–1222, 2005.
- [11] H. Zhang, Z. Wu, P. P. Shum, X. Shao, R. Wang, X. Q. Dinh, S. Fu, W. Tong, and M. Tang, "Directional torsion and temperature discrimination based on a multicore fiber with a helical structure," *Opt. Express*, vol. 26, no. 1, pp. 544–551, 2018.
- [12] I. Floris, J. Madrigal, S. Sales, P. A. Calderòn, and J. M. Adam, "Twisting compensation of optical multicore fiber shape sensors for flexible medical instruments," in *Proceedings of Optical Fibers and Sensors for Medical Diagnostics and Treatment Applications XX*, pp. 128-132, California, USA, 2020.
- [13] V. Budinski and D. Donlagic, "Fiber-optic sensors for measurements of torsion, twist and rotation: A review," *Sensors (Basel)*, vol. 17, no. 3, pp. 443–472, 2017.
- [14] B. Audoly and Y. Pomeau, *Elasticity and geometry : From hair curls to the non-linear response of shells*. New York: Oxford University Press, 2010.
- [15] R. C. Hibbeler, *Mechanics of Materials 8th ed.* Upper Saddle River, New Jersey: Pearson Prentice Hall, 2011.
- [16] R. J. Roesthuis, S. Janssen, and S. Misra, "On using an array of fiber Bragg grating sensors for closed-loop control of flexible minimally invasive surgical instruments," in *IEEE/RSJ International Conference on Intelligent Robots and Systems*, pp. 2545-2551, Tokyo, Japan, 2013.
- [17] J. V. Roosbroeck, C. Chojetzki, J. Vlekken, E. Voet, and M. Voet, "A new methodology for fiber optic strain gage measurements and its characterization," in *Proceedings of the SENSOR+TEST Conferences*, vol. OPTO 2 - Optical Fiber Sensors, pp. 59 - 64, Nürnberg, Germany, May 2009.
- [18] **F. Khan**, A. Donder, S. Galvan, F. Rodriguez y Baena, and S. Misra, "Pose measurement of flexible medical instruments using fiber Bragg gratings in multi-core fiber," *IEEE Sensors Journal*, vol. 20, no. 18, pp. 10 955–10 962, 2020.

- [19] J. J. Craig, *Introduction to Robotics: Mechanics and Control, third ed.* Upper Saddle River, New Jersey: Pearson Prentice Hall, 2005.

Part III

Application Studies

In the previous part, the theoretical framework for shape and pose measurement was presented. In this part the sensing framework is applied to various experimental studies. In Chapter 5, the shape sensing algorithm is used to track a magnetically actuated catheter. Next in Chapter 6, the force at the tip of a tendon driven manipulator is estimated based on the shape of the manipulator. These studies demonstrate the applications of shape sensing algorithms presented in previous part. Both the chapters are based on the following peer reviewed publications:

- A. Denasi, **F. Khan**, K. J. Boskma, M. Kaya, C. Hennersperger, R. Göbl, M. Tirindelli, N. Navab, and S. Misra, “An observer-based fusion method using multicore optical shape sensors and ultrasound images for magnetically-actuated catheters”, in *Proceedings of the IEEE International Conference on Robotics and Automation*, pp. 50-57, Queensland, Australia, 2018.
- **F. Khan**, R. J. Roesthuis, and S. Misra, “Force sensing in continuum manipulators using Fiber Bragg Grating sensors”, in *Proceedings of the IEEE International Conference on Intelligent Robots and Systems*, British Columbia, Canada, pp. 2531-2536, 2017.

Chapter 5

Catheter Tracking

Abstract

Minimally invasive surgery involves using flexible medical instruments such as endoscopes and catheters. Magnetically actuated catheters can provide improved steering precision over conventional catheters. However, besides the actuation method, an accurate tip position is required for precise control of the medical instruments. In this study, the tip position obtained from transverse 2D ultrasound images and multicore optical shape sensors are combined using a robust sensor fusion algorithm. The tip position is tracked in the ultrasound images using a template-based tracker and a convolutional neural network based tracker, respectively. Experimental results for a rhombus path are presented, where data obtained from both tracking sources are fused using Luenberger and Kalman state estimators. The mean and standard deviation of the Euclidean error for the Luenberger observer is 0.2 ± 0.11 [mm] whereas for the Kalman filter it is 0.18 ± 0.13 [mm], respectively.

5.1 Introduction

Flexible medical instruments such as endoscopes, catheters and needles constitute an important set of tools used in minimally invasive surgery (MIS). The integration of robotic navigation with MIS is becoming increasingly popular due to the advances in sensing and actuation technologies [1]. Remote actuation of flexible catheters has been investigated using the conventional displacement tendons [2] and recently using external magnetic fields [3, 4]. Magnetic actuation is more favorable compared to tendons

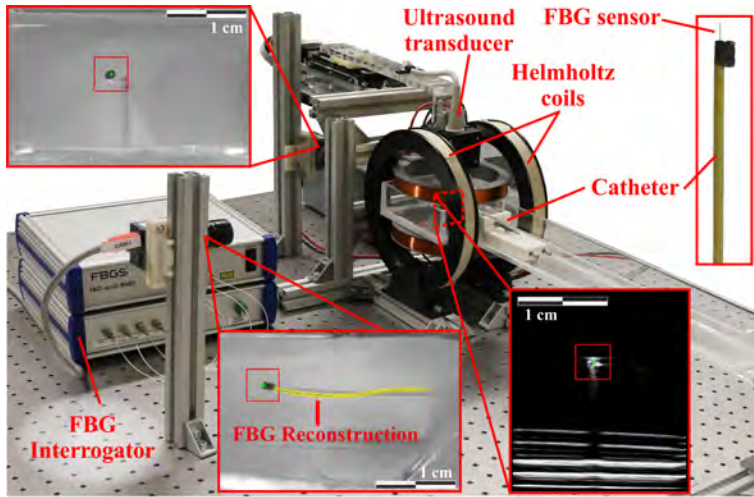


Figure 5.1: The magnetically-actuated flexible catheter setup: The magnetic field is generated by two pairs of Helmholtz coils. The flexible catheter has a stack of permanent magnets at its tip which are steered by the coils. The catheter tip is detected using 2D ultrasound images. The shape and tip pose of the catheter are also obtained using multi-core Fiber Bragg Grating sensors.

since it does not suffer from friction and hysteresis (Fig. 5.1).

Besides the actuation method, acquiring an accurate instrument tip pose is crucial for the success of robotically-guided MIS procedures, since the catheter tip is the end-effector. The tip pose is often acquired using medical imaging modalities such as ultrasound (US), fluoroscopy, computed tomography (CT) and magnetic resonance imaging (MRI). Among these modalities, US has the advantage of being easily accessible, safe to operate and the possibility to image using a hand-held probe. Further, ultrasound provides high acquisition rates, allowing sufficient feedback to allow for closed-loop control. Therefore, a two-dimensional (2D) US probe is used in this work to acquire transverse images of the catheter tip. Nonetheless, acquiring the tip pose using solely the US images is not sufficient. This is due to the fact the visual tracking methods used to estimate the tip pose from the acquired US images are prone to failure. The common reasons for this failure are the low signal-to-noise ratio and an excessive number of image artifacts in practice.

Besides image-based tracking, catheter poses can also be retrieved by shape sensing techniques to measure the tip pose [5], with common ap-

proaches such as fiber-optic-sensor-based and electromagnetic-tracking-based (EM) methods. Among the two methods, EM tracking is very challenging to be used in conjunction with magnetically-actuated catheters. Hence, Fiber Bragg Grating (FBG) sensors, a fiber-optic type of sensor, are used in this work. FBG sensors have been used for various purposes for catheters in medical robotics research [6]. Arkwright *et al.* investigated the measurement of the muscular activity in the gastrointestinal tract using diagnostic catheters with FBG's [7]. Xu *et al.* designed a temperature-insensitive contact force sensor for bi-directional catheters using an FBG pair [8]. Shi *et al.* presented a survey on the state-of-the art of shape sensing techniques for continuum robots used in minimally invasive surgery [5].

In the aforementioned studies, single core optical fibers are used to reconstruct the 3D shape of the catheters. Recently, Moore *et al.* have proposed using multi-core optical fibers [9]. They investigated reconstructing the shape of a multi-core optical fiber with Fiber Bragg Grating sensors by numerically solving the Frenet-Serret equations. Multi-core optical fibers have advantages over single-core optical fibers. For instance, the multi-core optical fibers occupy less space compared to a combination of multiple single core fibers. Further, the FBG sensors are easier to align on multi-core optical fibers. To the best of the authors' knowledge, multi-core optical fibers have not been used for shape reconstruction of flexible medical instruments. This study investigates the shape reconstruction of magnetically-actuated flexible catheters using multi-core FBGs.

The measurements obtained from multi-core FBGs can be a remedy to the aforementioned possible failure of visual tracking using US images. This is achieved by fusing the data from multi-core FBGs and US images, thereby increasing the success rate of visual tracking. In this study, sensor fusion using state estimators is investigated. The estimation performance of two different methods, namely a high gain Luenberger observer and Kalman filter are compared. A simple model with a suitable disturbance term is used in the design of the state estimators. To the best of the authors' knowledge, such an observer-based fusion algorithm has not been used in medical robotics applications.

The presented tracking and sensor fusion algorithm could potentially be used in clinical minimally invasive procedures such as transfemoral aortic valve implantation, atrial fibrillation, and angioplasty. The tip pose estimation accuracy achieved with this method can reduce the duration of the aforementioned surgical procedures and increase their safety.

The rest of the work is organized as follows: Section 5.2 describes the

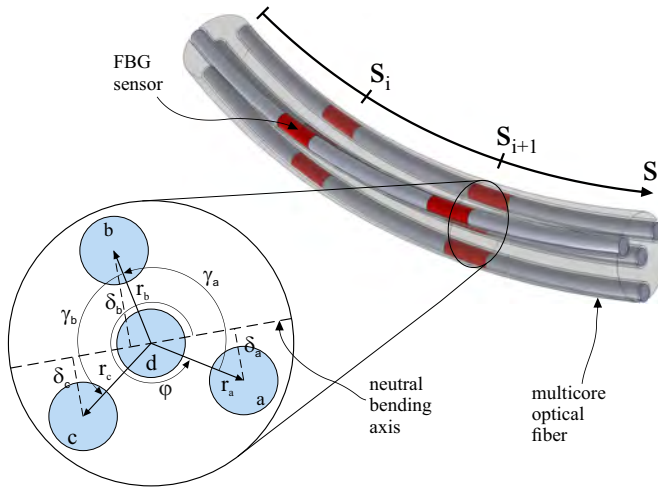


Figure 5.2: Section of a multicore fiber with Fiber Bragg Grating (FBG) sensors is shown. The fiber has 4 cores and each core has 32 FBG sensors.

shape sensing using multi-core FBGs. This is followed by the tracking algorithms for US images in Section 5.3. The sensor fusion algorithm is introduced in Section 5.4. Section 5.5 reports the results of the experiments. The conclusions are drawn in Section 5.6 and directions for future work are given.

5.2 Shape Sensing Using Fiber Bragg Gratings

This section describes the procedure to reconstruct the 3D shape of the magnetic catheter using sets of four FBG sensors placed along the length of the catheter [10]. The optical fiber used in this study contains four cores, where one of the cores is placed in the center axis of the fiber. The FBG sensors etched on the three cores placed around the center are used to measure the strains whereas the center core can be used for the purpose of temperature compensation. An FBG periodically modulates the refractive index in each core of the fiber. It reflects the light at a specific wavelength, called the Bragg wavelength λ_B . Variations in mechanical strain and temperature result in a change in the Bragg wavelength. The shift in the Bragg wavelength due to applied strain and temperature change is given by the

following exact differential form [11]:

$$\frac{d\lambda_B}{\lambda_B} = (1 - p_e) d\varepsilon + (\alpha_\lambda + \alpha_n) d\mathcal{T}, \quad (5.1)$$

where p_e , α_λ and α_n are the photoelastic, thermal expansion and thermo-optic coefficients, respectively. Further, ε and \mathcal{T} are the axial strain and temperature, respectively. After integrating both sides of (5.1) we obtain

$$\ln \frac{\lambda_B}{\lambda_{B,0}} = (1 - p_e) (\varepsilon - \varepsilon_0) + (\alpha_\lambda + \alpha_n) (\mathcal{T} - \mathcal{T}_0), \quad (5.2)$$

where $\lambda_{B,0}$, ε_0 and \mathcal{T}_0 indicate the reference Bragg wavelength, reference strain and reference temperature, respectively. It should be noted that equation (5.1) is often approximated without performing the above integration procedure (d is replaced by Δ and λ_B by $\lambda_{B,0}$) [10]. However, this introduces errors which increase for increasing strain. If the temperature change is assumed to be negligible (i.e. $\mathcal{T} - \mathcal{T}_0 \approx 0$), then the shift in the Bragg wavelength is due to the applied strain which simplifies (5.2) as follows:

$$\ln \frac{\lambda_B}{\lambda_{B,0}} = (1 - p_e) (\varepsilon - \varepsilon_0). \quad (5.3)$$

The axial strain ε measured by the FBG sensors placed on each core can be related to the distance of the fiber to the neutral axis (see Fig. 5.2) as follows:

$$\varepsilon = \frac{ds - dl}{dl} = \frac{(\rho - \delta) d\theta - \rho d\theta}{\rho d\theta} = -\frac{\delta}{\rho} = -\kappa\delta, \quad (5.4)$$

where κ is the curvature of the flexible catheter. Here, it is assumed that the catheter can be modeled as a beam in pure bending. The curvature and its direction are determined at a particular cross section using the three FBG sensors placed around the center (see Fig. 5.2) as follows:

$$\begin{aligned} \varepsilon_a - \varepsilon_0 &= -\kappa\delta_a = -\kappa r_a \sin(\varphi), \\ \varepsilon_b - \varepsilon_0 &= -\kappa\delta_b = -\kappa r_b \sin(\varphi + \gamma_a), \\ \varepsilon_c - \varepsilon_0 &= -\kappa\delta_c = -\kappa r_c \sin(\varphi + \gamma_a + \gamma_b), \end{aligned} \quad (5.5)$$

where φ is the angle between r_a and the neutral axis. Further, r_a , r_b and r_c are the distance of the cores a , b and c from the center, respectively. It is assumed that the position and orientation of the FBG sensors are known

and constant. The unknown parameters κ , φ and ε_0 can be determined by solving the set of equations (5.5). The curvature $\kappa(s_i)$ and its direction $\varphi(s_i)$ can be obtained at every location s_i by interpolating the measurements from FBG sensors placed on the catheter. These can then be used to compute the tangent vector of the curve of the catheter [12]. Consequently, the shape and respectively the tip pose of the flexible catheter is determined by numerical integration of the tangent vector.

5.3 Ultrasound Tracking Algorithm

In this section, two algorithms to obtain catheter pose information for given ultrasound images are introduced: i) a template based tracking algorithm, and ii) a tracking algorithm utilizing convolutional neural networks.

5.3.1 Template Based Tracking Algorithm

The ultimate goal of the template based tracking method is registering the template image of the catheter, $T(\mathbf{x})$ and current image of the catheter, $I(\mathbf{w}(\mathbf{x}, \mathbf{p}))$. Here, $\mathbf{x} \in \mathbb{R}^2$ contains the pixel coordinates $\mathbf{x} = [x, y]^T$, and is transformed by a motion model, which is also known as the warping function, $\mathbf{w}(\mathbf{x}, \mathbf{p})$. The aim of registration is to calculate the optimal value of the motion parameters, \mathbf{p} . The template based tracking algorithm described in this study is adapted from [13] and detailed in the following.

Motion Model

One of the most significant layers of visual tracking is determining the motion of a flexible catheter in the image plane. The motion model describes the transformation between the template and current images. The motion of a flexible catheter in the US image plane can be decomposed into translation and scaling transformations. These transformations can be described by an affine motion model, $\mathbf{w}(\mathbf{x}, \mathbf{p})$, given as follows:

$$\mathbf{w}(\mathbf{x}, \mathbf{p}) = \begin{bmatrix} 1 + p_1 & p_3 \\ p_2 & 1 + p_4 \end{bmatrix} \begin{bmatrix} x \\ y \end{bmatrix} + \begin{bmatrix} p_5 \\ p_6 \end{bmatrix}, \quad (5.6)$$

where $\mathbf{p} \in \mathbb{R}^6$ is the 6-DOF motion parameter vector. Further, the motion model (5.6) can be used to track the tip position of the flexible catheter.

While tracking the tip of the catheter, transient variations of its pixel values may occur. In order to estimate the catheter tip position with a high accuracy, the tracker must compensate for these intensity fluctuations. A

scale-offset model (α, β) can compensate these variations [14]. Then, the compensated current image $I^*(\mathbf{w}(\mathbf{x}, \mathbf{q}))$, is written as:

$$I^*(\mathbf{w}(\mathbf{x}, \mathbf{q})) = (\alpha + 1)I(\mathbf{w}(\mathbf{x}, \mathbf{p})) + \beta. \quad (5.7)$$

Using the affine motion and scale-offset models, eight parameters $\mathbf{q} \in \mathbb{R}^8$ are calculated for the transformation from the template to the current image during the visual tracking, where $\mathbf{q} = [\mathbf{p}^T, \alpha, \beta]^T$. In the rest of this section, the calculation of \mathbf{q} vector using the SSD cost function is explained.

SSD-based Visual Tracking

The sum of squared differences (SSD) between $I^*(\mathbf{w}(\mathbf{x}, \mathbf{p}))$ and $T(\mathbf{x}) : \mathbb{R}^2 \rightarrow \mathbb{R}$ can be computed as follows:

$$SSD(\mathbf{q}) = \sum_{\mathbf{x}} [I^*(\mathbf{w}(\mathbf{x}, \mathbf{q})) - T(\mathbf{x})]^2. \quad (5.8)$$

The main goal of SSD based visual tracking is to find the vector \mathbf{q} that minimizes the SSD value between $T(\mathbf{x})$ and $I^*(\mathbf{w}(\mathbf{x}, \mathbf{q}))$. For this purpose, forward or inverse compositional methods [15], first order optimization, or efficient second order minimization (ESM) methods [16] can be used. In this study, an ESM method is used since it is more robust to noise and its convergence rate is higher as compared to other optimization methods. Using ESM, the vector \mathbf{q} is iteratively computed by accumulating $\Delta\mathbf{q}$ in each iteration ($\mathbf{q} \leftarrow \mathbf{q} + \Delta\mathbf{q}$). $\Delta\mathbf{q}$ is computed using ESM as follows:

$$\Delta\mathbf{q} = -2(\mathbf{J}(\mathbf{q}_0) + \mathbf{J}(\mathbf{q}_c))^\dagger (I^*(\mathbf{w}(\mathbf{x}, \mathbf{q})) - T(\mathbf{x})), \quad (5.9)$$

where \dagger is the Moore-Penrose pseudoinverse of a matrix. Further, $\mathbf{J}(\mathbf{q}_0)$ and $\mathbf{J}(\mathbf{q}_c)$ are the Jacobian of $I^*(\mathbf{w}(\mathbf{x}, \mathbf{q}))$ [14, 16]. Before the iteration loop starts, $\mathbf{J}(\mathbf{q}_0)$ is pre-computed. During the iterations, first $\mathbf{J}(\mathbf{q}_c)$ is computed and then $\Delta\mathbf{q}$ is calculated using (5.9). Iterations last until the number of iterations reach a predefined maximum iteration number or sum of $\Delta\mathbf{q}$ vector elements are smaller than the predefined threshold.

Pyramidal Implementation

In our experiments, it was observed that the motion of the flexible catheter can be very large in the US image plane. In this situation, the displacement of the catheter between the previous and the current US frames can

be large. Hence, the number of iterations to calculate the motion parameters between the template and current images increases dramatically. Further, the catheter can be so far away from the search region in the image plane that tracking might fail. In order to increase the convergence rate and robustness of the tracking, pyramidal implementation of the proposed template-based tracking method is applied [17]. During the tracking, optimization methods are first applied to the coarsest level of pyramid and then, results are transferred to the next finer level of the pyramid. The number of pyramid layer for the frames in our data set and imaging system was selected as two. If the number of pyramid layers in the experiments was more than two, significant texture loss was observed because our maximum template size is 40×40 pixels.

Template Update Strategy

During the tracking, the template images are updated with a drift correction strategy to minimize the registration error and prevent template drifts [18]. This strategy consists of two registration steps. In the first step, the template and current images are registered. In the second step, the output image obtained in the first step is registered with the master template. The master template is the first appearance of the flexible catheter in the US image. After the second step, the template image is updated with registration output obtained in the second step.

5.3.2 Convolutional Neural Network Based Tracking

In this section, a tracking approach utilizing a Convolutional Neural Network (CNN) is presented. Fully convolutional neural networks have been shown to be well suited for the imaged-based estimation of object positions. When applied to the task of human pose estimation, the works of Newell et al. [19] and Wei et al. [20] demonstrated improved tracking performance compared to naive joint coordinate regression. In these works, fully convolutional neural networks are trained to predict a dense probability map, providing the probability for each pixel to contain the object of interest.

Following this approach, we propose a CNN architecture based on the work of Milletari et al. [21], originally described for segmentation of magnetic resonance images. As shown in Fig. 5.3, the network architecture consists of an encoding and a decoding branch, both organized in different levels. At each level of the encoding part, the input data are processed with a set of convolutional layers, the residuals are computed and downsampled

by means of an additional convolutional layer, which stride size is set to two in both x and y direction. When moving toward deepest levels in the encoding branch, the resolution of the features maps decreases, while the number of filters in each convolutional layer increases. At the last level of the encoding branch, the resolution is lowered to 23×24 , while the number of channels is 256.

The decoding branch of the structure is employed to retrieve the original resolution. As the encoding branch, it is organized in different levels. At each level of the decoding branch, the input data is concatenated with the output of the correspondent level in the encoding branch forming a so called skip-connection, and subsequently processed with a set of convolutional layers. Residuals are then computed and upsampled by means of a deconvolution layer. When moving from lower to higher levels in the right branch, the resolution of the features maps increases again, while the number of channels decreases. The output of the last deconvolution is processed with two convolutional layers, which reduces the number of channels of the output features map to one. Though the whole network $\tanh(\cdot)$ activation is applied after the convolutional layers, as it sped up training compared to the original ReLU.

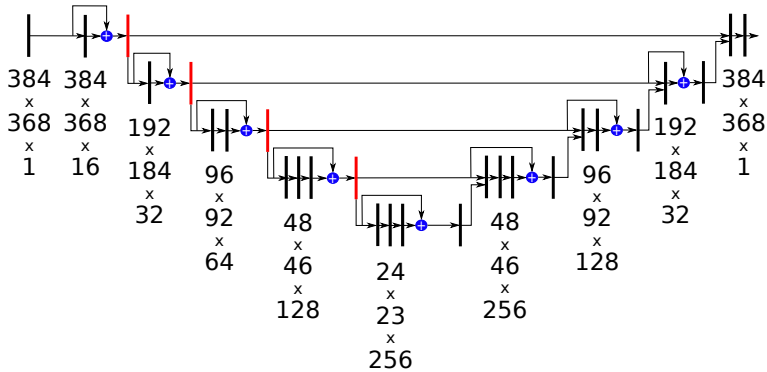


Figure 5.3: Architecture of the convolutional neural network, with the encoding branch left and the decoding branch of inverse structure right.

During network training, the network output is compared to the ground truth images to compute the loss. Ground truth images consist in heatmaps, where decreasing intensities are associated to pixels with increasing distance from the catheter tip. The heatmap intensity at pixel (x, y) provides the probability that the catheter’s tip is located at (x, y) , given the Ground

Truth tip location (x_t, y_t) ,

$$\text{HM}(x, y) = \mathcal{P}((x, y)|(x_t, y_t)), \quad (5.10)$$

where $\text{HM}(x, y)$ is the heatmap intensity value at pixel (x, y) .

Under the assumption that $\mathcal{P}((x, y)|(x_t, y_t))$ follows a Gaussian distribution, ground truth heatmaps can be computed as the 2D Gaussian centered in (x_t, y_t) .

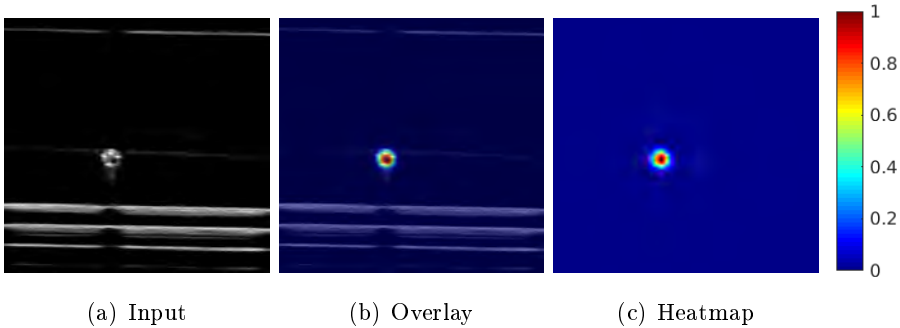


Figure 5.4: Convolutional neural network based tracking results of a flexible catheter in a 2D transverse ultrasound image.

An exemplary output of the network can be seen in Fig. 5.4. The Loss function used for training is defined as

$$Loss = \sum_{k \in B} \left[\frac{1}{2} \sum_i (\text{HM}_i^k - P_i^k)^2 + \omega R^k \right], \quad (5.11)$$

where B is the minibatchsize, HM_i is the i^{th} pixel of the ground truth heatmap, P_i is the i^{th} pixel of the predicted map, R^k is a regularization term and ω is the weight associated to the regularization term. In particular, R is defined as:

$$R = \sum_i \left[\left(\frac{\partial P_i}{\partial x} \right)^2 + \left(\frac{\partial P_i}{\partial y} \right)^2 \right] \quad (5.12)$$

During network validation, the catheter tip position is given by the position of the peak in the output map:

$$(x_t^p, y_t^p) = \arg \max_{i,j} P_{i,j} \quad (5.13)$$

5.4 Sensor Fusion Algorithm

In this section, a simplified kinematics based model is used to estimate the tip position of the magnetic catheter in 2D by fusing ultrasound and FBG measurements. This is followed by the application of a Luenberger state observer and a Kalman filter. In the following, it is assumed that the dynamics of the catheter can be approximated by a linear time-invariant model. Further, the influence of deviations of the actual system from the linear system are modeled with a disturbance term. The dynamics of a continuous-time LTI (linear time-invariant) system is expressed as follows:

$$\dot{\mathbf{x}}_p = \mathbf{A}_{pc}\mathbf{x}_p + \mathbf{B}_{pc}\mathbf{u} + \mathbf{B}_{pc}\mathbf{d} \quad (5.14)$$

$$\mathbf{y} = \mathbf{C}_{pc}\mathbf{x}_p + \mathbf{D}_{pc}\mathbf{u} + \mathbf{v} \quad (5.15)$$

where $\mathbf{x}_p \in \mathbb{R}^{n_p}$ and $\mathbf{u} \in \mathbb{R}^m$ are the state of the plant and the control input, respectively. Further, $\mathbf{d} \in \mathbb{R}^{n_d}$, $\mathbf{v} \in \mathbb{R}^l$ and $\mathbf{y} \in \mathbb{R}^l$ are the disturbance, the measurement noise and the measured output, respectively. The measurement noise is assumed to be zero-mean, Gaussian and white. The measurement data from different sensors can be fused by collecting them together as follows:

$$\mathbf{y} = [\mathbf{y}_{sensor,1}^T \quad \cdots \quad \mathbf{y}_{sensor,l}^T]^T \quad (5.16)$$

where each $\mathbf{y}_{sensor,i}$ for $i \in \{1, \dots, l\}$ represents a measurement from a particular sensor. The dynamics of the disturbance term given in (5.14) is expressed as follows:

$$\dot{\boldsymbol{\eta}}_d = \mathbf{A}_{dc}\boldsymbol{\eta}_d + \mathbf{B}_{dc}\mathbf{w} \quad (5.17)$$

$$\mathbf{d} = \mathbf{C}_{dc}\boldsymbol{\eta}_d, \quad (5.18)$$

where $\boldsymbol{\eta}_d \in \mathbb{R}^{n_\eta}$ and $\mathbf{w} \in \mathbb{R}^{n_w}$ are the state of the disturbance dynamics and an external driving signal, respectively. The signal \mathbf{w} can either be deterministic but unknown or stochastic with the assumption of being zero-mean, Gaussian and white. If the signal \mathbf{w} is deterministic but unknown and bounded, then a Luenberger state observer can be designed. But, if the signal \mathbf{w} is stochastic with the assumption of being zero-mean, Gaussian and white, then a Kalman filter can be designed. The plant dynamics given by (5.14)-(5.15) and the disturbance dynamics given by (5.17)-(5.18) can be combined into the following augmented system

$$\dot{\mathbf{x}} = \mathbf{A}_c\mathbf{x} + \mathbf{B}_c\mathbf{u} + \mathbf{B}_{wc}\mathbf{w} \quad (5.19)$$

$$\mathbf{y} = \mathbf{C}_c\mathbf{x} + \mathbf{D}_c\mathbf{u} + \mathbf{v}, \quad (5.20)$$

with

$$\begin{aligned} \mathbf{A}_c &= \begin{bmatrix} \mathbf{A}_{pc} & \mathbf{B}_{pc}\mathbf{C}_{dc} \\ \mathbf{0}_{n_d \times n_p} & \mathbf{A}_{dc} \end{bmatrix}, \mathbf{B}_c = \begin{bmatrix} \mathbf{B}_{pc} \\ \mathbf{0}_{n_d \times m} \end{bmatrix}, \mathbf{B}_{wc} = \begin{bmatrix} \mathbf{0}_{n_p \times n_w} \\ \mathbf{B}_{dc} \end{bmatrix}, \\ \mathbf{C}_c &= [\mathbf{C}_{pc} \quad \mathbf{0}_{l \times n_\eta}], \quad \mathbf{D}_c = \mathbf{D}_{pc}, \quad \mathbf{x} = [\mathbf{x}_p^T \quad \boldsymbol{\eta}_d^T]^T \end{aligned} \quad (5.21)$$

and $\mathbf{0}$ a zero matrix of appropriate size. For systems with a low sampling rate, the LTI system given by (5.19)-(5.20) can be discretized exactly at the sampling instants using the exact discretization method. The system is discretized with a sampling time, $T_s \in \mathbb{R}_{>0}$ which corresponds to reciprocal of the frames per second (1/fps) of the imaging system. After discretizing (5.19) and (5.20), the resulting system of difference equations are given as follows:

$$\mathbf{x}[(k+1)T_s] = \mathbf{A}_d \mathbf{x}[kT_s] + \mathbf{B}_d \mathbf{u}[kT_s] + \mathbf{B}_{wd} \mathbf{w}[kT_s] \quad (5.22)$$

$$\mathbf{y}[kT_s] = \mathbf{C}_d \mathbf{x}[kT_s] + \mathbf{D}_d \mathbf{u}[kT_s] + \mathbf{v}[kT_s]. \quad (5.23)$$

The matrices in (5.22)-(5.23) are given by

$$\mathbf{A}_d = \exp(\mathbf{A}_c T_s), \quad \mathbf{B}_d = \int_0^{T_s} \exp(\mathbf{A}_c \tau) \mathbf{B}_c d\tau, \quad (5.24)$$

$$\mathbf{B}_{wd} = \int_0^{T_s} \exp(\mathbf{A}_c \tau) \mathbf{B}_{wc} d\tau, \quad \mathbf{C}_d = \mathbf{C}_c, \quad \mathbf{D}_d = \mathbf{D}_c \quad (5.25)$$

where $\exp(\cdot)$ is the matrix exponential. If \mathbf{A}_c is nonsingular, the integral terms in (5.24) and (5.25) are computed as follows:

$$\mathbf{B}_d = \mathbf{A}_c^{-1} (\mathbf{A}_d - \mathbf{I}) \mathbf{B}_c. \quad (5.26)$$

However, if \mathbf{A}_c is singular, \mathbf{B}_d can be computed as follows [22]:

$$\begin{bmatrix} \mathbf{A}_d & \mathbf{B}_d \\ \mathbf{0} & \mathbf{I} \end{bmatrix} = \exp \left(\begin{bmatrix} \mathbf{A}_c & \mathbf{B}_c \\ \mathbf{0} & \mathbf{0} \end{bmatrix} T_s \right). \quad (5.27)$$

For clarity of notation, the sampling time variables in (5.22)-(5.23) can be dropped to obtain

$$\mathbf{x}(k+1) = \mathbf{A}_d \mathbf{x}(k) + \mathbf{B}_d \mathbf{u}(k) + \mathbf{B}_{wd} \mathbf{w}(k), \quad (5.28)$$

$$\mathbf{y}(k) = \mathbf{C}_d \mathbf{x}(k) + \mathbf{D}_d \mathbf{u}(k) + \mathbf{v}(k) \quad (5.29)$$

for $k = 1, 2, 3, \dots$. In the following, the specific model for (5.19)-(5.20) used to estimate the tip positions of the flexible catheter in 2D is explained.

Consider the x- and y- tip position coordinates of the catheter denoted by $p_x, p_y \in \mathbb{R}$ and the corresponding velocities denoted by $v_x, v_y \in \mathbb{R}$. We consider the case when there are no control inputs, thus $\mathbf{u} = \mathbf{0}$ holds. Consequently, the system dynamics is given as follows:

$$\underbrace{\begin{bmatrix} \dot{p}_x \\ \dot{p}_y \\ \dot{v}_x \\ \dot{v}_y \end{bmatrix}}_{\dot{\mathbf{x}}_p} = \underbrace{\begin{bmatrix} 0 & 0 & 1 & 0 \\ 0 & 0 & 0 & 1 \\ 0 & 0 & 0 & 0 \\ 0 & 0 & 0 & 0 \end{bmatrix}}_{\mathbf{A}_{pc}} \underbrace{\begin{bmatrix} p_x \\ p_y \\ v_x \\ v_y \end{bmatrix}}_{\mathbf{x}_p} + \underbrace{\begin{bmatrix} 0 & 0 \\ 0 & 0 \\ 1 & 0 \\ 0 & 1 \end{bmatrix}}_{\mathbf{B}_{pc}} \underbrace{\begin{bmatrix} d_x \\ d_y \end{bmatrix}}_{\mathbf{d}} \quad (5.30)$$

$$\mathbf{y} = \begin{bmatrix} \mathbf{y}_{US} \\ \mathbf{y}_{FBG} \end{bmatrix} = \underbrace{\begin{bmatrix} 1 & 0 & 0 & 0 \\ 0 & 1 & 0 & 0 \\ 1 & 0 & 0 & 0 \\ 0 & 1 & 0 & 0 \end{bmatrix}}_{\mathbf{C}_{pc}} \underbrace{\begin{bmatrix} p_x \\ p_y \\ v_x \\ v_y \end{bmatrix}}_{\mathbf{x}_p} + \underbrace{\begin{bmatrix} v_{US,x} \\ v_{US,y} \\ v_{FBG,x} \\ v_{FBG,y} \end{bmatrix}}_{\mathbf{v}} \quad (5.31)$$

where the matrices given by (5.14)-(5.15) are used. Further, \mathbf{y}_{US} and \mathbf{y}_{FBG} denote the position measurements obtained from the ultrasound images and FBG sensors, respectively. If the tracking of the catheter in 3D coordinates is required, then the system dynamics can be extended by including the states p_z and v_z to the state vector and d_z to the disturbance vector. The system dynamics described by \mathbf{A}_{pc} in (5.30) with $\mathbf{d} = \mathbf{0}$ is commonly used in vision applications in the literature [23]. However, in order to have a more general yet simple model, a disturbance term should be included. There are different ways to model the disturbance term depending on the application. In order to keep the formulation sufficiently general a polynomial function is selected [24]. The disturbance term can be locally represented by an $(n - 1)^{\text{th}}$ degree family of Taylor polynomial function of time as follows:

$$d_j(t) = \sum_{i=0}^{n-1} d_{j,i} t^i + d_{j,r}(t) \quad (5.32)$$

where $j \in \{x, y\}$, $d_{j,i} \in \mathbb{R}$ and $d_{j,r}(t) \in \mathbb{R}$ are the coefficients of the polynomial and a residual term, respectively. It is assumed that the residual term, $d_{j,r}(t)$, is such that its time derivatives for $i \geq n$ satisfy $|d_{j,r}^{(i)}(t)| \leq \gamma_{i-r} \approx 0$, thus they are all uniformly absolutely bounded and small enough to be negligible [24]. This implies that the residual term is slowly varying with respect to time. The disturbance dynamics for a polynomial of degree n is

given by

$$\underbrace{\begin{bmatrix} \dot{\boldsymbol{\eta}}_{d,1} \\ \dot{\boldsymbol{\eta}}_{d,2} \\ \vdots \\ \dot{\boldsymbol{\eta}}_{d,n-1} \\ \dot{\boldsymbol{\eta}}_{d,n} \end{bmatrix}}_{\dot{\boldsymbol{\eta}}_d} = \underbrace{\begin{bmatrix} \mathbf{0}_2 & \mathbf{I}_2 & \dots & \mathbf{0}_2 & \mathbf{0}_2 \\ \mathbf{0}_2 & \mathbf{0}_2 & \dots & \mathbf{0}_2 & \mathbf{0}_2 \\ \vdots & \vdots & \ddots & \vdots & \vdots \\ \mathbf{0}_2 & \mathbf{0}_2 & \dots & \mathbf{0}_2 & \mathbf{I}_2 \\ \mathbf{0}_2 & \mathbf{0}_2 & \dots & \mathbf{0}_2 & \mathbf{0}_2 \end{bmatrix}}_{\mathbf{A}_{dc}} \underbrace{\begin{bmatrix} \boldsymbol{\eta}_{d,1} \\ \boldsymbol{\eta}_{d,2} \\ \vdots \\ \boldsymbol{\eta}_{d,n-1} \\ \boldsymbol{\eta}_{d,n} \end{bmatrix}}_{\boldsymbol{\eta}_d} + \underbrace{\begin{bmatrix} \mathbf{0}_2 \\ \mathbf{0}_2 \\ \vdots \\ \mathbf{0}_2 \\ \mathbf{I}_2 \end{bmatrix}}_{\mathbf{B}_{dc}} \underbrace{\begin{bmatrix} d_{x,r}^{(n)} \\ d_{y,r}^{(n)} \end{bmatrix}}_{\mathbf{w}},$$

$$\underbrace{\begin{bmatrix} d_x \\ d_y \end{bmatrix}}_{\mathbf{d}} = \underbrace{\begin{bmatrix} \mathbf{I}_2 & \mathbf{0}_2 & \dots & \mathbf{0}_2 & \mathbf{0}_2 \end{bmatrix}}_{\mathbf{C}_{dc}} \boldsymbol{\eta}_d \quad (5.33)$$

where $\mathbf{0}_2$ and \mathbf{I}_2 are zero and identity matrices, respectively. Further, in (5.33) each element of the state vector $\boldsymbol{\eta}_d$ satisfies $\boldsymbol{\eta}_{d,i} \in \mathbb{R}^2$.

Both the Luenberger observer and Kalman filter uses the model of a given system together with a suitable update term to estimate state variables that cannot be measured. In order to apply them to the augmented system dynamics (5.22)-(5.23), the system should be observable. This is satisfied if the observability matrix

$\mathcal{O}^T = \left[\mathbf{C}_d^T \quad \mathbf{A}_d^T \mathbf{C}_d^T \quad \dots \quad (\mathbf{A}_d^{n_p+n_d-1})^T \mathbf{C}_d^T \right]$ has full rank, i.e. $\text{rank}(\mathcal{O}) = n_p + n_d$. The Luenberger observer is typically a copy of the augmented system dynamics (5.22)-(5.23) with a correction term

$$\hat{\mathbf{x}}(k+1) = \mathbf{A}_d \hat{\mathbf{x}}(k) + \mathbf{B}_d \mathbf{u}(k) - \mathbf{L}(\hat{\mathbf{y}}(k) - \mathbf{y}(k)), \quad (5.34)$$

with the observer state $\hat{\mathbf{x}}(k)$ and feedback gain matrix \mathbf{L} . Using (5.28), (5.29) and (5.34) and defining the observation error as $\mathbf{e}(k) = \hat{\mathbf{x}}(k) - \mathbf{x}(k)$, the error dynamics is given as:

$$\mathbf{e}(k+1) = (\mathbf{A}_d - \mathbf{L}\mathbf{C}_d) \mathbf{e}(k) + \mathbf{L}\mathbf{v}(k) - \mathbf{B}_{wd} \mathbf{w}(k). \quad (5.35)$$

Here, the feedback gain matrix is designed such that if the system is observable, the eigenvalues of the nominal system (i.e. for $\mathbf{v} = 0$ and $\mathbf{w} = 0$) can be placed at arbitrary locations, for instance using Ackermann's formula. The nominal system (i.e. for $\mathbf{v} = 0$ and $\mathbf{w} = 0$) is asymptotically stable if all of the eigenvalues are inside the unit disk. The stability of the error dynamics (5.35) can be shown using a variation of the input-to-state stability theorem.

The Kalman filter consists of two phases at each sampling loop: prediction and update. In both phases next to the state estimate, the covariance

of the observation error is estimated. In the prediction phase the estimate of the state is obtained using the discretized system dynamics (5.28)-(5.29) as follows:

$$\widehat{\mathbf{x}}(k+1 | k) = \mathbf{A}_d \widehat{\mathbf{x}}(k | k) + \mathbf{B}_d \mathbf{u}(k) \quad (5.36)$$

where $\widehat{\mathbf{x}}(k | k)$ is the estimate of $\widehat{\mathbf{x}}$ at time instant k given observations up to and including at time k . The predicted estimate of the error covariance matrix $\mathbf{P}(k+1 | k) = \text{cov}(\mathbf{x}(k+1) - \widehat{\mathbf{x}}(k+1 | k))$ is computed as follows:

$$\mathbf{P}(k+1 | k) = \mathbf{A}_d \mathbf{P}(k | k) \mathbf{A}_d^T + \mathbf{Q} \quad (5.37)$$

where $\mathbf{Q} \in \mathbb{R}^{(n_d+n_\eta) \times (n_d+n_\eta)}$ represents the covariance matrix of the process noise. In the update phase the state estimate can be corrected with an innovation term using the measurements

$$\widehat{\mathbf{x}}(k+1 | k+1) = \widehat{\mathbf{x}}(k+1 | k) + \mathbf{K}(k+1) [\mathbf{y}(k) - \mathbf{C}_d \widehat{\mathbf{x}}(k+1 | k)], \quad (5.38)$$

where $\mathbf{K}(k+1)$ is the optimal Kalman gain. The gain is given by

$$\mathbf{K}(k+1) = \mathbf{P}(k+1 | k) \mathbf{C}_d^T [\mathbf{C}_d \mathbf{P}(k+1 | k) \mathbf{C}_d^T + \mathbf{R}]^{-1}, \quad (5.39)$$

and $\mathbf{R} \in \mathbb{R}^{l \times l}$ is the covariance matrix of the measurement noise. On this foundation, the estimate of the error covariance matrix can be finally updated

$$\mathbf{P}(k+1 | k+1) = [\mathbf{I}_{(n_d+n_\eta)} - \mathbf{K}(k+1) \mathbf{C}_d] \mathbf{P}(k+1 | k) \quad (5.40)$$

where $\mathbf{I}_{(n_d+n_\eta)}$ is the identity matrix. The Luenberger and the Kalman state estimators are used to fuse US and FBG measurements in the next section.

5.5 Experiments

In this section, the experimental setup is briefly presented. This is followed by the experimental results comparing the tracking and fusion algorithms introduced in Sections 5.3 and 5.4.

5.5.1 Experimental Setup

The setup consists of two pairs of Helmholtz coils (Teltron Helmholtz Coils S, 3B scientific, Hamburg, Germany) that can generate a homogeneous magnetic field along the x- and y-axis of the system (see Fig. 5.1). The details of the physical properties of the coils can be found in [4]. The catheter is 55 mm long and is made of a flexible hollow PVC tube with an outer diameter of 2 mm and an inner diameter of 1.2 mm. It is steered by the Helmholtz coils using a stack of 4 cylindrical Neodymium N48 (Supermagnete, Gottmadingen, Germany) magnets (2 mm diameter, 1 mm height) attached to the distal end of its shaft. The tip position of the catheter in 2D is obtained using transverse US images and FBG strain measurements. The transverse B-mode US images are acquired using a 14 MHz US transducer (L14-5/38, Ultrasonix, Richmond, Canada) in which the radial cross-section of the distal end of the shaft is visualized as a circular or oval shape. The strain measurements are obtained using a multicore FBG fiber (FBGS International NV) which has 4 cores where each core has 32 FBG sensors. The FBG sensor data is acquired using an FBG-Scan 804D interrogator. The accuracy of the visual tracking for the US tracker is measured using stereo cameras (Sony XCD-SX90, lenses Pentax 8.5mm, focus 0.2 - infinity, Cosmicar/Pentax 12 mm, focus 0.2 - infinity). The software to acquire the FBG data, US and stereo camera images is written in C++ on Linux Ubuntu. The sampling frequency of the measurements is set to 14 Hz.

5.5.2 Experimental Results

In this section, the results related to the template based tracking algorithm described in Section 5.3.1 are given. This is followed by the results for the fusion of US and FBG data.

Visual Tracking Results

The magnetic catheter is steered in a water tank using a pair of Helmholtz coils and its tip is imaged using a 2D ultrasound probe transversely. The US images are acquired with a rate of 14 fps.

The results of template tracking are shown in Fig. 5.5. It can be observed from Fig. 5.5 that the catheter pixel intensity changes over time. Also, a small number of pixels are available in the US image plane. Under these circumstances, the catheter tip is successfully tracked in long term using the scale-offset and affine motion models.

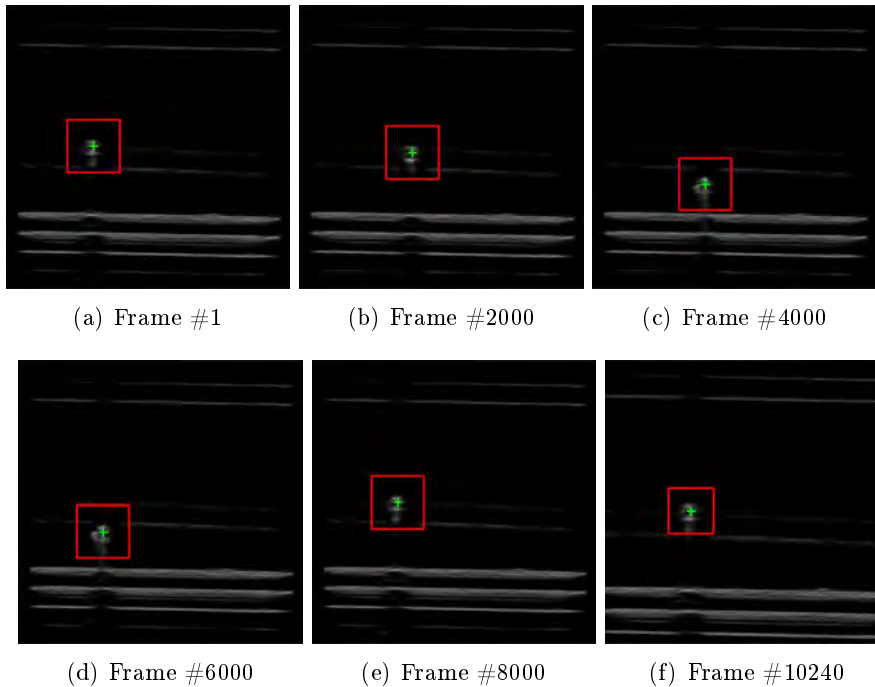


Figure 5.5: Template based tracking results of a flexible catheter in 2D transverse ultrasound images.

For the training of the proposed CNN tracking approach, two additional US sequences with different catheter motions were used and the network was trained to reproduce the results of the template tracker. The sequences were randomly separated into training, test, and validation sets. Training was performed with stochastic gradient descent with iterative learning rate reduction once there was no improvement in testing accuracy. On the validation set we observed an average error of 0.085mm. This error represents the difference between the network output and the ground truth. It is independent of the resolution of the US probe and it can even be lower. Although, practically such an error level would not be meaningful. When applying this network to the previously unseen sequence shown in Fig. 5.7, however, we observed an average error of 1.411mm. This implies, that for a more robust network more data would have to be collected, covering different motion patterns and visual appearances of the catheter.

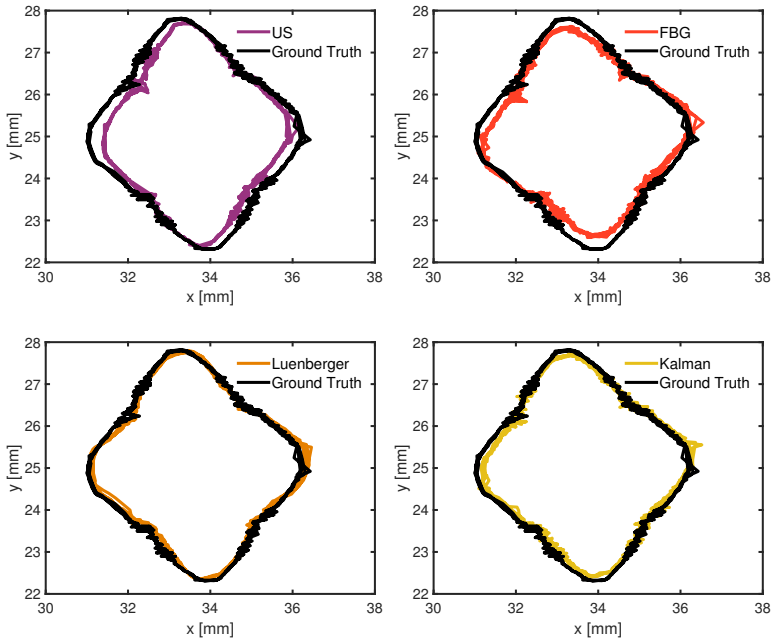


Figure 5.6: The data fusion results for the catheter tip using Luenberger and Kalman state estimators are shown. Further, the ultrasound position obtained from the template based tracker and Fiber Bragg Grating sensor are also plotted. The ground truth obtained from the stereo cameras are also given.

Sensor Fusion Results

The accuracy of the sensor fusion method is evaluated using the ground truth data obtained from the stereo camera setup. The template based tracker described in Section 5.3.1 is used to obtain the ground truth data with respect to the world coordinate system.

First of all, the stereo cameras (see Fig. 5.1) are calibrated using the method described in [25]. Then, the tip coordinates of the catheter obtained using visual tracking and FBGs are expressed with respect to the an inertial coordinate frame attached to the US. In order to obtain the ground truth position of the catheter, its tip is tracked in stereo camera images using the SSD based tracking method. Thus, the complexity of the algorithm is reduced.

The magnetic catheter is commanded to follow different geometric paths such as circle, rhombus and figure eight paths using the controller described

Table 5.1: Performance criteria for the fusion algorithms

	SSD	mean	std	min	max	NCC	SNR
Template-based							
Luenberger	1565.9	0.20	0.11	0.0013	0.88	0.9955	48.8
Kalman	1450.6	0.18	0.13	0.0027	0.95	0.9959	49.3
CNN-based							
Luenberger	3569.5	0.45	0.41	0.0005	2.24	0.9803	42.5
Kalman	3004.2	0.38	0.37	0.0043	2.44	0.9864	44.1

in [4]. The Luenberger state observer and Kalman filter described in Section 5.4 is used to fuse the data from US and FBG. The closed-loop observer poles for the Luenberger state observer are selected as $[0.9, 0.9, 0.9, 0.81, 0.81, 0.81, 0.729, 0.729, 0.729]$. Further, the process noise covariance is obtained empirically as $\mathbf{Q} = 5 \times \mathbf{I}_9$. The measurement noise covariance is $\mathbf{R} = \text{diag}[0.0099, 0.0059, 0.0370]$. The order of the disturbance model for both estimators is selected as $n_d = 1$.

The results for the rhombus path are shown as an example in Fig. 5.6 for the template based tracker and in Fig. 5.7 for the CNN tracker, respectively. Further, quantitative performance criteria including the sum of squared differences (SSD), normalized cross correlation (NCC), the maximum and minimum errors, the mean and the standard deviation of the Euclidean distance of each sample and signal-to-noise ratio (SNR) are given in Table 5.1. The error is computed between the ground truth and the fused positions. It can be observed from these results that the Kalman filter slightly performs better as compared to the Luenberger observer. This is more pronounced in the presence of larger US tracking errors, as is the case with the employed CNN tracker.

5.6 Conclusions

This study presents a sensor fusion method for magnetically-actuated flexible catheters. The algorithm makes use of two different source of measurements, images acquired from US and strains obtained from multicore FBGs. The tip positions for the tip of the catheter are obtained using two different visual tracking algorithms, the template-based and convolutional neural network based methods. The data obtained from both sources are fused using Luenberger and Kalman state estimators. The mean and standard deviation of the Euclidean error for the Luenberger observer is 0.2 ± 0.11 [mm] whereas for the Kalman filter it is 0.18 ± 0.13 [mm], respec-

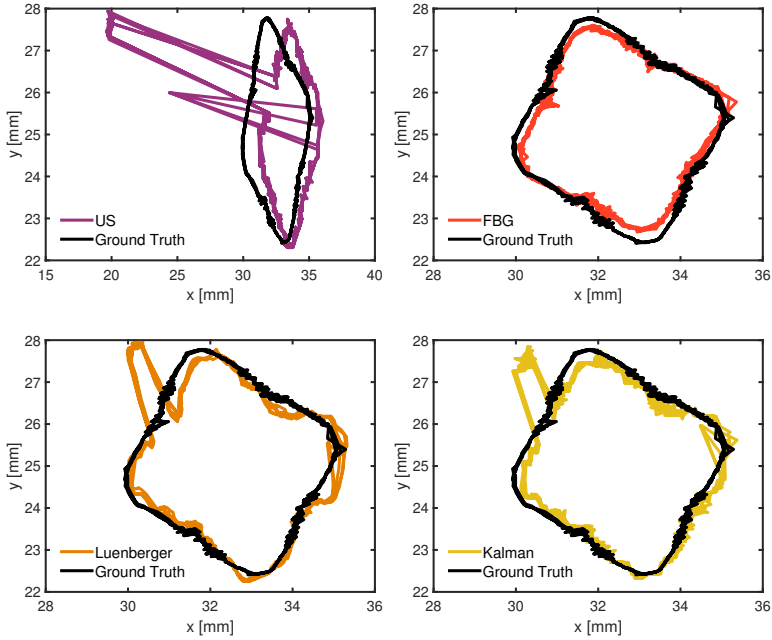


Figure 5.7: The data fusion results for the catheter tip using Luenberger and Kalman state estimators are shown. Further, the ultrasound position obtained from the convolutional neural network based tracker and Fiber Bragg Grating sensor data are also plotted. The ground truth obtained from the stereo cameras are also given.

tively. In the future work, the accuracy of the tracking and sensor fusion will be improved.

References

- [1] V. Vitiello, S. L. Lee, T. P. Cundy, and G. Z. Yang, “Emerging robotic platforms for minimally invasive surgery,” *IEEE Reviews in Biomedical Engineering*, vol. 6, pp. 111–126, 2013.
- [2] G. J. Vrooijink, A. Denasi, J. G. Grandjean, and S. Misra, “Model predictive control of a robotically actuated delivery sheath for beating heart compensation,” *The International Journal of Robotics Research*, vol. 36, no. 2, pp. 193–209, 2017.
- [3] J. Sikorski, I. Dawson, A. Denasi, E. E. G. Hekman, and S. Misra, “Introducing bigmag-a novel system for 3d magnetic actuation of flexible surgical manipulators,” in *Proceedings of IEEE/ICRA International Conference on Robotics and Automation*, pp. 3594–3599, Singapore, Singapore, May 2017.
- [4] K. J. Boskma, S. Scheggi, and S. Misra, “Closed-loop control of a magnetically-actuated catheter using two-dimensional ultrasound images,” in *Proceedings of 6th IEEE International Conference on Biomedical Robotics and Biomechanics (BioRob)*, pp. 61–66, Singapore, Singapore, June 2016.
- [5] C. Shi, X. Luo, P. Qi, T. Li, S. Song, Z. Najdovski, T. Fukuda, and H. Ren, “Shape sensing techniques for continuum robots in minimally invasive surgery: A survey,” *IEEE Transactions on Biomedical Engineering*, vol. 64, no. 8, pp. 1665–1678, Aug 2017.
- [6] V. Mishra, N. Singh, U. Tiwari, and P. Kapur, “Fiber grating sensors in medicine: Current and emerging applications,” *Sensors and Actuators A: Physical*, vol. 167, no. 2, pp. 279 – 290, 2011, solid-State Sensors, Actuators and Microsystems Workshop.
- [7] J. W. Arkwright, N. G. Blenman, I. D. Underhill, S. A. Maunder, N. J. Spencer, M. Costa, S. J. Brookes, M. M. Szczesniak, and P. G. Dinning, “A fibre optic catheter for simultaneous measurement of longitudinal and circumferential muscular activity in the gastrointestinal tract,” *Journal of Biophotonics*, vol. 4, no. 4, pp. 244–251, 2011.
- [8] L. Xu, L. A. Feuerman, J. Ge, K. R. Nilsson, and M. P. Fok, “Temperature-insensitive contact force sensing in bi-directional catheter using fiber bragg grating pair,” *IEEE Sensors Journal*, vol. 17, no. 16, pp. 5118–5122, Aug 2017.

- [9] J. P. Moore and M. D. Rogge, “Shape sensing using multi-core fiber optic cable and parametric curve solutions,” *Opt. Express*, vol. 20, no. 3, pp. 2967–2973, Jan 2012.
- [10] R. J. Roesthuis, M. Kemp, J. J. van den Dobbelsteen, and S. Misra, “Three-dimensional needle shape reconstruction using an array of fiber bragg grating sensors,” *IEEE/ASME Transactions on Mechatronics*, vol. 19, no. 4, pp. 1115–1126, Aug 2014.
- [11] J. V. Roosbroeck, C. Chojetzki, J. Vlekken, E. Voet, and M. Voet, “A new methodology for fiber optic strain gage measurements and its characterization,” in *Proceedings of the SENSOR+TEST Conferences*, vol. OPTO 2 - Optical Fiber Sensors, pp.59 - 64, Nürnberg, Germany, May 2009.
- [12] **F. Khan**, R. J. Roesthuis, and S. Misra, “Force sensing in continuum manipulators using fiber Bragg grating sensors,” in *Proceedings of IEEE International Conference on Intelligent Robots and Systems*, pp. 2531–2536, British Columbia, Canada, 2017.
- [13] M. Kaya, E. Senel, A. Ahmad, and O. Bebek, “Visual tracking of biopsy needles in 2D ultrasound images,” in *Proceedings of the IEEE International Conference on Robotics and Automation (ICRA)*, pp. 4386-4391, Stockholm, Sweden, 2016.
- [14] M. Hwangbo, J.-S. Kim, and T. Kanade, “Inertial-aided klt feature tracking for a moving camera,” in *Proceedings of IEEE/RSJ International Conference on Intelligent Robots and Systems*, pp. 1909-1916, Missouri, USA, 2009.
- [15] S. Baker and I. Matthews, “Lucas-kanade 20 years on: A unifying framework,” *International journal of computer vision*, vol. 56, no. 3, pp. 221–255, 2004.
- [16] R. Richa, R. Sznitman, and G. Hager, “Robust similarity measures for gradient-based direct visual tracking,” The Johns Hopkins University, Tech. Rep., 2012.
- [17] J.-Y. Bouguet, “Pyramidal implementation of the affine lucas kanade feature tracker description of the algorithm,” *Intel Corporation*, vol. 5, no. 1-10, p. 4, 2001.

-
- [18] I. Matthews, T. Ishikawa, and S. Baker, "The template update problem," *IEEE Transactions on Pattern Analysis & Machine Intelligence*, no. 6, pp. 810–815, 2004.
- [19] A. Newell, K. Yang, and J. Deng, *Stacked Hourglass Networks for Human Pose Estimation*. Cham: Springer International Publishing, 2016, pp. 483–499.
- [20] S. E. Wei, V. Ramakrishna, T. Kanade, and Y. Sheikh, "Convolutional pose machines," in *Proceedings of IEEE Conference on Computer Vision and Pattern Recognition (CVPR)*, pp. 4724–4732, Nevada, USA, June 2016.
- [21] F. Milletari, N. Navab, and S. A. Ahmadi, "V-net: Fully convolutional neural networks for volumetric medical image segmentation," in *Proceedings of Fourth International Conference on 3D Vision (3DV)*, pp. 565–571, California, USA, Oct 2016.
- [22] R. A. DeCarlo, "Some techniques for computing the matrix exponential and its integral," in *Linear Systems: A State Variable Approach with Numerical Implementation*. Prentice-Hall, 1989, ch. 14.
- [23] M. Azizian and R. Patel, "Data fusion for catheter tracking using kalman filtering: applications in robot-assisted catheter insertion," in *Proceedings of Medical Imaging 2011: Visualization, Image-Guided Procedures, and Modeling*, vol. 7964, pp. 327–337, Florida, USA, 2011.
- [24] H. Sira-Ramírez and V. F. Batlle, "Robust Σ - Δ modulation-based sliding mode observers for linear systems subject to time polynomial inputs," *International Journal of Systems Science*, vol. 42, no. 4, pp. 621–631, 2011.
- [25] Z. Zhang, "A flexible new technique for camera calibration," *IEEE Transactions on Pattern Analysis and Machine Intelligence*, vol. 22, no. 11, pp. 1330–1334, Nov 2000.

Chapter 6

Force Estimation

Abstract

The presence of force feedback in medical instruments has been proven to reduce tissue damage. In order to provide force feedback, information about the interaction forces between the instrument and the environment must be known. Direct measurement of these forces by commercial sensors is not feasible due to space limitation. Thus, in this study we propose to estimate the interaction forces using strain measurements from Fiber Bragg Grating (FBG) sensors. These measurements can also be used for shape sensing as a result both force and shape can be sensed simultaneously. For force sensing two models are proposed and compared: the first is based on a Rigid Link approximation, while the second uses the Cosserat rod theory. They are validated experimentally using a tendon-driven continuum manipulator that is subjected to forces at the tip. The force estimates from the models are compared to the measurements from a commercial force sensor. Mean absolute errors of 11.2 mN (6.9%) and 15.9 mN (8.3%) are observed for the Rigid Link model and Cosserat model, respectively.

6.1 Introduction

Many of the instruments currently used in medical procedures have a mechanical design similar to continuum manipulators [1]. Examples of such instruments are colonoscopes, endoscopes and other flexible catheters for procedures such as cardiac surgery and bronchoscopy. Some continuum manipulators have been developed specifically for medical applications; these include multi-backbone system for throat surgery, concentric tube active

cannula for cardiac surgery and steerable probe for neurosurgery [2–4]. These manipulators can be easily miniaturized and they provide a larger workspace compared to rigid tools, thus they are ideal for minimally invasive procedures [1]. However, the disadvantage of using such manipulators is the loss of force information at the tip. Having accurate knowledge about the interaction forces between the manipulator and tissue is important for the outcome of the procedure [5]. It can be used to provide surgeons with force feedback, thereby enabling more precise manipulation of the tissue. Sensing forces accurately at the manipulator tip is challenging because the available space does not allow integration of commercially-available force sensors. Considering further miniaturization of manipulator size in the future, there is a need for alternative methods for sensing interaction forces on manipulators for medical applications.

A number of studies have proposed methods to identify the interaction forces on manipulators without measuring them directly. For example, Xu and Simaan presented a method that used the deflected shape of the manipulator shaft to estimate the force at the tip [6,7]. Rucker and Webster estimated the tip force by using pose measurements and a kinematic static model of the continuum manipulator with measurement uncertainty [8]. They described the tip force as a state of the system, and an extended Kalman filter was used to estimate the system states from the noisy end-effector pose measurements. Lastly, Khosnam *et al.* used the curvature of a catheter, determined from camera images, in combination with a kinematic model to estimate the tip contact force [9].

Another approach to force estimation is to sense the strains on the manipulator directly using sensors. The benefit of using an independent sensor for force is that the robustness of the system to sensor failure will improve due to redundancy and in theory direct measurement of strain will lead to more accurate force estimation. A suitable sensor for medical applications is the Fiber Bragg Grating sensor because it is small in size, sterilizable, biocompatible, highly sensitive to strain, and compatible with medical imaging modalities [10]. The FBG sensors can be embedded in instruments for angioplasty, gastric endoluminal surgery or minimally invasive neurosurgery in order to measure interaction forces (Figure 6.1). These sensors have been used near the tip of medical instruments to measure only axial forces [11–13]. They have also been helically wrapped around the shaft of a manipulator in order to determine the wrench at the tip [14]. However, this approach can not be applied to all manipulators because of mechanical constraints, an example is the manipulator in Burrows *et al.* [15], thus another sensor

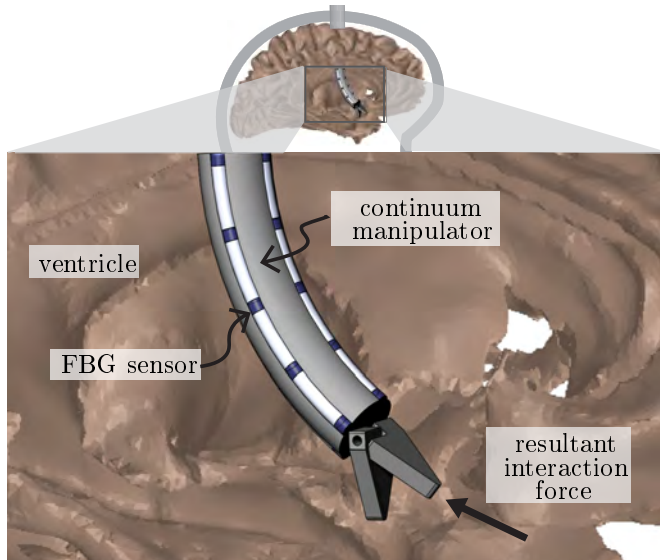


Figure 6.1: Minimally invasive neurosurgery is an example of a procedure that can benefit from instruments like continuum manipulators that provide a larger workspace compared to rigid manipulators. Fiber Bragg Grating (FBG) sensors can be used to acquire information about the interaction forces and the shape of the instrument.

placement configuration is required.

This paper presents two models that estimate contact forces on continuum manipulators using strain measurements from FBG sensors placed along the arc length. This placement configuration can also be used for shape sensing thus enabling simultaneous acquisition of force and shape information. The contact forces are estimated using the Rigid Link model and the Cosserat model. For the Rigid Link the manipulator is modeled as a series of rigid links connected by revolute joints and theory of serial manipulators is utilized to estimate contact forces. For the Cosserat the manipulator is modeled as a flexible rod and Cosserat theory is utilized to estimate contact forces. Both of the models give force estimates based on the shape information that can be derived from the FBG sensor measurements as described in Section 6.2. The Rigid Link model and the Cosserat model are presented in Sections 6.3 and 6.4, respectively. The Experimental Results and comparison between the two models are presented in Section 6.5, lastly Section 6.6 concludes the paper and provides direction for future work.

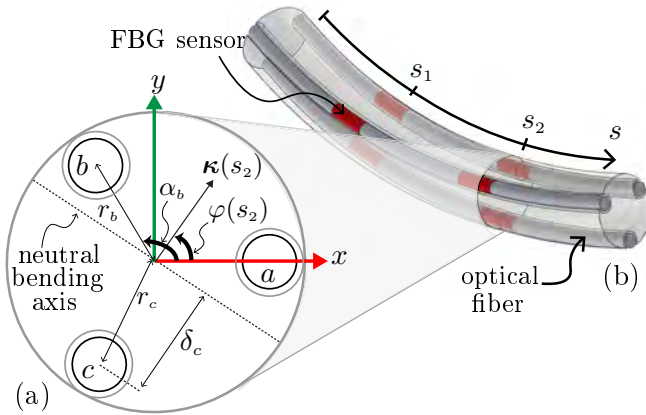


Figure 6.2: Shape reconstruction using Fiber Bragg Grating (FBG). (a) The manipulator curvature (κ) and bending direction (φ) are calculated using strain measurements from a set of three co-located FBG sensors on fibers a , b , and c . Distance from the center of the manipulator to the center of fibers b and c is r_b and r_c , respectively. Angle from x -axis to r_b is α_b and the perpendicular distance between the neutral bending axis and center of fiber c is δ_c . (b) Arc length is parameterized by s . The curvature is calculated from the strain measured at discrete locations (s_k) that have co-located FBG sensors.

6.2 Shape Reconstruction

The FBG sensors have been used for reconstruction of needle shape during insertion into soft-tissue phantoms, and for shape reconstruction of a tendon-driven continuum manipulator in free-space [16], [17]. Strain measurements from at least 3 co-located FBG sensors are required in order to calculate the magnitude ($\|\kappa\|$) and direction (φ) of the curvature vector at a discrete location (s_k , $k \in \mathbb{Z}_+$) along the manipulator shaft (Figure 6.2). Each FBG sensor measures a strain (ϵ_*), where $*$ \in (a, b, c), that is given by

$$\begin{aligned} \epsilon_*(s_k) &= \|\kappa(s_k)\| \delta_*(s_k) + \epsilon_0, \\ &= \|\kappa(s_k)\| r_* \cos(\varphi(s_k) - \alpha_*) + \epsilon_0, \end{aligned} \quad (6.1)$$

where δ_* is the distance from the fiber center to the neutral bending axis, r_* is the distance of the fiber center to the center of the manipulator, α_* is the angle of the fiber with respect to x -axis at the manipulator cross-section, $\kappa(s_k) \in \mathbb{R}^2$ is the curvature vector and $\varphi(s_k) \in \mathbb{R}$ is the direction of bend-

ing (Figure 6.2). Each sensor is assumed to have a common offset (ϵ_0) in the measured strain, that can be caused by a change in the environmental temperature or an axial force along the manipulator shaft. The three unknowns (i.e., $\|\boldsymbol{\kappa}\|$, φ and ϵ_0) are solved from the strains measured by the three co-located FBG sensors. The curvature magnitude ($\|\boldsymbol{\kappa}(s_k)\|$) and the bending direction ($\varphi(s_k)$) can be used to define the curvature vector ($\boldsymbol{\kappa}(s_k)$) at each sensor location as follows:

$$\boldsymbol{\kappa}(s_k) = \begin{bmatrix} \kappa_x(s_k) \\ \kappa_y(s_k) \end{bmatrix} = \|\boldsymbol{\kappa}(s_k)\| \begin{bmatrix} \cos(\varphi(s_k)) \\ \sin(\varphi(s_k)) \end{bmatrix}. \quad (6.2)$$

Interpolation of the curvature components ($\kappa_x(s_k)$, $\kappa_y(s_k)$) between each of the FBG sensor locations is performed in order to evaluate the curvature vector ($\boldsymbol{\kappa}(s)$) at every location along the manipulator shaft (Figure 6.2). The bending direction ($\varphi(s)$) along the shaft, is equal to the direction of the curvature vector. The curvature and the bending direction defines the orientation, which can be used to evaluate the tangent vector ($\mathbf{t}(s)$) of the curve and $\mathbf{t}(s) = \frac{d\mathbf{r}}{ds}$, where $\mathbf{r}(s) \in \mathbb{R}^3$ is the position vector of the curve. Hence, manipulator shape can be reconstructed by numerical integration of the tangent vector. The curvature and direction of bending information will be required by both the Rigid Link and Cosserat model.

6.3 Rigid Link Model

In rigid link robots contact forces/torques at the end-effector are estimated using joint forces/torques [18] [19]. The continuum manipulator is modeled as a rigid link robot with revolute joints [20]. The interaction forces at the tip are determined based on the joint torques in the model.

6.3.1 Kinematics

The continuous shape of a manipulator is approximated by a serial chain of n rigid links, connected by n revolute joints (Figure 6.3). This method can be used to describe non-constant curvature bending, that occur in flexible instruments subjected to external loading. Link orientation is described by three consecutive rotations, thus results in the following rotation matrix of the i -th link with respect to the $i - 1$ link:

$$\mathbf{R}_i^{i-1} = \mathbf{R}_z(q_{\varphi,i})\mathbf{R}_y(q_{\theta,i})\mathbf{R}_z(-q_{\varphi,i}), \quad (6.3)$$

where $\mathbf{R}_z \in SO(3)$ and $\mathbf{R}_y \in SO(3)$ are rotation matrices about the z -axis and y -axis of the rotated frame, respectively (Figure 6.3). The two joint

angles that determine the rotations in (6.3) are related to the direction of bending ($q_{\varphi,i} \in \mathbb{R}$) and the amount of bending ($q_{\theta,i} \in \mathbb{R}$). In order to describe the manipulator elasticity using the Rigid Link model, each joint is assigned a flexural stiffness that is related to the bending stiffness. In the next sub-section, manipulator statics is used to relate manipulator shape to the manipulator tip wrenches which is the result from actuation and from external loading.

6.3.2 Statics

In order to calculate manipulator configuration, the joint angles of the Rigid Link model need to be related to the loads that act on the manipulator. In static equilibrium, the loads that act on the manipulator are balanced by the torques generated in the joints. The joint torques are not generated by motors, but are the result of manipulator bending. The joints are elastic, such that a joint torque (τ_i) at the i -th joint is given by the following relation:

$$\tau_i = K_{\theta,i} q_{\theta,i}, \quad (6.4)$$

where, $K_{\theta,i}$ is the flexural stiffness, $q_{\theta,i}$ is the amount of bending (Section 6.2), and $\tau_i \in \mathbb{R}$ is the magnitude of the bending moment at the location of the joint. The bending moment ($\mathbf{m}(s_i) \in \mathbb{R}^3$) at the i -th joint is the sum of the contribution of an actuation moment and an external force (Figure 6.3):

$$\mathbf{m}(s_i) = \mathbf{m}_{ac} + \mathbf{r}_F(s_i) \times \mathbf{F}_{ext}. \quad (6.5)$$

where, $\mathbf{m}_{ac} \in \mathbb{R}^3$ is the actuation moment, $\mathbf{F}_{ext} \in \mathbb{R}^3$ is the external force and $\mathbf{r}_F(s_i) \in \mathbb{R}^3$ is the vector from the external force contact point to joint i . For a continuum manipulator with n rigid links connected by n joints, the joint torque vector ($\boldsymbol{\tau} \in \mathbb{R}^n$) can be written as

$$\boldsymbol{\tau} = \boldsymbol{\tau}_{ac} + \boldsymbol{\tau}_{ext}, \quad (6.6)$$

where $\boldsymbol{\tau}_{ac} \in \mathbb{R}^n$ and $\boldsymbol{\tau}_{ext} \in \mathbb{R}^n$ are the joint torques due to (internal) actuation and (unknown) external forces, respectively. We assume that actuation generates a pure moment at the end of the manipulator (Figure 6.3). The joint torques due to the actuation moment ($\mathbf{m}_{ac} \in \mathbb{R}^3$) can be calculated using

$$\boldsymbol{\tau}_{ac} = \mathbf{J}_m^T \begin{bmatrix} \mathbf{0}_3 \\ \mathbf{m}_{ac} \end{bmatrix} = \mathbf{J}_m^T \mathbf{w}_{ac}, \quad (6.7)$$

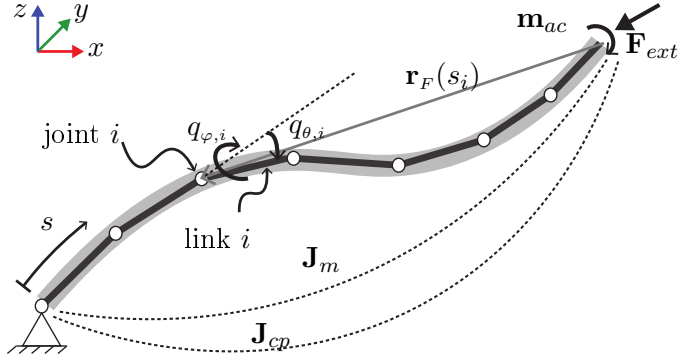


Figure 6.3: Rigid Link Model: The continuum manipulator is illustrated as bold gray curve and its shape is approximated by a serial chain of seven rigid links that are connected by revolute joints. This description enables calculation of manipulator shape under a combination of internal actuation moments (\mathbf{m}_{ac}) and external force (\mathbf{F}_{ext}). \mathbf{J}_m and \mathbf{J}_{cp} are the manipulator and contact point Jacobians, respectively. The amount of bending at joint i is given by $q_{\theta,i}$ and the direction of bending is given by $q_{\varphi,i}$. The vector from the contact point to joint i is $\mathbf{r}_F(s_i)$.

where $\mathbf{J}_m \in \mathbb{R}^{6 \times n}$ is the manipulator Jacobian, $\mathbf{0}_3 = [000]^T$, and $\mathbf{w}_{ac} \in \mathbb{R}^6$ denotes the actuation wrench. The contribution to the joint torque vector in (6.6) is given by

$$\boldsymbol{\tau}_{ext} = \mathbf{J}_{cp}^T \begin{bmatrix} \mathbf{F}_{ext} \\ \mathbf{0}_3 \end{bmatrix} = \mathbf{J}_{cp}^T \mathbf{w}_{ext}, \quad (6.8)$$

where $\mathbf{J}_{cp} \in \mathbb{R}^{6 \times n}$ is the contact point Jacobian. The above formulation will be used in combination with shape information ($q_{\varphi,i}$ and $q_{\theta,i}$) derived from FBG sensor measurements. The next section presents the rigid link model fitting based on the shape information.

6.3.3 Rigid Link Model Fitting

The model consists of n joints and n rigid links, each joint has two degrees of freedom, one related to the bending and the other related to the direction of bending. The joint angles can be determined from the curvature vector ($\boldsymbol{\kappa}(s) \in \mathbb{R}^2$) and bending direction ($\varphi(s) \in \mathbb{R}$), which are calculated from FBG sensors (Section 6.2). The joint angles that define the configuration of the Rigid Link model can be related to the curvature vector. Integrating

the curvature magnitude gives the slope ($\theta(s) \in \mathbb{R}$) along the shaft:

$$\theta(s) = \int_0^s \|\kappa(s)\| ds. \quad (6.9)$$

The joint angle related to manipulator bending can be calculated from manipulator slope as

$$q_{\theta,i} = \frac{1}{2}\Delta\theta_{i-1} + \frac{1}{2}\Delta\theta_i, \quad (6.10)$$

where $\Delta\theta_i$ is the change in manipulator slope between two consecutive joints:

$$\Delta\theta_i = \theta(s_{i+1}) - \theta(s_i). \quad (6.11)$$

The joint angle related to the bending direction equals the curvature direction at the location of the i^{th} joint ($q_{\varphi,i} = \varphi(s_i)$). Manipulator configuration is now fully defined given the curvature vector from the FBG sensor measurements. This allows the derivation of the manipulator Jacobian, which is used in the next section to estimate the unknown external forces.

6.3.4 Contact Force Estimation

The joint torque due to the unknown external load is given by $\tau_{ext} = \tau - \tau_{ac}$, where τ is determined using (6.4) and τ_{ac} is from (6.7). Thus, combining (6.4) and (6.7)

$$\tau_{ext} = \begin{bmatrix} \tau_1 \\ \vdots \\ \tau_n \end{bmatrix} = \begin{bmatrix} K_{\theta,1}q_{\theta,1} - \tau_{ac,1} \\ \vdots \\ K_{\theta,n}q_{\theta,n} - \tau_{ac,n} \end{bmatrix}. \quad (6.12)$$

The contact points are assumed to be known for all (unknown) external loads, such that the Jacobian (\mathbf{J}_{cp}) for the contact point can be determined using the forward kinematics of the Rigid Link model. In the case of a single external load (\mathbf{F}_{ext}) at the manipulator tip, the contribution to a joint torque vector from the load is given by

$$\tau_{ext} = \mathbf{J}_{cp}^T \begin{bmatrix} \mathbf{F}_{ext} \\ \mathbf{0}_3 \end{bmatrix}, \quad (6.13)$$

where, $\mathbf{J}_{cp} \in \mathbb{R}^{6 \times n}$ and $\mathbf{F}_{ext} \in \mathbb{R}^3$. For multiple external loads $\mathbf{J}_{cp} \in \mathbb{R}^{6m \times n}$, where m is the number of external loads. Since the manipulator Jacobian is often non-square, the external force is estimated using the pseudoinverse of the Jacobian

$$\begin{bmatrix} \mathbf{F}_{ext} \\ \mathbf{0}_3 \end{bmatrix} = (\mathbf{J}_{cp}^T)^\dagger \tau_{ext}, \quad (6.14)$$

where $(\cdot)^\dagger$ denotes the Moore-Penrose pseudoinverse, and $\boldsymbol{\tau}_{ext}$ is calculated from (6.12). Thus, the external force (\mathbf{F}_{ext}) is estimated using the Rigid Link model. The next section presents the Cosserat model that can also be utilized to estimate the external force.

6.4 Cosserat Model

The Cosserat rod theory presents an geometrically exact model for a flexible rod, this is the motivation for the Cosserat model. The model presented in the paper is applicable to manipulators that have small cross section area compared to their length and are not subjected to torsion or axial forces. The force at the tip of the continuum manipulator can be estimated based on the shape information calculated from the strain measurements of the FBG sensors.

6.4.1 Kinematics

The manipulator kinematics is based on a continuous transformation that is a function of the arc length [21]. In general, the transformation is dependent on the strains and shear stress acting on the manipulator, however given the assumption that the manipulator is not subjected to torsion and axial forces, the kinematics can be simplified such that the position ($\mathbf{r}(s) \in \mathbb{R}^3$) as a function of the arc length ($s \in \mathbb{R}$) can be determined by solving the following:

$$\mathbf{r}'(s) = \mathbf{R}(s)\mathbf{e}_3, \quad (6.15)$$

$$\mathbf{R}'(s) = \mathbf{R}(s)\hat{\mathbf{u}}(s), \quad (6.16)$$

where $(\cdot)'$ is the derivative with respect to s , $\mathbf{R}(s) \in SO(3)$ is the rotation matrix and it represents the change in curvature with respect to the arc length, $\mathbf{e}_3 = [0 \ 0 \ 1]^T$ and $\hat{\mathbf{u}}(s) \in so(3)$ represents a skew symmetric matrix based on the components of the curvature vector ($\mathbf{u}(s) \in \mathbb{R}^3$) that is in local coordinates. $\mathbf{u}(s) = [\kappa_x(s) \ \kappa_y(s) \ 0]^T$, the last component is zero due to the assumption of no torsion. Frenet-Serret frames are used for the local coordinates; the z_l -axis is tangent to the center curve of the manipulator, the x_l -axis is aligned with the inner normal and the y_l -axis is aligned with the binormal vector (Figure 6.4).

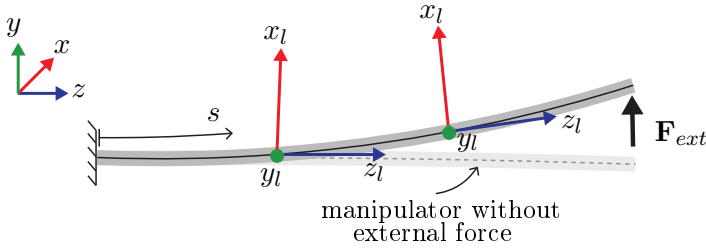


Figure 6.4: Cosserat Model: Continuous Frenet-Serret frames are assigned along the centerline curve of the manipulator. The global axis is at the base and the local axis is along the arc length of the manipulator.

6.4.2 Contact force estimation

The applied force at the tip of the manipulator is calculated using the constitutive relation and equations for equilibrium. The linear constitutive relation is as follows:

$$\mathbf{m}(s) = \mathbf{R}(s)\mathbf{K}(s)\Delta\mathbf{u}(s), \quad (6.17)$$

where $\Delta\mathbf{u}(s) = \mathbf{u}^*(s) - \mathbf{u}(s)$, $\mathbf{u}^*(s) \in \mathbb{R}^3$ is the curvature vector when no external force is applied and $\mathbf{u}(s) \in \mathbb{R}^3$ is the curvature vector after the external force is applied on the manipulator, both are in local coordinates. $\mathbf{K}(s) \in \mathbb{R}^{3 \times 3}$ is the stiffness matrix. The equations for equilibrium are as follows:

$$\mathbf{n}(s) = \int_s^L \mathbf{f}(\sigma) d\sigma, \quad (6.18)$$

$$\mathbf{m}(s) = \int_s^L [\mathbf{r}(\sigma) \times \mathbf{f}(\sigma)] d\sigma - \mathbf{r}(s) \times \mathbf{n}(s), \quad (6.19)$$

where $\mathbf{f}(\sigma) \in \mathbb{R}^3$ is the external force at the tip of the manipulator and $\sigma \in \mathbb{R}$ is a dummy integral variable. The force is modeled as a product of the unknown force $\mathbf{F}_{ext} \in \mathbb{R}^3$ and a shifted Dirac delta function, $\mathbf{f}(\sigma) = \mathbf{F}_{ext} \delta(\sigma - L)$, where L is the arc length at which the force is applied. Substituting (6.17) and (6.18) into (6.19) leads to the estimate of the external force \mathbf{F}_{ext} that is given below:

$$\mathbf{F}_{ext} = (\widehat{\Delta\mathbf{r}(s)})^\dagger \mathbf{R}(s)\mathbf{K}(s)\Delta\mathbf{u}(s), \quad (6.20)$$

where $(\cdot)^\dagger$ is the Moore-Penrose pseudoinverse and

$$\Delta\mathbf{r}(s) = \mathbf{r}(L) - \mathbf{r}(s), \quad (6.21)$$

$\widehat{\Delta\mathbf{r}}(s) \in so(3)$ is a skew symmetric matrix based on the vector $\Delta\mathbf{r}(s) \in \mathbb{R}^3$ from (6.21). The rotation matrix $\mathbf{R}(s)$ in (6.20) is calculated from (6.16). Thus, (6.20) gives the external force based on any point on the arc length and the evaluated parameters on the right hand side of the equation.

6.5 Experiments and Results

This section presents the experiments used to validate the Rigid Link and Cosserat model, the experimental setup, the calibration procedures and results.

6.5.1 Experimental Setup

The experimental setup consists of a continuum manipulator that is actuated by four tendons (DSM Dyneema B.V., Geleen, The Netherlands), shown in Figure 6.5(a). The backbone (Figure 6.5(b)) of the manipulator is made from a flexible Polyether ether ketone (PEEK) and it has grooves in which three optical fibers of diameter $250 \mu\text{m}$ are glued. Each fiber has 8 FBG sensors and the fibers are positioned such that corresponding FBG sensors are co-located (Figure 6.2). Thus, the backbone has 8 sets of co-located FBG sensors as shown in Figure 6.5(b). The setup has a linear stage to move the continuum manipulator along the global z -axis, a Deminsys Python FBG interrogator (Technobis group, Alkmaar, The Netherlands) and a Nano-43 6-DOF force/torque sensor (ATI Industrial Automation, Apex, USA). The actuation motors for the manipulator are Maxon EC-max 283840 (Maxon motor AG, Sachseln, Switzerland) and they are driven by Elmo controllers (Elmo Motion Control Ltd., Petach-Tikva, Israel). Controller Area Network (CAN) is used to provide communication with the motor drivers and Ethernet is used for communication with the interrogator and the force sensor.

6.5.2 Calibration

In order to accurately calculate curvature from the measured strains, the exact distance of the fiber from the center of the manipulator at the location of the sensor needs to be known. The shape sensing rod is placed in several constant curvature slots, which are laser cut in an acrylic plate (Figure 6.5(c)). Each fiber is separately calibrated by aligning the fiber with the bending direction of the rod. Using the curvature of the slot and the measured strain, the distance (r_a , r_b and r_c , (Figure 6.2)) between the

fiber and the center of the rod at each sensor location is calculated. The average value for all slots is calculated, and is used as the calibrated distance (Table 6.1). These values are used to calculate the curvature vectors from the strain measurements, as described in Section 6.2.

The flexural stiffness ($K_{\theta,i}$ in (6.4)) required by the Rigid Link model and the stiffness matrix ($\mathbf{K}(s)$ in (6.17)), required by the Cosserat rod model are determined experimentally due to unavailability of accurate material properties. Data from 14 experiments in conjunction with *lsqlin* (MATLAB R2015b, The MathWorks Inc., Natick, MA) is utilized to solve for the stiffness parameters. The remaining experiments were used to validate the models.

6.5.3 Experiments

The Rigid Link and the Cosserat models are validated using a tendon-driven continuum manipulator (Figure 6.5(a)). An external force (\mathbf{F}_{ext}) is applied to the tip of the manipulator from three directions (α_{ft}) which are 0° , 90° and 180° with respect to the global x -axis (Figure 6.5). The manipulator tip is tethered to the force sensor and the sensor is manually placed such that the tether is in-line with one of the three directions. Once the sensor is placed, the tension in the tether is increased, which results in an external force at the manipulator tip in the α_{ft} direction. The experiment is repeated 10 times for each direction and the measurements from the FBG sensors and the force sensor are collected. Inputs to the two models are the measurements from the FBG sensors and the output is the tip force estimate. In the next sub-section, the force sensor measurement is compared to the force estimate from both models.

Table 6.1: Mean (standard deviation in brackets) distances (in μm) of FBG sensors (r_a , r_b and r_c) after calibration

sensor #	1	2	3	4	5	6	7	8
r_a	672 (20)	743 (9)	767 (13)	802 (19)	774 (11)	748 (9)	696 (14)	412 (62)
r_b	611 (14)	695 (8)	697 (10)	704 (14)	701 (17)	681 (4)	603 (13)	289 (16)
r_c	611 (31)	672 (21)	695 (29)	722 (18)	729 (35)	683 (13)	663 (23)	413 (53)

6.5.4 Results

The magnitude of the force from the sensor and the models are compared for all experiments. The plot of the force measured and the force estimated from a representative experiment is presented in Figure 6.6. It shows that both models can track the change in applied force. The mean error (\bar{e}) and the mean relative error (\bar{re}) as defined in (6.22) and (6.23) are reported in Table 6.2. The errors are reported for all the experiments and for experiments with the same direction of applied force (α_{ft}). This approach aids in observing the behavior of the models in relation to the direction of the applied force. The results show that both models have similar performances and that force in the x - z plane are better estimated. On average, the Rigid Link model has a smaller error compared to the Cosserat model and it is computationally less complex thus a good option for real time applications.

$$e(t) = |(\|\mathbf{F}_{sen}(t)\| - \|\mathbf{F}_{mdl}(t)\|)|, \quad (6.22)$$

$$re(t) = \frac{e(t)}{\|\mathbf{F}_{sen}(t)\|} \text{ s.t } \|\mathbf{F}_{sen}(t)\| > 0, \quad (6.23)$$

where $t \in \mathbb{R}$ represents time, $\mathbf{F}_{sen}(t) \in \mathbb{R}^3$ is the force measurement from the sensor and $\mathbf{F}_{mdl}(t) \in \mathbb{R}^3$ is the force estimate from the models.

Table 6.2: Model Comparison: Mean error (\bar{e}) with standard deviation in brackets and mean relative error (\bar{re}) for experiments with applied force in α_{ft} direction and for all experiments

α_{ft}		0°	90°	180°	All
Rigid Link	\bar{e} (mN)	5.6 (6.0)	19.7 (20.8)	6.5 (7.1)	11.2 (15.3)
	\bar{re} (%)	6.9	6.1	6.9	6.9
Cosserat	\bar{e} (mN)	8.2 (9.6)	29.4 (31.9)	7.6 (7.1)	15.9 (23.1)
	\bar{re} (%)	6.2	11	7.5	8.3

6.6 Conclusions

This paper provides a framework for the FBG sensors that can be utilized for simultaneous shape and force sensing in continuum manipulators. In addition, two models for force sensing are presented and validated on a tendon driven continuum manipulator. The results show that the Rigid Link and Cosserat model can estimate the applied tip forces with an error of 11.2

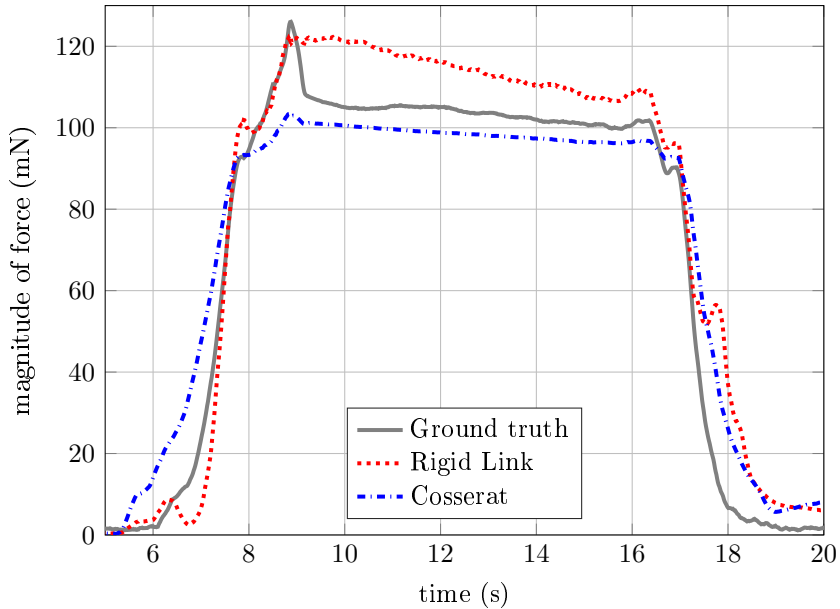


Figure 6.6: Representative plot from an experiment where the tip force (\mathbf{F}_{ext}) is applied in the $\alpha_{ft} = 180^\circ$ direction. The output from the models is compared to the force sensor measurement (ground truth).

mN (6.9%) and 15.9 mN (8.3%), respectively. For future work, the wrenches along the shaft of the manipulator and the axial force will be included in the models. The estimated forces could be used for closed loop force control coupled with other clinical imaging modalities for accurate manipulation.

References

- [1] R. J. Webster and B. A. Jones, “Design and Kinematic Modeling of Constant Curvature Continuum Robots: A Review,” *The International Journal of Robotics Research*, vol. 29, no. 13, pp. 1661–1683, 2010.
- [2] N. Simaan, K. Xu, A. Kapoor, W. Wei, P. Kazanzides, P. Flint, and R. Taylor, “Design and Integration of a Telerobotic System for Minimally Invasive Surgery of the Throat.” *The International Journal of Robotics Research*, vol. 28, no. 9, pp. 1134–1153, 2009.
- [3] A. H. Gosline, N. V. Vasilyev, E. J. Butler, C. Folk, A. Cohen, R. Chen, N. Lang, P. J. del Nido, and P. E. Dupont, “Percutaneous intracardiac

- beating-heart surgery using metal MEMS tissue approximation tools,” *The International Journal of Robotics Research*, vol. 31, no. 9, pp. 1081–1093, 2012.
- [4] S. Bano, S. Y. Ko, and F. Rodriguez, “Smooth Path Planning for a Biologically-Inspired Neurosurgical Probe,” in *Proceedings of the Annual International Conference of the IEEE Engineering in Medicine and Biology Society*, pp. 920–923, San Diego, USA, 2012.
- [5] C. R. Wagner, N. Stylopoulos, and R. D. Howe, “The role of force feedback in surgery: Analysis of blunt dissection,” in *Proceedings of the Tenth Symposium on Haptic Interfaces for Virtual Environment and Teleoperator Systems*, pp. 68–74, Orlando, USA, Mar 2002.
- [6] K. Xu and N. Simaan, “An Investigation of the Intrinsic Force Sensing Capabilities of Continuum Robots,” *IEEE Transactions on Robotics*, vol. 24, no. 3, pp. 576–587, 2008.
- [7] K. Xu and N. Simaan, “Intrinsic Wrench Estimation and its Performance Index for Multisegment Continuum Robots,” *IEEE Transactions on Robotics*, vol. 26, no. 3, pp. 555–561, 2010.
- [8] D. C. Rucker and R. J. Webster, “Deflection-based force sensing for continuum robots: A probabilistic approach,” in *Proceedings of the IEEE International Conference on Intelligent Robots and Systems*, pp. 3764–3769, San Francisco, USA, Sept 2011.
- [9] M. Khoshnam, A. C. Skanes, and R. V. Patel, “Modeling and estimation of tip contact force for steerable ablation catheters,” *IEEE Transactions on Biomedical Engineering*, vol. 62, no. 5, pp. 1404–1415, 2015.
- [10] S. C. Ryu and P. E. Dupont, “FBG-based Shape Sensing Tubes for Continuum Robots,” in *Proceedings of the IEEE International Conference on Robotics and Automation*, pp. 3531–3537, Hong Kong, China, may 2014.
- [11] B. Gonenc and I. Iordachita, “FBG-Based Transverse and Axial Force-Sensing Micro-Forceps for Retinal Microsurgery,” in *Proceedings of the IEEE Sensors*, pp. 5–7, Orlando, USA, Oct 2016.
- [12] S. Elayaperumal, J. H. Bae, D. Christensen, M. R. Cutkosky, B. L. Daniel, R. J. Black, J. M. Costa, F. Faridian, and B. Moslehi, “MR-compatible biopsy needle with enhanced tip force sensing,” in *Proceed-*

-
- ings of the World Haptics Conference*, pp. 109–114, Daejeon, Korea, April 2013.
- [13] L. Xu, M. I. Miller, J. Ge, K. R. Nilsson, Z. T. H. Tse, and M. P. Fok, “Temperature-Insensitive Fiber-Optic Contact Force Sensor for Steerable Catheters,” *IEEE Sensors*, vol. 16, no. 12, pp. 4771–4775, 2016.
- [14] R. Xu, A. Yurkewich, and R. V. Patel, “Curvature , Torsion , and Force Sensing in Continuum Robots Using Helically Wrapped FBG Sensors,” *IEEE Robotics and Automation Letters*, vol. 1, no. 2, pp. 1052–1059, 2016.
- [15] C. Burrows, R. Secoli, and F. Rodriguez, “Experimental Characterisation of a Biologically Inspired 3D Steering Needle,” in *Proceedings of the International Conference on Control, Automation and Systems*, pp. 1–6, Gwangju, Korea, Oct 2013.
- [16] R. J. Roesthuis, S. Janssen, and S. Misra, “On using an array of fiber Bragg grating sensors for closed-loop control of flexible minimally invasive surgical instruments,” in *Proceedings of the IEEE/RSJ International Conference on Intelligent Robots and Systems*, pp. 2545–2551, Tokyo, Japan, Nov 2013.
- [17] R. J. Roesthuis, M. Kemp, and J. J. V. D. Dobbelsteen, “Three-Dimensional Needle Shape Reconstruction Using an Array of Fiber Bragg Grating Sensors,” *IEEE/ASME Transactions on Mechatronics*, vol. 19, no. 4, pp. 1115–1126, 2014.
- [18] K. S. Eom, I. H. Suh, W. K. Chung, and S. R. Oh, “Disturbance Observer Based Force Control of Robot Manipulator without Force Sensor,” in *Proceedings of the IEEE International Conference on Robotics and Automation*, pp. 3012–3017, Leuven, Belgium, May 1998.
- [19] N. Likar and L. Žlajpah, “External joint torque-based estimation of contact information,” *International Journal of Advanced Robotic Systems*, vol. 11, no. 7, pp. 1–11, 2014.
- [20] T. Greigarn and M. C. Çavuşoğlu, “Pseudo-Rigid-Body Model and Kinematic Analysis of MRI-Actuated Catheters,” in *Proceedings of the IEEE International Conference on Robotics and Automation*, pp. 2236–2243, Washington, USA, May 2015.

- [21] D. C. Rucker, B. A. Jones, and R. J. Webster, “A geometrically exact model for externally loaded concentric-tube continuum robots,” *IEEE Transactions on Robotics*, vol. 26, no. 5, pp. 769–780, 2010.

Part IV

Outlook

The previous parts presented the literature relevant to the thesis along with the sensing techniques and their applications. The experimental results show that FBG sensors can be effective in localizing medical instruments. Moreover, research can be conducted further to improve the utilization of these sensors. In this part, the research presented in the thesis along with the contributions are discussed and potential future work are suggested. In addition, the scientific publications and presentations from the thesis are provided.

Chapter 7

Conclusions

7.1 Discussion and Future Work

One of the main objectives of this thesis is to develop a technique that would provide the pose, that is position and orientation, of a flexible instrument's tip. The motivation is that the tip pose of a flexible instrument is required for minimally invasive procedures, however the current methods of acquiring the tip pose have certain drawbacks. In this thesis, optical sensors called fiber Bragg grating (FBG) are utilized to acquire the pose of a flexible instrument's tip. More specifically, various techniques to derive the pose from the raw sensor data are presented along with experimental validation. The following paragraphs summarize and discuss the chapters of the thesis.

Chapter 1, presents the literature on FBG sensors in medical instruments and the main contributions of the thesis. In the research literature, FBG sensors are used in medical instruments for sensing shape and position. There are various solutions to the derivation of shape and position from the raw sensor data. This thesis contributes to the literature with techniques to acquire both position and orientation information from FBG sensors. Moreover, it also presents the techniques for distinct configurations of the FBG sensors such as the sensors in single core fiber, multi-core fiber and in helical core fiber. The next paragraph discusses Chapter 2, which focuses on the position reconstruction of a catheter.

In Chapter 2, a catheter is reconstructed in 3D space which yields the position of all the points along its length. The reconstruction is based on Frenet-Serret equations of curves, which require the catheter's shape, that is the curvature and torsion, over its length. The shape of the catheter is deduced from the shape of four multi-core fibers in the catheter. Although

for the catheter reconstruction one fiber is sufficient, utilizing four fibers makes the reconstruction less prone to individual sensor failure. Thus, leading to robust sensing which is key in clinical applications where the safety is a major prerequisite. The results show that the catheter's position can be calculated with a maximum error of 1.05 mm and mean error of 0.44 mm, which is acceptable for clinical applications like biopsies and ablations. Thus, this work shows that reconstruction with FBG sensors is feasible and applicable for medical instruments. The work is augmented in the next chapter to acquire the pose of the catheter tip.

Chapter 3 extends the reconstruction technique in Chapter 2 to acquire the orientation of the catheter tip in addition to its position, thus acquiring the catheter tip's pose. Bishop frames are used for the reconstruction instead of Frenet-Serret because they are valid for curves with discontinuity in the curvature; such as an 'S' shape curve. The reconstruction requires the catheter's shape which is calculated with the same procedure as in Chapter 2. Experimental results show that the technique in Chapter 3 has a tip position error of 4.69 mm and tip orientation error of 6.48 degrees. The difference between the position error reported in Chapter 3 and the error reported in Chapter 2 could be due to the dynamic nature of the experiments in Chapter 3. Moreover, the FBG sensors used for the experiments in Chapter 3 have lower reflectivity than the ones in Chapter 2, which could also lead to lower accuracy. Lastly, in Chapter 2 the catheter shape is based on the average of four multi-core fiber instead of one fiber, the redundancy of sensing may play a part in improving accuracy. Chapters 2 and 3 utilized multi-core fiber with straight cores that have FBG sensors, which are observed to be insensitive to twist or torsion. Thus, in the next chapter FBG sensors inscribed on helical cores are used for reconstruction.

In Chapter 4, the reconstruction technique in Chapter 3 is modified such that it is applicable to the helical core fiber. Moreover, the measurement accuracy of the helical core and straight core are compared. The position error with straight core is 0.27 mm and orientation error is 0.72 degrees, where as the position error with helical core fiber is 0.49 mm and orientation error is 0.61 degrees. The straight core fiber performs better for position measurement than the helical core fiber, whereas the helical core fiber out performs the straight core fiber in orientation measurement. Thus, for applications where twist measurement is important helical core fibers should be utilized and for applications where the curvature is crucial the straight core fiber is recommended. In clinic, position measurement is utilized more frequently than orientation measurement. However, accurate

orientation sensing would increase the accuracy of position measurement, particularly for applications where the instrument is exposed to forces from the environment that cause it to twist, such as needle insertion in tissue. Further application studies of the reconstruction techniques presented in the aforementioned chapters are given in Chapter 5 and 6.

In Chapter 5, a catheter tip is tracked by fusing tip position from ultrasound images and tip position based on FBG sensors. The catheter tip is magnetically steered and its trajectory is captured in 2D ultrasound images. The catheter tip is tracked using computer vision algorithms on the US images and the shape of the catheter is reconstructed based on FBG sensors in a multi-core fiber with straight cores. The position obtained from US and FBGs are fused using Kalman and Luenberger state estimators, with the mean error of 0.2 mm and 0.18 mm, respectively. The position error with fused measurements is lower than the position error when only one sensing technology is used. Thus, the results show that the position error can be reduced by fusing data from multiple sensors, thereby increasing the reliability of tip tracking for clinical applications and paving the way for implementation in the clinic.

In Chapter 6, FBG sensors are utilized to get an estimate of the force at a flexible instrument's tip. The curvature of the instrument is calculated from the strains on the FBG sensors and the reconstruction is acquired based on the curvature. The force at the tip is estimated from the reconstruction using two models, a Rigid link model and a Cosserat rod model, and the mean error as the percentage of the true force is found to be 6.9% and 8.3%, respectively. The study shows the feasibility of tip force estimation, which can be used for haptic feedback or to prevent tissue damage due to excessive force in clinical applications.

The FBG sensors are highly effective for medical instruments but there are a few caveats. At the time of writing, a hindrance to acquiring FBG sensors in multi-core fiber is the high cost of the sensing hardware and the fibers. Moreover, due to the lack of commercial demand for FBG sensors in multi-core fibers there are very few institutions capable and interested in producing these sensors. Though this may change in the future, until then the limited suppliers for FBG sensors in multi-core fibers will create acquisition of these sensors a challenge. Furthermore, the fibers have a very small footprint which makes them highly suitable for minimally invasive instruments. However, the auxiliary hardware such as the interrogator and the fan-out box require more space. As an example the hardware utilized in this thesis required at least 260 mm \times 230 mm \times 120 mm of space. Thus,

the placement of the hardware and the routing of the fibers require proper planning. In addition, the tethered nature of the fibers excludes them from been applicable to technologies like capsule endoscope. Nevertheless, for minimally invasive medical instruments FBG sensors are highly suitable due to their small footprint and compatibility with the clinical environment.

For future work, force sensing at the tip can be used for diagnostics via palpation, moreover possibility of diagnostic imaging like optical coherence tomography in conjunction with FBGs can be explored. An interesting study would be to compare reconstruction using single core fibers with reconstruction using multi-core fibers. Moreover, helical multi-core fibers can be combined with single core fibers in an instrument; this will result in accurate twist sensing and also accurate curvature sensing. Another area for research could be the calibration of the FBG sensors in order to further improve the pose measurement accuracy. More specifically, the complex relation between the applied strain and sensor output can be further studied and incorporated into the calibration procedure. Lastly, the pose measurement based on the FBG sensors can be validated using a commercial 6-DOF sensor, strengthening the validation provided in Chapters 3 and 4. These works would further the fundamental research in this thesis that has empirically shown the utilization of optical fibers with FBG sensors for pose measurements of medical instruments.

7.2 Scientific Disseminations

International Journal Papers

1. **F. Khan**, D. Barrera, S. Sales, and S. Misra, “Curvature, Twist and Pose Measurements using Fiber Bragg Gratings in Multi-Core Fiber: A Comparative Study between Straight and Helical Core Fiber”, *Sensors and Actuators A: Physical*, vol. 317, pp. 112442-112449, 2021.
2. **F. Khan**, A. Donder, S. Galvan, F. Rodriguez y Baena and S. Misra “Pose Measurement of Flexible Medical Instruments using Fiber Bragg Gratings in Multi-Core Fiber”, *IEEE Sensors Journal*, vol. 20, no. 18, pp. 10955-10962, 2020.
3. **F. Khan**, A. Denasi, D. Barrera, J. Madrigal, S. Sales, and S. Misra, “Multi-core optical fibers with Bragg gratings as shape sensor for flexible medical instruments”, *IEEE Sensors Journal*, vol. 19, no. 14, pp. 5878-5884, 2019.

Peer-Reviewed Conference Papers

1. A. Denasi, **F. Khan**, K. J. Boskma, M. Kaya, C. Hennersperger, R. Göbl, M. Tirindelli, N. Navab, and S. Misra, “An observer-based fusion method using multicore optical shape sensors and ultrasound images for magnetically-actuated catheters”, in *Proceedings of the IEEE International Conference on Robotics and Automation*, pp. 50-57, Queensland, Australia, 2018.
2. **F. Khan**, R. J. Roesthuis, and S. Misra, “Force sensing in continuum manipulators using Fiber Bragg Grating sensors”, in *Proceedings of the IEEE International Conference on Intelligent Robots and Systems*, British Columbia, Canada, pp. 2531-2536, 2017.

Abstracts/Posters

1. **F. Khan** and S. Misra, “Robust shape sensing for flexible medical instruments”, in *Proceedings of the W. J. Kolff Annual Research Days*, Schiermonnikoog, Netherlands, 2019.
2. **F. Khan**, A. Denasi, and S. Misra, “Shape sensing for flexible medical instruments using Fiber Bragg Grating sensors in multicore optical fibers”, in *Proceedings of the IEEE International Conference on*

Intelligent Robots and Systems — Late Breaking Result Abstract, pp. 3166, British Columbia, Canada, 2017.

Oral Presentations

1. **F. Khan** and S. Misra, “Multicore optical fibers as shape sensors for flexible medical instruments”, in *Proceedings of the W. J. Kolff Annual Research Days*, Schiermonnikoog, Netherlands, 2018.
2. A. Denasi, **F. Khan**, K. J. Boskma, M. Kaya, C. Hennersperger, R. Gobl, M. Tirindelli, N. Nawab, and S. Misra, “An observer-based fusion method using multicore optical shape sensors and ultrasound images for magnetically-actuated catheters”, in *Proceedings of the W. J. Kolff Annual Research Days*, Schiermonnikoog, Netherlands, 2018.
3. **F. Khan**, R. J. Roesthuis, and S. Misra, “Force sensing in minimally invasive medical devices”, in *Proceedings of the 6th Dutch Biomedical Engineering Conference*, Egmond aan Zee, The Netherlands, 2017.

Acknowledgments

There are many people to whom I am sincerely grateful. Thank you, Prof. Misra for giving me the opportunity to work on the EDEN2020 project, which to say the least was a very interesting and a challenging project. Thank you, Prof. Jutte for co-supervising my thesis. Thank you to Prof. Rodriguez y Baena, Stefano, Abdulhamit, Marlene, Eloise, Riccardo, Alberto, Tom, Marco and the EDEN team; it was a pleasure working with you all.

Sincere thanks to Wya, Ina, and Lianne for helping me through all the administrative tasks. A heartfelt thank you to Jeanine for been there on all matters and to Stella for getting me through the last stretch of the program. Thank you to my colleagues Guus, Navid, Roy, Federico, Jakub, Guilherme, Christoff, Alper, Gert, Theodosia, Venkat, Foad, Sumit, Klaas, Luigi, Francis, Frans and Mert for their help during my time at the Surgical Robotics Lab. Thank you to David and Prof. Sales for collaborating on the research and manufacturing the sensors which were crucial for the research.

I would also like to acknowledge the professors from University of Toronto who have had a significant impact on my education. Thank you, Prof. Nachman for making calculus accessible, Prof. Liang for teaching me probability, Prof. Abdelrahman for making programming fun and lastly, Prof. Francis for showing me the world of details. I would also like to thank my cousin Joya apu for introducing me to critical thinking.

On a more personal level, I am indebted to the Bangladeshi community in Enschede and Hengelo for making me feel at home away from home. Thank you for all the sweet memories. Special thank you to the Breimer family for easing my transition to the Netherlands, particularly Gerben for always being there for me. Moreover, thank you Hetty, Tibbe and Gerben for helping me with the samenvatting. I have been very fortunate in my life, but I am most thankful for been the daughter of my parents, Ali and Nasreen. To top off the good fortune I have two supportive brothers Emran and Nabeel, a lovely sister-in-law Shilpa, two dear nephews Aaban, Arham and a dear niece Ayra. I am very grateful to my family for their love and support.

Curriculum Vitae

Fouzia Khan was born in Munshiganj, Bangladesh and spent her childhood in Riyadh, Saudi Arabia. She was in Toronto, Canada during her teens and young adulthood. She graduated from the University of Toronto with a Master of Engineering degree in Control Systems, which is part of the Electrical and Computer Engineering department. After her studies she worked in Toronto, first as a Research Technologist at the Hospital for Sick Children and then as a Control Systems Engineer at Bionik Labs. Subsequently, she worked as a Simulation Engineer with the Formula One team Red Bull Racing in Milton Keynes, England.



In 2016, she began her Doctoral studies at University Medical Center Groningen while simultaneously been a visiting researcher at University of Twente. Currently, she works as a Mechatronics System Engineer at Demcon, Enschede, The Netherlands.

The Hitchhiker's guide to the galaxy has this to report on the best drink in existence: "The effect of a Pan Galactic Gargle Blaster is like having your brains smashed out by a slice of lemon wrapped round a large gold brick." What it does not report is that the same effect can be experienced multiple times during a PhD program.